Validation of a Lower-limb Musculoskeletal Model for the Estimation of Hip Joint Contact Forces using an Energy-based Cost Function

Margarida Oliveira Brotas de Carvalho

Thesis to obtain the Master of Science Degree in

Mechanical Engineering

Supervisors: Prof. Carlos Miguel Fernandes Quental

Prof. Jorge Alberto Cadete Ambrósio

Examination Committee

Chairperson: Prof. João Orlando Marques Gameiro Folgado

Supervisor: Prof. Carlos Miguel Fernandes Quental

Member of the Committee: Profª. Vera Moniz Pereira da Silva

December 2019

Abstract

The present dissertation aims to determine the musculoskeletal loading conditions during gait motion for two studied patients and compare these findings with in vivo data and literature. In a context of multibody dynamics, a three-dimensional biomechanical model for the lower limb based on a comprehensive dataset is presented. The biomechanical model consists in a lower limb representation for human motion analysis with small influence of the upper limbs. The anatomical articulations are approximated by ideal mechanical joints and the muscles are included in the system as two-point actuators.

A gait analysis is conducted using the kinematic and kinetic data for two patients using instrumented hip prosthesis that measure in vivo forces. The muscle and joint contact forces are calculated using inverse dynamic optimization. A static optimization technique is used to find the solution for the redundant muscle force sharing problem. The optimization consists on the minimization of a cost function that represents a physiological criterion.

The relative contribution of the energy-related terms included in the energy-based criterion is evaluated by using the in vivo measurements of hip contact forces. The contribution of each term is discussed so that the optimization can lead to a closer match between the obtained forces and the experimental measurements. The muscle forces and activations patterns are also evaluated and compared with literature. This comparison attempts to evaluate the accuracy of the biomechanical model and to identify what alterations can be made to obtain more accurate predictions of hip contact forces.

Keywords: Musculoskeletal Model, Hip Contact Forces, Inverse Dynamics, Metabolic Energy Rate, Optimization Criteria, Gait Analysis.

Resumo

A presente dissertação determina as condições de carga musculosquelética, durante a marcha, para dois pacientes e compara esses resultados com dados medidos *in vivo* e com a literatura. No contexto de dinâmica multicorpo, é apresentado um modelo biomecânico tridimensional para o membro inferior com base num conjunto de dados. O modelo biomecânico consiste numa representação do membro inferior para a análise do movimento do corpo humano, com pequena influência dos membros superiores. As articulações anatómicas são aproximadas a juntas mecânicas e os músculos são incluídos no sistema como atuadores.

Uma análise de marcha é realizada utilizando dados cinemáticos e cinéticos de dois pacientes implantados com próteses de anca instrumentadas, que medem forças *in vivo*. As forças musculares e de contato nas juntas são calculadas utilizando otimização de dinâmica inversa. O problema indeterminado da redundância muscular é resolvido utilizando otimização estática. A otimização consiste na minimização de uma função objetivo que representa um critério fisiológico.

A contribuição relativa dos termos presentes na função objetivo utilizada, baseada no consumo energético muscular, é avaliada com base nas forças de contato medidas *in vivo*. A contribuição de cada termo é discutida de forma a que a otimização permita o cálculo de forças de contato o mais próximo do *in vivo* possível. As forças e ativações musculares são também avaliadas e comparadas com a literatura. A comparação tem como objetivo avaliar o desempenho do modelo biomecânico e identificar quais são as alterações a realizar para obter previsões mais corretas das forças de contato na anca.

Palavras-Chave: Modelo Musculosquelético, Forças de Contacto na Anca, Dinâmica Inversa, Taxa de Energia Metabólica, Critério de Otimização, Análise de Marcha

Acknowledgments

Aos meus orientadores quero agradecer todo o apoio e orientação ao longo do desenvolvimento deste trabalho. Agradeço ao Professor Carlos Quental todo o empenho, paciência e disponibilidade para esclarecer todas as minhas dúvidas e ao Professor Jorge Ambrósio por toda a motivação e ajuda. Obrigada por todas as aulas e reuniões de grupo, sempre motivadoras, que enriqueceram o meu conhecimento e despertaram ainda mais o meu interesse pela área.

Aos colegas que me acompanharam durante todo o curso quero agradecer todo o apoio. Queria agradecer principalmente à Carolina e Francisca que tornaram todo o percurso académico mais leve e animado. Ficará para sempre uma enorme amizade.

Agradeço a toda a minha família por todo o carinho e apoio. Aos meus primos Catarina, Pedro, Teresa, Frederico, Marta, António, Francisco e Matias que sempre me apoiaram, inspiraram e motivaram, um grande obrigado. Agradeço também à minha avó por desde cedo ter despertado o minha curiosidade e interesse cientifico, com as suas explicações de Química incansáveis. Um grande agradecimento à minha mãe, irmã e pai por todo o carinho e paciência. Á minha mãe por toda a preocupação e afeto. À minha irmã pela grande amizade e motivação. Um especial agradecimento ao meu pai por toda a dedicação e ajuda ao longo de todo o percurso académico, especialmente nesta última fase.

Por último, um agradecimento muito especial ao Francisco por todo o carinho, apoio, paciência e inspiração.

Table of Contents

List of Figures

List of Tables

List of Acronyms

CE	Contractile Elements
COP	Center of Pressure
DOF	Degrees-of-freedom
FD	*Fréchet* Distance
GRF	Ground Reaction Forces
HCF	Hip Contact Forces
HJC	Hip Joint Centre
ISB	International Society of Biomechanics
LBL	Lisbon Biomechanics Laboratory
LLEM	Lisbon Lower Extremity Model
PE	Passive Element
RDP	Relative Deviation between Force Peaks
RMSE	Root Mean Square Error

List of Symbols

Convention

a, α, A	Scalar
a	Vector
A	Matrix
$\dot{a}$	First time derivative
$\ddot{a}$	Second time derivative
$\mathbf{A}^T$, $\mathbf{a}^T$	Matrix/Vector transpose
a'	Vector expressed in the body-fixed reference frame

Latin Symbols

$\mathbf{A}_i$	Rotation matrix of body *i*
a	Muscle activations
$\mathbf{g}^c$	Vector of internal constraint forces
q	Vector of coordinates
$\dot{\mathbf{q}}$	Vector of velocities
$\ddot{\mathbf{q}}$	Vector of accelerations
t	Time
x,y,z	Global coordinates

Greek Symbols

α	Pennation angle
Φ	Vector of kinematic constraints
$\mathbf{\Phi_q}$	Jacobian matrix of the constraints
λ	Vector of Lagrange multipliers
ε, η, ζ	Body local coordinates
ω_1, ω_2	Cost function weight factors

1. Introduction

1.1. Motivation

The human locomotion system is able to perform a wide variety of movements and, for every motion, the central nervous system selects a combination of muscles to activate in order to rotate the bones around the articulations (Carbone, 2016) to achieve the desired action. Biomechanics is defined as the science that describes, analyses and assesses the physiology of living structures and animals using the laws of mechanics. The human motion is one of the objects of study in biomechanics (Winter, 2009).

Important biomechanics research tools that helps to understand how the human body works include biomechanical models, consisting on a mathematical reproduction of the musculoskeletal biological systems in which the bones, articulations and muscles are included in the form of mechanical elements (Horsman, 2007). In this field, lower limb musculoskeletal models have enabled a wide variety of medical applications such as clinical post-operative follow-up for patients with prosthesis (Wren et al., 2011), clinical gait diagnosis, and treatment of patients with orthopaedic or neurological disabilities. These models also help to assess the consequences of medical intervention (Delp et al., 1990) and contribute to non-medical applications such as improvement of athletic performance (Pfister et al., 2014) and equipment design. A variety of human biomechanical models have been proposed, among which recently Horsman (2007) presented a complete dataset collected from a single embalmed specimen containing all the necessary information for a correct modelling of the human lower limb.

Musculoskeletal models can be applied not only to investigate the theoretical principles of the motion and control of biological systems but equally to applied research. They are used to estimate joints and muscles load forces taking place under given motions, since direct measurement of this data is strongly limited by the need of instrumented prostheses, a practice usually restricted to pathological patient cases. Hereupon, the knowledge of musculoskeletal loading is still limited (Yamaguchi et al., 1995; Carbone, 2016) i.e. the actual forces occurring *in vivo*, such as articular compression forces and muscular forces, are hardly accessible, since these forces arise from a complex interaction between the central nervous and musculoskeletal systems, owing to the redundancy of the muscle apparatus (Silva and Ambrósio, 2003). Computational biomechanical models combined with proper optimization techniques allow solving the musculoskeletal force redundancy and offer tools to estimate *in vivo* forces during motion (Yamaguchi et al., 1995; Heller et al., 2001; Praagman, 2008).

The preferred approach to solve the muscle-force sharing problem is an inverse dynamic analysis, where external forces and motion trajectories are the inputs of the optimization process. Therefore, kinematic and kinetic data must be collected beforehand using three-dimensional motion capture systems and force platforms. An important requirement to perform an inverse dynamic analysis is the definition of a cost function which best represents the physiological criteria adopted by the central nervous system to generate the muscular activation patterns needed to achieve a given motion

(Rasmussen et al., 2001). Different cost functions have been proposed in the literature (Tsirakos et al., 2017). As expected, the optimal solution found must also satisfy the equations of motion applied for the biomechanical system (Silva and Ambrósio, 2003). However, the development of more refined optimization criteria that better represents the *in vivo* process is still an ongoing field on research.

The meaningfulness of the results of the computational biomechanical models is a key issue, as most of the results cannot be measured experimentally. Two standard forms of validation are used in musculoskeletal models. A common approach is to compare the activation patterns obtained from the dynamic simulation and compare the results against electromyography (EMG) measurements. However this method does not allow full quantitative comparison of the forces (Heller et al., 2001). Moreover, the non-invasive application, i.e. the surface EMG, can only be applied to superficial muscles. Alternatively, when possible, invasive instrumented prostheses allow *in vivo* joint contact forces measurements. The *OrthoLoad* project (Bergmann, 2008) provides a comprehensive dataset containing hip contact forces (HCF) measured *in vivo* for a number of daily activities, as well as kinematics and ground reacting forces. This data repository allows to evaluate the model accuracy by comparing the forces obtained computationally, when using the measured kinematics and GRF as an input, with *in vivo* measurements (Bergmann et al., 2016; Fregly et al., 2012).

The first objective of the work now presented is to validate the Lisbon Lower Limb Model (LBL), a model based on the comprehensive dataset published by Horsman (2007). The musculoskeletal model is solved in optimization environment to find the solution for the so-called "redundant muscle force sharing problem", using an inverse dynamics approach. The model HCF predictions for gait motion of two *OrthoLoad* patients are compared with the respective *in vivo* measurements. Also, the muscle activations patterns and the forces developed are evaluated and compared with those presented in literature. This comparison attempts to evaluate the accuracy of the biomechanical model and to identify upgrades that can be implemented to obtain more accurate predictions of HCF. The main objective of the present work is to evaluate the relative contribution of the muscular energy consuming processes included in muscle load sharing cost function proposed by Praagman et al. (2006). The aim is to estimate the relative contribution of the processes included in the cost function, i.e. ion pumping and cross-bridges cycling, that can lead to a closer match between hip forces predicted by the model obtained forces and the experimental measurements.

1.2. Literature Review

Scientific literature dedicated to studying animal motion dates back to 384-322 B.C., when Aristotle introduced the concept of locomotion and movement on his work ''*De Motu Animalium*''. Later, Erasistratus (304-250 B.C.) described the muscle as a contractile element. Galen of Pergamum (129-200 A.C) made one of the most important contributions when writing works ''*De Usu Partium*'' and ''*De Moto Musculorum*'' describing the human musculoskeletal system, which were the main references for related studies for over 1300 years. Galileu Galilei (1564-1642) considered by many the *father of biomechanics,* studied the animal motion from a mechanical point of view, followed by Giovanni Borelli (1608-1679) who firstly used a geometric method to characterize and analyse human movement. Isaac

Newton (1642-1727) laws revealed fundamental for the kinematics and dynamics analysis of mechanical systems. The 18th century was marked by the constant emergence of new ideas, especially in the field of mathematics. More recently, Étienne Marey (1830-1904) implemented the first biomechanical laboratory, were he developed methods and technologies for motion capture. Major technological advances took place in the 20th century, were science developments like video motion capture systems, electromyography, advance biomechanical models and mechanical descriptions of muscles were presented, such as the Nobel awarded Archibald Hill (1886-1977) work on mathematical modelling of muscles.

1.2.1. Gait Analysis

Gait is the natural mode of human locomotion. Consequently, many studies have focused on the identification of normal and abnormal gait patterns (Gage, 1993; Sutherland, 1997; Perry and Burnfield, 2010; Chambers and Sutherland, 2002). Innovative three-dimensional motion capture systems made a radical contribution in gait assessments, allowing the detailed measurement and interpretation of human kinematics. The present section presents the main principles of gait motion analysis and how they can be useful for the validation of the proposed biomechanical model and optimization procedures.

The *gait cycle* can be defined as the time period between two identical repeating events during bipedal human locomotion (Gage, 1993). Likewise, one step can be defined as the time between the heel strike of one leg and the heel strike of the contralateral leg, and one stride as the time between two consecutive heel strikes of the same foot. In more detail, the gait cycle can be divided into two phases: stance and swing. The stance phase is defined as the period where the reference foot is contacting the floor.

Human motion is controlled by muscles and their activity is governed by characteristic average activation patterns (Ivanenko et al., 2004). Clinical techniques such as electromyography have provided a more comprehensive insight into muscle behaviour during gait. The muscle activations obtained from an inverse dynamic analysis of a biomechanical model can be compared against characteristic activation patterns. In this study, the criteria used by the central nervous system to activate the set of muscles needed for a given motion is simulated by a cost function that attempts to mimic the rationales of the central nervous system. Accordingly, the generated activation numerically patterns may differ from the actual *in vivo* patterns. Improvements in computational predictions may be achieved through further advances in the description of the musculoskeletal systems, the cost functions considered and, eventually, by better constraining the problem.

1.2.2. Biomechanical Models

Several musculoskeletal models have been developed to study the biomechanics of human locomotion. Human biomechanical models can cover the whole body (eg. Silva and Ambrósio, 2003) or only a part of the human body. The present work focus on the validation of a lower limb model that is used to study human movements in which the influence of the upper limbs is neglectable, such as gait, stair climbing or cycling. The simpler 2D models proposed in the literature are used to study the general properties of gait and other activities. However, these models only allow studying gait in the sagittal plane, missing

some spatial movement characteristics. Moreover, they cannot be used to study the complete muscular activity since the complete muscular apparatus cannot be considered. To provide a better description of the complex musculoskeletal system of the human body, 3D models comprising full dimensional articular joints with multiple degrees of freedom and including musculo-tendon actuators that consider the muscular force generating properties have been proposed (e.g. Anderson and Pandy, 2001; Silva and Ambrósio, 2003). The proposed 3D models have usually been originated from anatomical studies containing anthropometric information, such as muscle parameters and joint locations (e.g. Chandler et al., 1975). However, in most of these anatomical studies the respective datasets are not comprehensive, meaning that a complete musculoskeletal modelling can only be assembled by combining distinct datasets, and finding parameters by estimation/extrapolation.

The lower limb model applied in the present work is developed using the musculoskeletal dataset published by Horsman (2007). The authors developed a complete and consistent dataset embracing data on joint kinematics, muscle parameters and geometrical data measured from a single embalmed specimen, which contains all the necessary data for state-of-the-art musculoskeletal modelling of the lower limb. The implementation of the data presented aims to improve the estimation of internal forces, for a better biomechanical investigation. However, quantitative validation of biomechanical models based on this dataset is still on-going research (Fraysse et al., 2009; Modenese and Phillips, 2012; Carbone, 2016)

Biomechanical models can be driven by two different kinematic drivers: joint actuators and muscle actuators (Silva and Ambrósio, 2003). With joint actuators, the degrees of freedom (DOF) of the model associated with the joints are driven based on experimental obtained data, which can be considered to perform a kinematic analysis to obtain the complete model kinematics. The moments of force acting on the joints are calculated via an inverse dynamic analysis. The muscle actuators must be used when the objective is to evaluate muscle forces: the muscles are included in the biomechanical system in the form of individual actuators, each simulating the muscular force with its intrinsic muscular dynamic properties (Horsman, 2007).

To simulate the muscle contraction dynamics, a number of mechanical muscle models have been proposed in the literature (Yamaguchi, 2001). Due to a lower computational complexity and a more accurate representation of the macroscopic muscle contraction properties, the Hill-type muscle model is mostly used in biomechanical studies (Zajac, 1989). The application of the model only requires a set of parameters that can be easily extracted from anthropometric datasets. The Hill-type muscle model is described by means of passive and active elements representing the contractile properties of the muscle tissue and the elasticity of the muscle fibres and tendon. Because tendon elasticity is especially critical for fast movements and large tendon actuators, many studies consider the tendon component as a rigid element for the sake of computational simplicity (Quental et al., 2018). In effect, since the gait motion under analysis, in this work, does not involve fast movements, the tendon deformation is neglected.

1.2.3. Experimental Work

The biomechanics of motion is often studied using inverse dynamics approaches. The aim is to predict all the driving/reaction forces arising in the biomechanical model that materialise in a specific dynamic response. This analysis has great value when approaching the human locomotion system since the real forces that move the system, i.e. the muscular forces, are hardly accessible by experimentation.

In order to perform an inverse dynamic analysis, the system kinematics and kinetics, in particular the externally applied forces, must be acquired in advance and processed to guarantee kinematic consistency with the biomechanical model (Silva and Ambrósio, 2002). The kinematic data can be obtained from three-dimensional motion capture systems, measuring the trajectory of reflective markers placed on the patient's skin. Afterwards these data are used for reconstruction of the human movement. The *OrthoLoad* project (Bergmann, 2008) provides a comprehensive data set containing the three-dimensional marker trajectories, captured for implanted patients, needed for the full lower limb motion reconstruction and the relative ground reaction forces. The main advantage of this dataset is the inclusion of *in vivo* joint contact forces data, measured using instrumented implants and provided for the set of movements, allowing a cycle-to-cycle comparison with numerical results.

The estimation of muscular and internal contact forces developed in musculoskeletal models requires solving an optimization problem due to the redundancy of the muscular apparatus (Yamaguchi et al., 1995), i.e. the biomechanical model has more muscle actuators than mechanical degrees of freedom, i.e. the system is underdetermined. The optimization procedure consists on the minimization of a physiological criteria, in the mathematical form of a cost function that simulates the decision criteria taken by the central nervous system to recruit muscles. Several cost functions have been proposed in the literature (Tsirakos et al., 2017), most of which are mechanical cost functions based on muscle force (Collins, 1995; Crowninshield and Brand, 1981). However, more recently, an energy-related cost function representing the two major energy-consumption processes in the muscles was proposed by Praagman (2008). This cost function, composed of three additive terms, two related with the reabsorption of calcium ions and another with cross-bridges detachment, seems to provide more physiologically realistic results. Since the optimal relative contribution of each term in the cost function is still unknown (Nikooyan, 2011), this study aims at identifying them based on physiological quantification.

1.3. Thesis Organization

In the first Chapter of the present thesis, the context of this work is introduced and a review of the current developments in musculoskeletal modelling, gait analysis and dynamic analysis of biomechanical models are presented. In Chapter 2 the biomechanical model anatomical data, specifically the geometry of the joints, muscular parameters and geometrical parameters are presented for a correct 3D musculoskeletal model construction. The principles for the implementation of the biomechanical model using a multibody formulation are presented in Chapter 3. In this chapter the formulation and the equations required for a kinematic and dynamic analysis are also presented.

Chapter 4 describes the data acquisition processes, and how the data is processed to reconstruct the movement captured from *OrthoLoad* (Bergmann, 2008) patients and how to ensure its consistency with the musculoskeletal model. The LLEM motion is evaluated and compared with that reported in the literature. The chapter concludes with the description of the kinematic data used in the dynamic analyses and in the validation of results, i.e. the *in vivo* joint contact forces data.

Chapter 5 focuses on the description of the muscular redundancy problem in the human locomotion system. An overview of inverse dynamic analysis is presented, followed by the description of the muscle actuators, in a multibody formulation, and the muscle tissue dynamic properties, which are included in the biomechanical model to mechanically represent the muscle apparatus. Afterwards, the muscle force-sharing optimization problem formulation is presented, which is followed by a detailed description of the cost function used.

The optimization problem formulated in Chapter 5 is solved in detail in Chapter 6, starting with a standard solution using the cost function proposed in the literature and followed by an identification of the optimal cost function parameters. The HCF is the dataset used to support the function parameters identification. An evaluation of the obtained muscle activations and force patterns is also obtained in the process. In the final chapter, Chapter 7, the conclusion and future developments regarding this work are addressed.

1.4. Novel Aspects of the Work

The present thesis uses background knowledge concerning the modelling of the LLEM and a computer code with the optimization procedure to solve indeterminate problem using inverse dynamic analysis. The aim of this study is to quantify the difference in muscle forces and joint contact forces estimated by the LLEM while performing an optimization procedure using the cost function proposed by Praagman (2008). In addition, the study assesses modelling aspects related to the musculoskeletal model and the cost function that impact the performance of the biomechanical model.

Considering a two-level optimization in which the contribution of the various terms of the objective function are optimized, a cost function with different weight parameters that can lead to a closer match between calculated HCF and *in vivo* measurements is presented. Also, the relative contribution of the cost function terms is discussed in the framework of a more accurate physiological behaviour of the biomechanical model.

Biomechanical muscle modelling improvements are discussed in order to have a more accurate representation of the muscle apparatus. This is demonstrated by the evaluation of the obtained muscle activation patterns and forces and their comparison with patterns presented in literature.

2. Biomechanical Model

A biomechanical model of the human lower limb consists on a mathematical reproduction of the musculoskeletal systems in which the bones, articulations and muscles are included in the form of mechanical elements. The modelling is done based on anthropometric data, definitions of the different anatomical segments, assumed rigid bodies, and their relative mobility. Horsman (2007) proposed a unique comprehensive dataset containing all information on the modelling parameters for the lower extremity measured on a single specimen, which is used in this work. In the current chapter the LLEM, based on the dataset of Horsman (2007), is described. All information required for constructing the musculoskeletal model is presented, including the anthropometric measurements kinematic structure and a description of the muscle apparatus.

2.1. Anthropometric Measurements

Horsman (2007) measurements were performed on a male specimen embalmed at the age of *77*, with weight *105* kg and height *1.74* m. The dataset measurements were performed for the right lower extremity of the male cadaver. Data for the left lower extremity was obtained by mirroring the data from the right lower extremity. The biomechanical model proposed is composed of 11 segments, including the pelvis and 5 segments for each lower limb, i.e. femur, patella, tibia, foot and hallux, assumed as rigid bodies. Figure 1 illustrates the skeletal structure of the biomechanical model resulting from using the aformentioned datased.

ID	Rigid Body
1	Pelvis
2	Right Femur
3	Right Patella
4	Right Tibia
5	Right Foot
6	Right Hallux
7	Left Femur
8	Left Patella
9	Left Tibia
10	Left Foot
11	Left Hallux
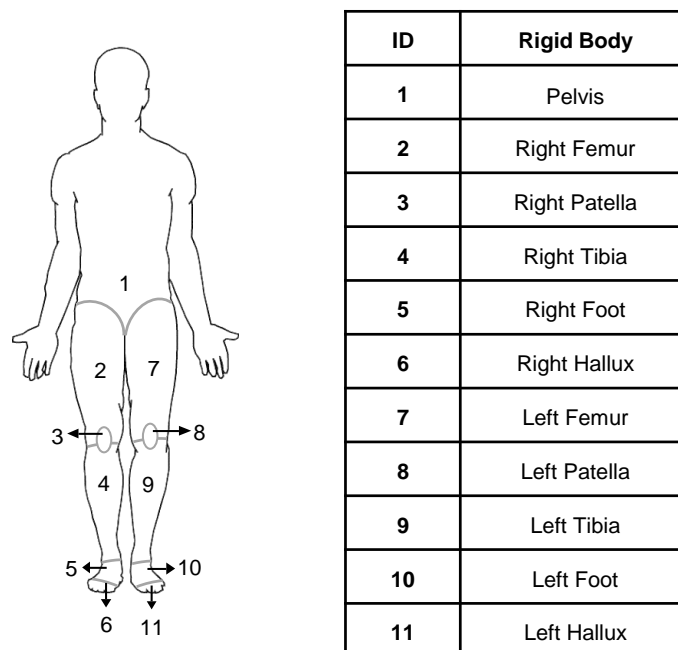
Figure 1: Biomechanical model rigid bodies description.

The parameters used for modelling the biomechanical model presented are estimated using the Horsman (2007) comprehensive dataset. Some adjustments and modifications are done in the anthropometric measurements of the model body segments, in particular mass and inertia, following the Dumas et al. (2007) recommendations. The anthropometric measurements of the biomechanical rigid bodies are presented in Table 1.

Table 1: Anthropometric measurements of the biomechanical system. The ID corresponds to the numeration adopted in Figure 1. The centre of mass of each body are for the pelvis coordinates system *(x,y,z)* for a biomechanical model position close to the anatomical reference position and moments of inertia are defined in the principal inertia axis according to (Dumas et al., 2007) .

Rigid Body	ID	Mass (kg)	Centre of Mass in global frame (m)			Principal Moments of Inertia		
			x	*y*	*x*	$I_{\xi\xi}$	$I_{\eta\eta}$	$I_{\zeta\zeta}$
HAT (pelvis)	1	15.3300	-0,0505	0,0487	-0,0905	0.1862	0.2044	0.1689
Femur	2 / 7	12.9150	0,0025	-0,1752	0,0093	0.1791	0.0479	0.1917
Patella	3 / 8	0.0862	0,0988	-0,3731	0,0353	0	0	0
Tibia	4 / 9	5.0400	0,0530	-0,5683	0,0021	0.0641	0.0082	0.0641
Foot	5 / 10	1.0434	0,1121	-0,8532	0,0275	0.0001	0.0030	0.0028
Hallux	6 / 11	0.2166	0,1747	-0,9401	0,0472	0	0	0

2.2. Description of the Kinematic Structure

The biomechanical model is composed of 11 rigid bodies connected by 10 mechanical joints and 2 inextensible ligaments. The unilateral model, i.e. one of the lower limbs, includes 5 joints, namely the hip, ankle, femur-patella, ankle and metatarsophalangeal and 1 ligament between the patella and tibia. The hip is modelled as a ball and socket joint, i.e. spherical, meaning that the connected bodies have 3 DOF. The knee, ankle and metatarsophalangeal are modelled as hinge, i.e. revolute, joints with one degree of freedom. Finally, the patella is connected to the tibia by the patellar ligament, assumed to be inextensible, and to the femur in the form of a hinge joint, representing the approximate circular path of the patella around the femur. Thus, the movement of the patella is totally restricted by the connected bodies. The same approximation is found in literature (Modenese et al., 2011).

While the knee and metatarsophalangeal articulations are hinge joints that allow only flexion and extension of the connected bodies, constraining the other DOF, the biological ankle joint is a combination of three articulations: the talocrural joint, permitting the dorsiflexion and plantarflexion, the subtalar and the tibiofibular joint, which allow the pronation and supination of the foot (Mansfield and Neumann, 2019). However, for the sake of simplicity only the talocrural joint is modelled as a revolute joint since dorsiflexion and plantarflexion define the main ankle kinematics associated with gait motion.

The biomechanical model has 18 degrees of freedom, which are the orientation and positions of the pelvis with respect to the global frame with 6 DOF, together with the rotation of the knee, ankle and metatarsophalangeal hinge joints, for 6 DOF, and the hip joint, which account for the remain 6 DOF. The exploded view of the lower limb model is illustrated in Figure 2, with the 18 DOF represented as arrows. For clarity, only the right leg joints are numbered.
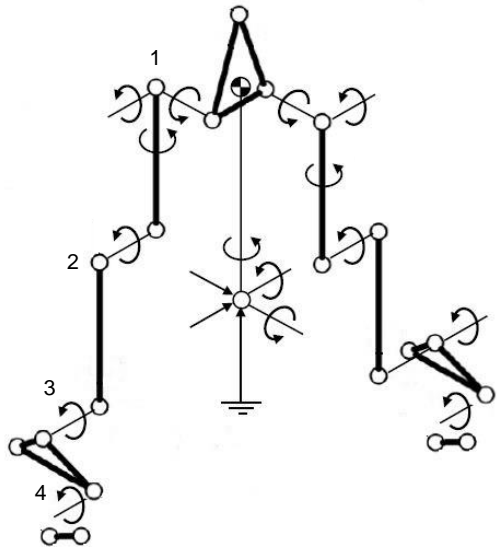
Figure 2: Exploded view of the lower limb biomechanical model. The DOF are represented as arrows for identification. The patella rotation around the femur is not represented.

The coordinates presented in Horsman (2007) dataset are expressed in the pelvis coordinate frame, considered the global frame. However, the current work uses a Cartesian coordinate formulation, to be presented in Chapter 3, to model the system. In this alternative formulation, the joint locations and other reference points are defined in relation to body-fixed coordinate frames (ξ,η,ζ). The origin of the local bodies reference frame is located at each body centre of mass and the corresponding orientations of the (ξ,η,ζ) axis are defined according to the ISB recommendations (Wu et al., 2002) using the bony landmark locations measured by Horsman (2007).

Table 2 and 3 detail the data for the anatomical joints according to the numbering presented in Figure 2, where *Body i* and *Body j* denotes the bodies connected by a joint. Table 2 describes the centre of rotation of the joint in the local reference of each body. The hip joint can be fully described by its rotation centre since no constraints exist on rotation. However, when two bodies are connected by a hinge type joint, the bodies rotate about a given axis that must be known. The direction of the rotation axis for the hinge joints is presented in Table 3. Note that this axis, representing a direction, must cross the rotation centre point presented in Table 2. The information concerning the inextensible patellar ligament is presented in Table 4.

Table 2: Centre of rotation local coordinates of the joints of the lower limb musculoskeletal model. The ID of the joints is consistent with Figure 2. The joint topology, third column, is explored in detail in Chapter 3. All coordinates are described in the respective body's local reference frame.

Joint	ID	Type	Body i	Body j	Rotation axis on Body i (m)			Rotation axis on Body i (m)		
					ξ	η	ζ	ξ	η	ζ
Hip	1	Spherical	Pelvis	Femur	0,0505	0,0505	-0,0487	0,0905	0.0167	0.1742
Knee	2	Hinge	Femur	Tibia	0,0031	0,0031	-0.2353	-0.0038	0.0142	0.1605
Ankle	3	Hinge	Tibia	Foot	0.0284	0.0284	-0.2482	-0.0142	-0.0378	0.0213
Metatarsopl.	4	Hinge	Foot	Hallux	0.0800	0.0800	-0.0329	0.0054	-0.0298	0
Patella-Fem.	5	Hinge	Femur	Patella	0.0055	0.0055	-0.2125	0.0015	-0.0652	-0.0029

Table 3: Joint's axis of rotation. The ID of the joints is consistent with Figure 2. All coordinates are described in the respective body's local reference frame.

Joint	ID	Type	Body i	Body j	Rotation axis on Body i (m)			Rotation axis on Body i (m)		
					ξ	η	ζ	ξ	η	ζ
Knee	2	Hinge	Femur	Tibia	-0.1004	-0.0589	0.9932	0.5108	-0.1097	0.8527
Pat.-Femur	3	Hinge	Femur	Patella	-0.0087	0.0613	0.9981	-0.0887	0.0613	0.9981
Ankle	4	Hinge	Tibia	Foot	0.2441	-0.1884	0.9513	-0.2949	0.0735	0.9527
Metatarsopl.	5	Hinge	Foot	Hallux	-0.2481	0	0.9687	0	0	1

Table 4: Patellar ligament an respective origin and insertion on the respective bodies.

Ligament	Type	Body i	Body j	Insertion on Body i (m)			Insertion on Body i (m)		
				ξ	η	ζ	ξ	η	ζ
Patellar lig.	Inextensible	Patella	Tibia	0.1020	-0.3970	0.0360	0.0850	-0.4550	0.0380

2.3. Muscle Apparatus Structure

A total of 38 muscles were measured by Horsman (2007). Because some muscle lines of action have a large curvature, due to underlying bones and high muscular volume, two methods are used to describe the change in muscle force directions. Bony contours which characterise mathematically the geometry of underlying structures (van der Helm et al., 1992) are used to define the muscle line of action of the *gastrocnemius* around the femur condyle and the *iliopsoas* around the pubis of the pelvis. For 19 muscles, via points are used to split the muscles in a series of shorter muscle segments (Delp et al., 1990) as an attempt to better reproduce the muscle path and the different muscle sections behaviour.

The 38 muscles are divided in 57 parts, containing up to 6 bundles, resulting in a total of 163 muscle actuators, as proposed in the Horsman (2007) dataset. The Appendix A presents the physiological and geometry properties of the 38 muscle used in the LLEM. The physiological parameters comprised are: the physiological cross-section area $PSCA$, defined as the muscle volume divided by the optimal fibre length, the optimal muscle length L_0, the tendon length L_s and the pennation angle α, defined as the angle between a fascicle's orientation and the tendon axis. The geometric parameters comprise the origin and insertion of the muscle. These parameters are needed for modelling the muscle as a mechanical element, e.g. Hill-type

3. Multibody Dynamics Review

A multibody system is defined as a collection of bodies connected to each other by joints that constrain their relative motion (Nikravesh, 1988). This formulation can be applied in biomechanical modelling, in general, and in musculoskeletal systems in particular. The rigid bodies correspond to the bones and the articulations to the joints. The biological joints are complex structures, and thus their computational implementation can be elaborated. To simplify their modelling, equivalent kinematical mechanical joints that represent the *in vivo* motion are used. In this chapter the multibody dynamics formulation used for the kinematics and dynamics of the multibody biomechanical system is presented. These methods are then applied to the three-dimensional musculoskeletal model of the lower limb to reconstruct the kinematics and evaluate the muscular and inter-segmental forces in the human lower limb. The formulation applied is based on Cartesian coordinates and the notation used by Nikravesh (1988).

3.1. Cartesian Coordinates

The position of a general point P located on body *i* in a three-dimensional fixed reference frame can be defined as:

$$\mathbf{r}_i^P = \mathbf{r}_i + \mathbf{A}_i \mathbf{s}_i'^P \tag{1}$$

where $\mathbf{r}_i$ is the global position of body *i*, $\mathbf{s}_i'^P$ is the relative position of point *P* in body *i* and $\mathbf{A}_i$ is the rotational transformation matrix from body *i* reference frame to the global reference frame.
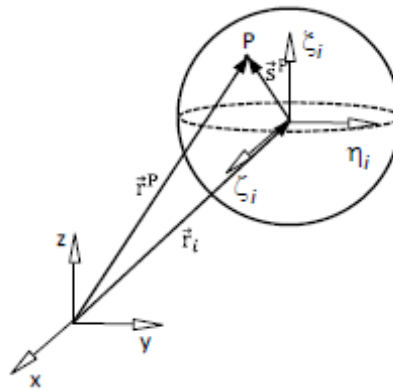
Figure 3: Rigid body position definition on a global reference frame

The position of a body in the three-dimensional space can be defined by three translational coordinates, which normally locate the body centre of mass in a fixed global reference frame, and three rotational coordinates that specify the rotation of the body reference frame in relation to the global reference. However, the use of three coordinates to specify the angular rotation of a body can originate complex mathematical formulations (Nikravesh, 1988). Euler parameters are an attractive alternative as there

are no singularities associated with these parameters and the transformation matrix is more efficiently computed. The Euler parameters define the body position resorting to four parameters (e_0, e_1, e_2, and e_3) that describe the rotation of a vector in three dimensions associated with a rotation matrix. Note that these parameters are coupled by one constraint equation, i.e. they are not independent. A body position in the three-dimensional space can be then fully defined using vector $\mathbf{q}_i$, written as:

$$\mathbf{q}_i = [x,y,z,e_0,e_1,e_2,e_3] = [\mathbf{r}_i, \mathbf{p}_i] \tag{2}$$

When describing a multibody system with n bodies, one can express its configuration using one global position vector $\mathbf{q}$:

$$\mathbf{q} = [\mathbf{q}_i, ..., \mathbf{q}_n] \tag{3}$$

In general, the coordinates contained in vector $\mathbf{q}$ are not independent being their relations described by kinematic constraints.

3.2. Kinematic Constraints

The biomechanical model of the lower limb described in Chapter 2 is composed only of a subset of joint types, namely revolute and spherical joints. Hence, for the sake of brevity, only these mechanical joints, together with driver constraints that guide the bodies through space, are formulated next. For a more detailed information about the multibody formulation of joints, including Jacobian matrices and formulations of the velocity and acceleration equations, the interested reader is directed to the reference (Nikravesh, 1988).

3.2.1. Rigid Linear Element

A rigid linear element connects point Q on body i to point P in body j by a link having a constant length L. This joint only constraints one DOF of the bodies, which is written in the form:

$$\Phi^{(rle,1)} = \mathbf{d}^T \mathbf{d} - L^2 \tag{4}$$

where

$$\mathbf{d} = \mathbf{r_j} + \mathbf{A}_j \mathbf{s}_j^{'Q} - \mathbf{r_i} - \mathbf{A}_i \mathbf{s}_i^{'P} \tag{5}$$

being $\mathbf{r}$ the global position vector of a body, $\mathbf{s}^{'Q}_i$ and $\mathbf{s}^{'P}_j$ the position of point Q and P relative to the associated body, and $\mathbf{A}$ the rotation matrix of the a body from the body coordinates frame to the global frame. Equation (4) denotes that the point Q and P must always be separated by a distance L.

3.2.2. Spherical Joint

A spherical joint connects two bodies in a way that 3 degrees of freedom are eliminated. Mathematically, this is expressed by:

$$\Phi^{(s,3)} = \mathbf{r}_i + \mathbf{A}_i \mathbf{s}_i'^P - \mathbf{r}_j - \mathbf{A}_j \mathbf{s}_j'^P = 0 \tag{6}$$

where $\mathbf{r}$ is the global position vector of a body, $\mathbf{s}'$ is the position of point P in the body fixed coordinate system. Equation (6) denotes that the point P, positioned at the joint centre, must always have a constant position in bodies i and j, local reference frames, being their local position defined by the vectors $\mathbf{s}_i'^P$ and $\mathbf{s}_i'^P$. As a result, even if the shared joint centre point P can move in space, only three relative rotational movements between the two bodies are allowed. The joint is presented in Figure 4.
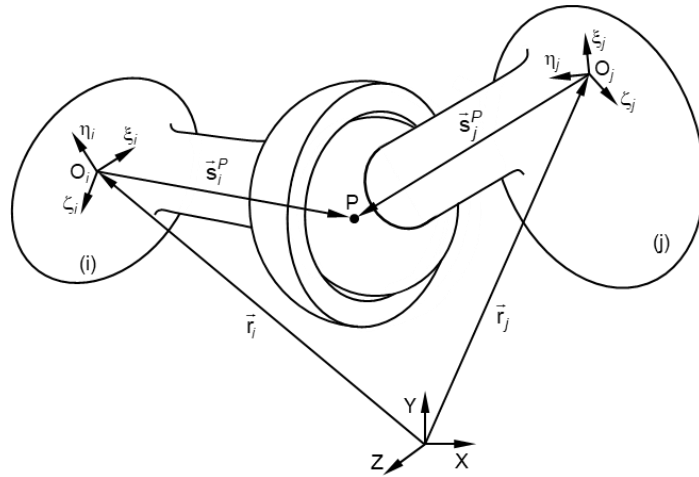
Figure 4: Spherical Joint. The two bodies share the centre of rotation P.

The hip articulation, represented in Figure 5, is a ball-and-and-socket joint, where the head of the femur is free to rotate inside the cup-shape acetabulum (Byrne et al., 2010). Therefore, a spherical joint is used to model the hip joint of the lower limb biomechanical model, since it is assumed to be a suitable approximation of the biological articulation (Arnold et al., 2010; Heller et al., 2001; Modenese et al., 2011). The point P corresponds to the joint centre of rotation presented in Table 2.
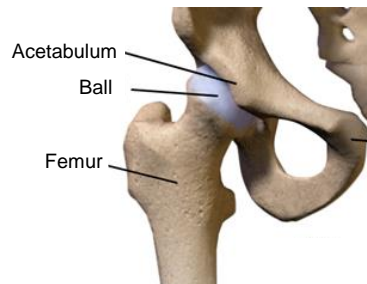
Figure 5: Hip, or *acetabulofemoral* joint. An analogy can be made to the mechanical spherical joint.

3.2.3. Revolute Joint

The revolute joint constrains the same relative motions between two bodies as the spherical joint plus two DOFs associated with relative rotations. Therefore, a revolute joint allows only two bodies to rotate around a single axis. The constraint equations of the revolute joint are:

$$\mathbf{\Phi}^{(r,5)}=\begin{bmatrix}\mathbf{\Phi}^{(s,3)}\\ \mathbf{s}_{i1}^{T}\mathbf{s}_{j}\\ \mathbf{s}_{i2}^{T}\mathbf{s}_{j}\end{bmatrix}=\mathbf{0} \tag{7}$$

The first three equations are equivalent to the spherical joint, while the two additional equations imply that the vectors $\mathbf{s}_{i1}$ and $\mathbf{s}_{j}$, and the vectors $\mathbf{s}_{i2}$ and $\mathbf{s}_{j}$, must remain perpendicular. This ensures that vectors $\mathbf{s}_{i}$ and $\mathbf{s}_{j}$ remain parallel so that the bodies can only rotate around a single axis. The revolute joint is presented in Figure 6.
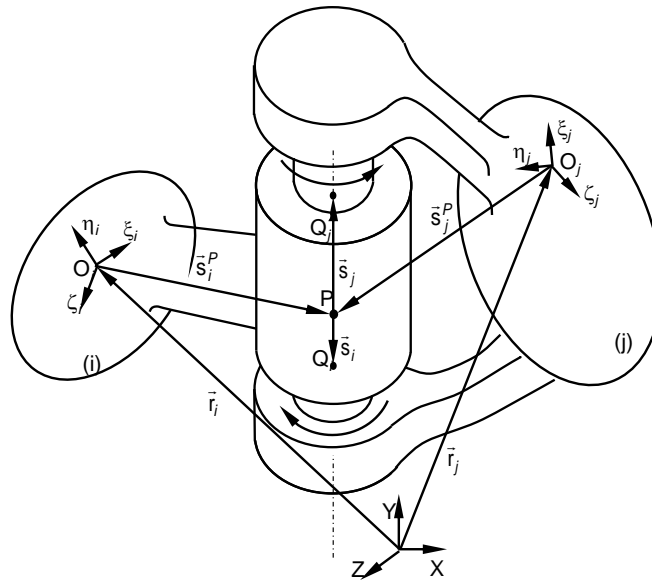
Figure 6: Revolute Joint. The two connected bodies can rotate around an axis that connects point P to Q_i (or Q_j).

This formulation is used to model the knee, ankle and metatarsophalangeal articulations. The point P is equivalent to the respective joint centre of rotation presented in Table 2 and the vectors $\mathbf{s}_j$ and $\mathbf{s}_i$ are assembled using the joint rotation axis in Table 3.

3.2.4. Prescribed Motion Constraint

To guide the position and orientation of a body along time, a driver constraint equation is applied:

$$\mathbf{\Phi}^{(pmc,7)}=\mathbf{q}_{i}-\mathbf{q}_{i}^{m}(t)=\mathbf{0} \tag{8}$$

The equation states that body position $\mathbf{q_i}$ must follow a desired trajectory $\mathbf{q_i}^m(t)$. Since the scope of this work is the study of the lower limb, this constraint is applied to guide the pelvis of the biomechanical model, according to the data obtained experimentally.

3.2.5. Rotational Driver

When the objective is to guide the relative orientation of two bodies connected by a joint, the rotational driver constraint is applied:

$$\mathbf{\Phi}^{(rd,1)} = \mathbf{u}^T\mathbf{v} - \cos(\theta(t)) \tag{9}$$

where $\mathbf{u}$ and $\mathbf{v}$ are unitary vectors fixed on body i and j local reference frames and the angle $\theta(t)$ is a function of time, obtained by evaluating the system's desired motion, acquired in the biomechanics laboratory. The process of obtaining the time dependent functions $\mathbf{q}(t)$ and $\theta(t)$ for this work is discussed in Chapter 4. In Figure 7 the rotational driver is represented as a joint actuator.
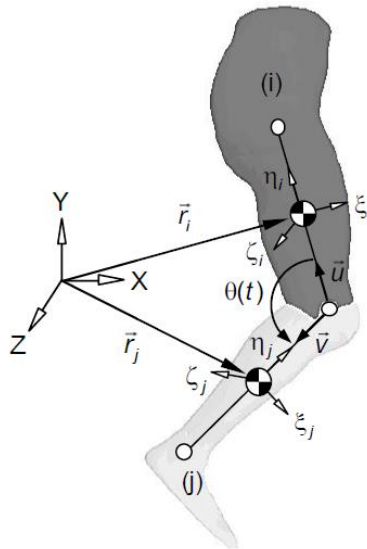
Figure 7: Rotational drive as a biomechanical joint actuator.

Note that, in the context of this work, the rotational driver substitutes the action of the muscles, acting upon the system as joint actuators. When the aim is to study the muscular forces, rotational drivers should not be considered. Instead, the muscle actuator formulation, presented in Section 5.2, must be included.

3.3. Kinematic Analysis

A kinematic analysis consists in determining the positions of the system bodies considering the restrictions of the joining components and driving constraints. This analysis must be done to ensure that the motion reconstructed is consistent with the biomechanical system model. Considering $\mathbf{\Phi}$ the vector of kinematic constraints, the following expression must hold for all time frames:

$$\Phi(q,t)=0 \tag{10}$$

The solution of Equation (10) in terms of **q** provides the kinematically consistent positions of the multibody system. Since Equation (10) is a set of non-linear equations, the solution can only be obtained numerically, using, for example, the Newton-Raphson method. This method is an iterative process based on the first order Taylor series expansion of Equation (10). The best approximation to the root of the function $\Phi(q,t)$ is reached when the residual Δq_i is lower than a given tolerance. This can be mathematically expressed as:

$$\Phi(q,t) \approx \Phi(q_i,t) + \frac{\partial \Phi(q_i,t)}{\partial q}(q\text{-}q_i) = \Phi(q_i,t) + \Phi_q \Delta q_i \tag{11}$$

where Φ_q is the Jacobian matrix of the constraints, defined as the constraint system of partial derivatives with respect to the vector of generalized coordinates **q**, and expressed as:

$$\Phi_q = \begin{bmatrix} \dfrac{\partial \Phi_1}{\partial q_1} & \cdots & \dfrac{\partial \Phi_1}{\partial q_{nb}} \\ \vdots & \ddots & \vdots \\ \dfrac{\partial \Phi_{nc}}{\partial q_1} & \cdots & \dfrac{\partial \Phi_{nc}}{\partial q_{nb}} \end{bmatrix} \tag{12}$$

where *nc* and *nb* represent the number of constraints and bodies, respectively. In each iteration:

$$q_{i+1} = q_i - \Delta q_i \tag{13}$$

The kinematic consistent velocities $\dot{q}$ and accelerations $\ddot{q}$ can be obtained by differentiating Equation (11), yielding the following expressions:

$$\dot{\Phi}(q,\dot{q},t) = \frac{\partial \Phi(q,t)}{\partial t} + \frac{\partial \Phi(q,t)}{\partial q}\dot{q} = 0 \Leftrightarrow \Phi_q \dot{q} = \nu \tag{14}$$

$$\ddot{\Phi}(q,\dot{q},\ddot{q},t) = \Phi_q \ddot{q} + (\Phi_q \dot{q})_q \text{-} \dot{\nu}(t) \Leftrightarrow \Phi_q \ddot{q} = \gamma \tag{15}$$

The *Jacobian* matrix and right hand side vectors of the velocity ν and acceleration γ equations are obtained by differentiation the constraint equations. Details can be seen in Nikravesh (1988).

3.4. Dynamic Analysis

A multibody dynamic analysis consists on the study of the system motion subjected to externally applied forces and taking into account the inertial characteristics of its components. When applied to biomechanical systems this analysis provides the joint reaction forces, joints moments-of-force and muscle forces.

3.4.1. Reaction Forces

Internal forces are generated in the system in order to fulfil the kinematic constraints. The relation between the constraint equation and the respective reaction forces can be obtained using the Lagrange multipliers method (Haug and Yen, 1992; Nikravesh, 1988).

$$\mathbf{g}^c = -\mathbf{\Phi}_q^T \boldsymbol{\lambda} \qquad (16)$$

where $\mathbf{g}^c$ denotes the vector of internal constraint forces, $\mathbf{\Phi}_q^T$ is the Jacobian matrix and $\boldsymbol{\lambda}$ is the vector of Lagrange multipliers, each associated with a reaction force developed to satisfy to the respective kinematic constraint.

3.4.2. Equations of Motion

For a general multibody system, i.e. a system of n constrained bodies, the equations of motion are written as (Nikravesh, 1988):

$$\mathbf{M\ddot{q}} = \mathbf{g} + \mathbf{g}^c \Leftrightarrow \mathbf{M\ddot{q}} + \mathbf{\Phi}_q^T \boldsymbol{\lambda} = \mathbf{g} \qquad (17)$$

where $\mathbf{g}$ is the vector of externally applied forces, such as gravitational forces and externally applied forces, obtained by assembling local forces and moments to which each body is subjected. The matrix $\mathbf{M}$ denotes the global mass matrix containing the individual body mass and moments of inertia. In an inverse dynamic analysis, the kinematics of the system, i.e., positions, velocities, and accelerations, is known in advance, e.g. obtained experimentally, as to be discussed in Chapter 5. In this case, the only unknowns of Equation (17) are the Lagrange multipliers (Silva and Ambrósio, 2003), which represent the internal forces of the biomechanical system.

4. Data Acquisition and Processing

This study focuses on evaluating the human gait since walking is the major means of locomotion for the human being. In general, gait presents common patterns among different individuals. Experimental biomechanical analysis can be used to evaluate gait from several perspectives (Bonnefoy-Mazure and Armand, 2015) playing a key role in identifying motor impairments, in postoperative clinical follow-up, and also in other fields such as improvement of athletic performance (Pfister et al., 2014).

Three-dimensional motion capture systems offer an accurate tool for supporting the study of locomotion and, as a result, for evaluating the human system kinematics. These systems allow collecting the kinematic data necessary to perform an inverse dynamic analysis. The kinematics data is complemented with kinetic data from which the externally applied forces must be computed in advance.

In this work, the data reported by the *OrhoLoad* database (Bergmann, 2008), containing experimental measurements of gait kinematics using three-dimensional motion capture systems (eg. *Vicon Motion Capture Systems*), is used. The data is processed and provided as input to the *LLEM* for motion reconstruction. Ground reaction forces are to complement the dataset required for the dynamic analysis, thus allowing a direct comparison of calculated and experimental HCF values. The reconstructed motion is further compared with literature for validation

4.1. Kinematic Data

The *Charité in Berlin* (Bergmann, 2008) measured the loads developed in human joints directly by using instrumented implants in several anatomical joints of different individuals, with hip or knee implants on those related to gait. These measurements were done for a number of daily activities, including gait. *OrhoLoad* (Bergmann, 2008) supplies not only the *in vivo* loads but also the kinematic data and the ground reaction forces. The kinematic data provided consists on the trajectory of bony landmarks. This data was obtained using 10 synchronized cameras recording the trajectory of reflective markers placed on the subject skin with a sampling frequency of 120 Hz.

The gait kinematics data of two patients using instrumented hip implants, reported by *OrthoLoad* (Bergmann, 2008), is processed to set up kinematic simulations. The general anthropometric characteristics of the studied subjects are presented in Table 5.

A total of 18 markers are used to track the lower limb motion. The reflective markers placement follows the recommendations of the ISB (Wu et al., 2002), which certifies the necessary data quality. The evaluation of the anatomic points positions enables to define the positions of the anatomical segments and the joint centres. The marker set locations used to describe the motion of the lower limb in this work is illustrated in Figure 8.

The kinematic data is filtered using a 2nd order low-pass filter, since high frequencies are not related to the kind of movements that are under analysis, to eliminate noise. The cut-off frequencies selected are calculated using residual analysis (Winter, 2009).

1	RASIS right anterior superior iliac spine
2	LASIS left anterior superior iliac spine
3	RPSIS right posterior superior iliac spine
4	LPSIS left posterior superior iliac spine
5	RMCO right medial condylus femoris
6	RLCO right lateral condylus femoris
7	RMMA right medial malleolus
8	RLMA right lateral malleolus
9	RHEEL right calcaneal tubercle
10	RMET01 right metatasale I
11	RMET05 right metatasale V
12	LMCO left medial condylus femoris
13	LLCO left lateral condylus femoris
14	LMMA left medial malleolus
15	LLMA left lateral malleolus
16	LHEEL left calcaneal tubercle
17	LMET01 left metatasale I
18	LMET05 left metatasale V

Figure 8: Location of the eighteen markers placed on the subject's skin used to identify the biomechanical model body segments. The markers were placed according to the ISB recommendations. The markers acronyms are also presented, followed by the complete anatomical position description.

Table 5: General anthropometric data of the two studied patients.

Patient	Gender	Affected Leg	Age (year)	Weight (kg)	Height (cm)	Time post op. (months)
H2R	male	right	62	78	172	12
H1L	male	left	55	73	178	13

4.2. Motion Reconstruction

Once the kinematic data processing is finished, kinematic consistency must be ensured between the data provided and the model developed (Silva and Ambrósio, 2002). Note that the motion acquisition instrumentation introduces errors in the system that may lead to the violation of the biomechanical

system constraints. Furthermore, the LLEM does not have the same anthropometric measurements as the subjects under motion analysis, which leads to inconsistencies when matching the markers trajectories with the biomechanical body trajectories.

When reconstructing the motion in the LLEM, the angles related to the DOF of each joint, designated as driving angles, and the global position of the base body, i.e. the pelvis, are considered. The driving angles measurements starts with the identification of the joints centres. Most joint centres are defined as the midpoint between two reflective markers. In the case of the hip joint, implemented as a spherical joint, the joint centre cannot be found by palpation since it is not a superficial anatomical landmark. Accordingly, its location is estimated.

The location of the HJC is a crucial aspect of a kinematic analysis since it will be the origin point for hip rotation angles and, consequently, it has a strong repercussion in the accuracy of the contact forces calculated (Hara et al., 2016), to be discussed in Section 6.2.1, which are the thoroughly used for validation in this work. The HJC location is usually calculated using functional or predictive methods. The former consists on optimization procedures aiming to determine the centre of the limb spatial rotation (eg. Piazza et al., 2001) which can be challenging as it requires the recording of additional motions. Alternatively, predictive methods, consisting in regression equations based on anthropometric measurements, offer a simpler implementation while delivering good results. Hara et al. (2016) proposes a set of regression equations using the leg length, measured as depict in Figure 9, as a single predictor.
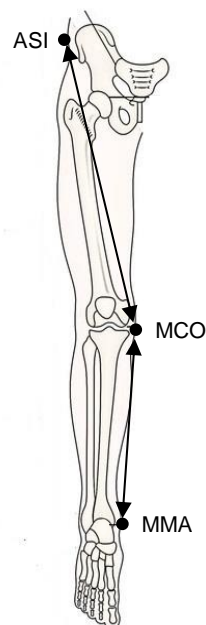
Figure 9: Leg length as the distance from anterior superior iliac spline (ASI) to medial malleolus (MMA) markers passing throw the medial femur epicondyle (MCO).

Hara et al. (2016) rational is that the leg length measurement is less affected by the soft tissues thickness than the pelvic depth and pelvic width, used in former HJC prediction equations (e.g. Harrington et al., 2007). In consequence, Hara et al. (2016) equations are selected in this work to predict the HJC of the subjects, i.e. in local pelvis body coordinates the location of the HJC is given by:

$$posterior - anterior\ direction: \quad HJC_x = 11 - 0.063\ LL$$

$$medial - lateral\ direction: \quad HJC_y = 8 + 0.086\ LL \qquad (18)$$

$$inferior - superior\ direction: \quad HJC_z = -9 - 0.078\ LL$$

where the leg length *LL* is in millimetres and the *x,y* and *z* correspond to the directions used to define the pelvis coordinate system in accordance with ISB (Wu et al., 2002).

From the positions of bony landmarks, each anatomical segment coordinate frame is computed following the recommendations of the International Society of Biomechanics (Wu et al., 2002). The evolution of the angles between anatomical segments associated with the DOF of the biomechanical system are measured by processing the reflective markers acquired kinematics. Subsequently, the angles measured are prescribed in the LLEM by using rotational drivers. The angles measured correspond to the time dependent terms $q_i^m(t)$ of the prescribed motion constraint Equation (8) and $\theta(t)$ of the rotational driver constraint Equation (9). To ensure total consistency so the Equations (10), (14) and (12), described in Section 3.3 must be solved.

The hallux marker is not present in the *OrthoLoad* kinematic data. However, its trajectory is considered important for a correct prediction of the internal forces since there are several muscles whose insertion point is located at the toe. Note that the motion of the toes may influence the moment arm of these muscles and, therefore, influence the internal forces developed. To reproduce the halluces kinematics, the motion of the toes is measured from a different subject in the Lisbon Biomechanics Laboratory (LBL) and is then prescribed for the *OrthoLoad* kinematic data. This approach is selected since the gait kinematics is considered as a standardized motion (Kadaba et al., 1990; Sheffler and Chae, 2015).

4.3. Application to the Gait Analysis Study

The gait stride can be divided into two phases: stance phase (ipsilateral foot contacting the ground) and swing phase (ipsilateral foot not contacting the ground). The stance phase can be divided into sub-phases: (1) the initial foot contact with the ground, heel strike, (2) the mid-stance phase that ends when the centre of gravity is over the ipsilateral foot, entering (3) the terminal stance when the heel is taking of the floor and ending in (4) the pre-swing phase in which the anterior foot is still contacting the floor. The swing phase can be sub-divided in three categories: (1) initial swing from the toe off until the foot passes the adjacent feet entering (2) the mid-swing phase that ends with vertical tibial position and finally, (3) the terminal-swing that ends when the heel strike (Bonnefoy-Mazure and Armand, 2015; Sheffler and Chae, 2015). Gait is characterized by alternating periods of double support and single support, as shown in Figure 10.

In the interest of confirming the validity of the computed kinematics, the driving angles measured for the two *OrthoLoad* subjects are compared against the data of Kadaba et al. (1990). The referred literature describes several gait analyses for a number of patients using the clinical reflective markers procedure, to evaluate the angular motion of the lower limb joints. In **Error! Reference source not found.**, the joint

angles obtained for both patients are compared with Kadaba et al. (1990) measurements, presented in a grey shadowed region.
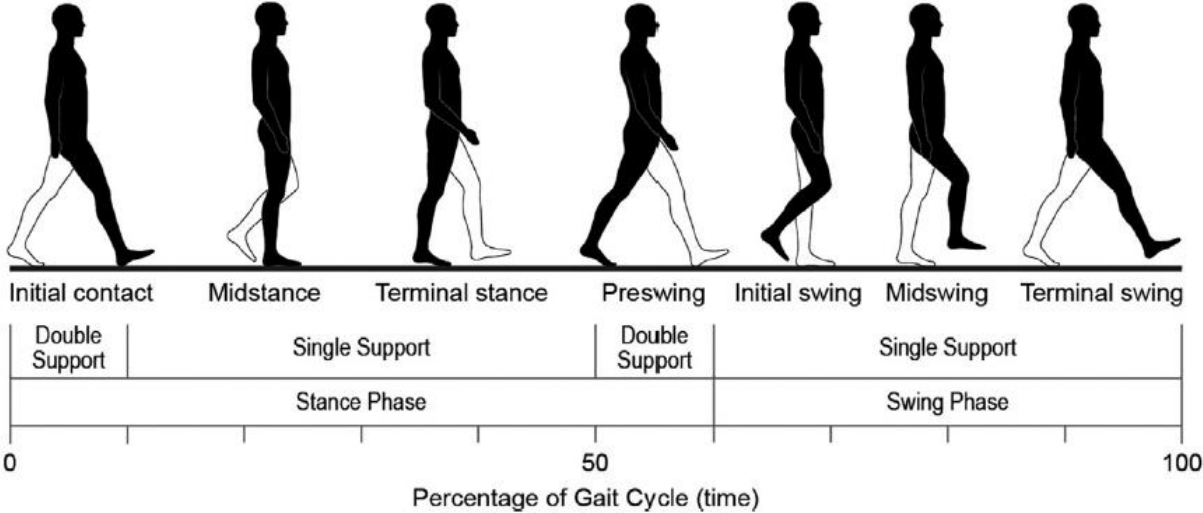
Figure 10: Gait cycle and respective phases. Image from (Sheffler and Chae, 2015).

Despite some minor differences existing, the results obtained are, overall, in good agreement with literature (Arnold and Delp, 2011; Kadaba et al., 1990). It is important to notice that the HJC is defined differently in Kadaba et al. (1990), which is shown by the authors to have a noticeable influence in the hip angles measured. The knee axis of rotation may also impact the joint angle measurements. Additionally, note that the joint angle ranges and patterns are highly sensitivity to the patients' age and gender (Sutherland, 1997). Thus, the direct comparison of data obtained from the older subject, in *OrthoLoad*, with that from younger subjects (Kadaba et al., 1990) is expected to reflect some of these differences.
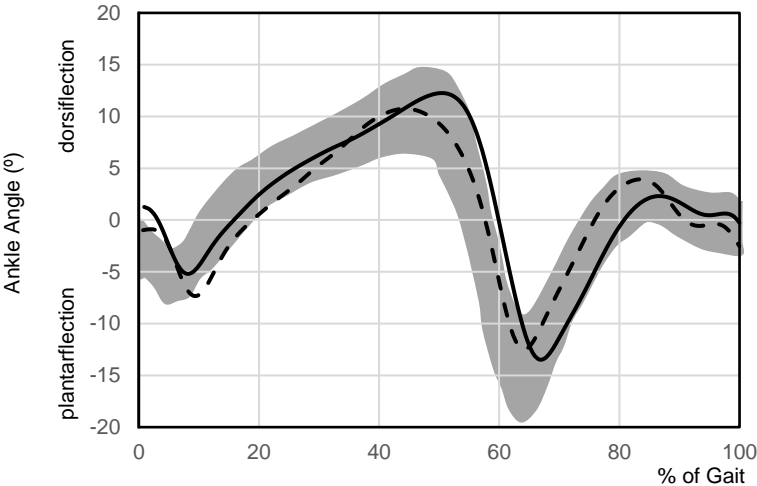
Figure 11: Joint angles measured for the patients *H2R* (solid line) and *H1L* (dash line). The shaded area corresponds to the joint angle ranges reported by Kadaba et al. (1990). These joints angles were prescribed in the LLEM kinematic simulation.
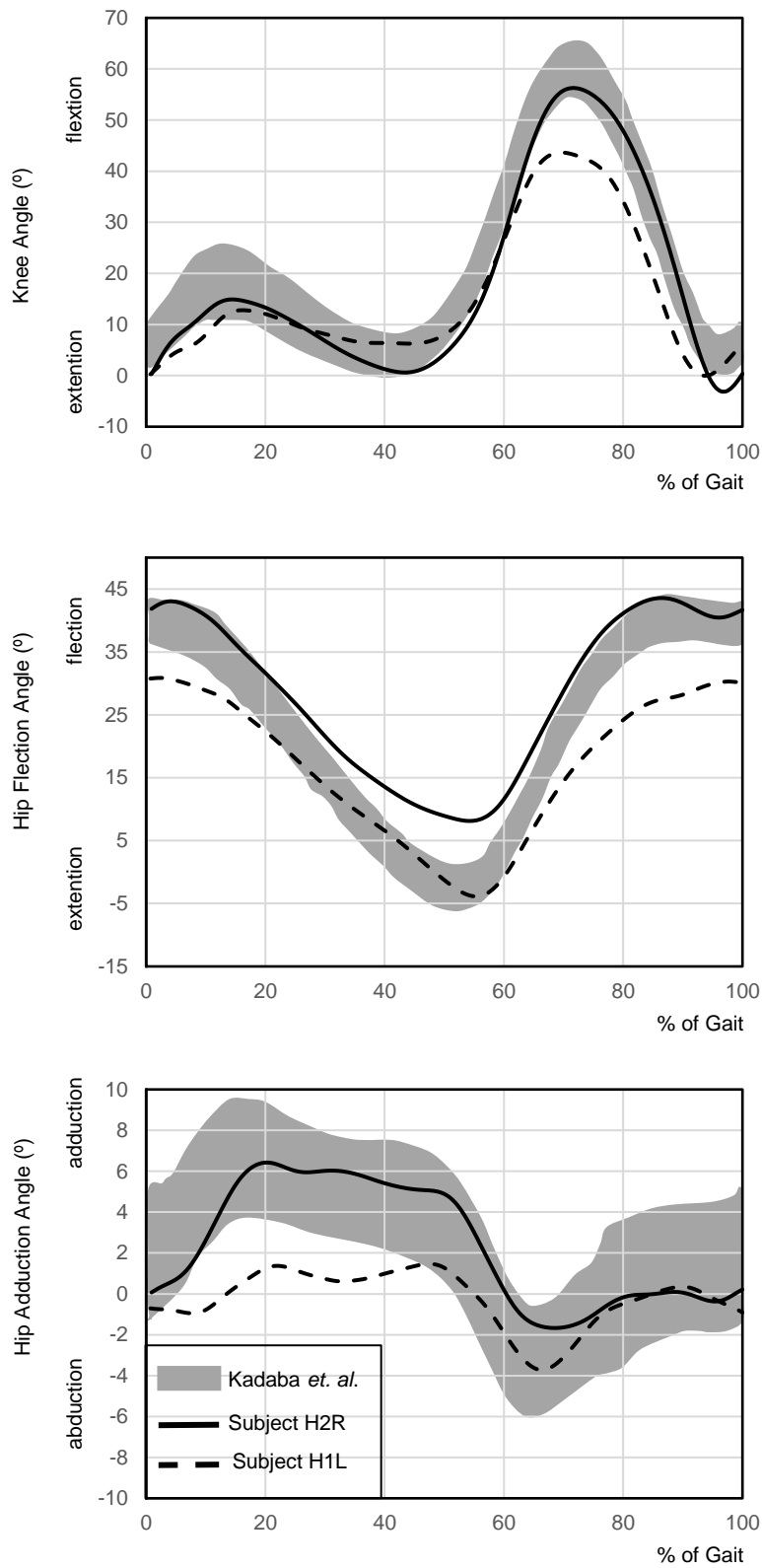
Figure 11: (cont.)

4.4.   Kinetic Data by OrthoLoad

The ground reaction forces are the contact forces transmitted between ground and feet during the stride phase. Together with the gravitational forces, they represent the externally applied forces in the biomechanical system during normal gait and represent the total forces acting on the lower limb system. *OrhoLoad* measures the GRF and their point of application using 6 DOF force plates (*AMTI, Watertown Ma*). The data provided comprises the magnitude of the forces in the three related directions of the reference frame and the moments-of-force in relation to the force plate coordinate system, which allows the calculation of the centre of pressure (COP) and subsequent force point-of-application. The force-plates referential is depicted in Figure 12.
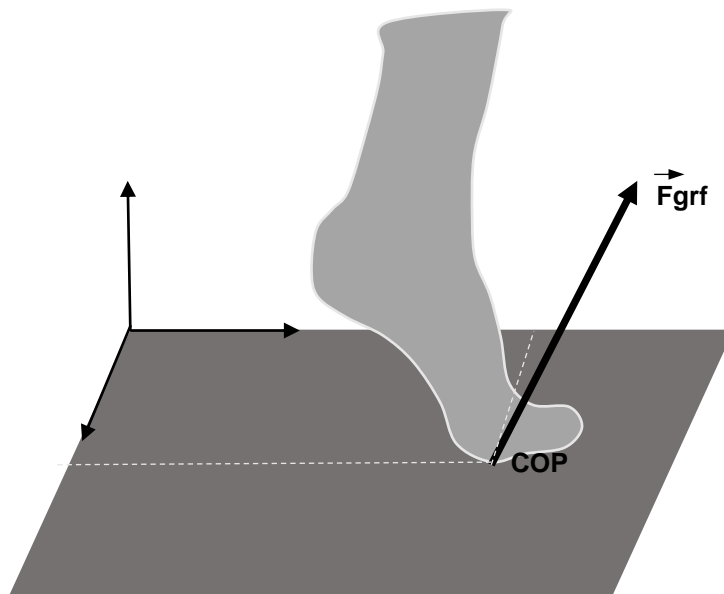
Figure 12: Ground Reaction Forces representation and respective reference frame.

The GRF, for both studied subjects, is presented in Figure 13. Only the GRF on the instrumented leg are presented for the stride phase, for a better visualisation. The generation of the GRF begins at the instant when the foot contacts the ground, in the double support phase. At the same time the force magnitude rises rapidly since the body weight is being transferred from the contralateral leg to the new supported leg, attaining a force peak due to the impact force of the contacting foot. After the first peak, the force tends to decrease, since in this phase the contralateral leg is in the swing phase, helping the movement of the body, and the ipsilateral is in a stable position. The next phase is characterized by a further increase in strength, while the heel lifts away from the ground and the system is on double support once more (Bonnefoy-Mazure and Armand, 2015). This gives origin to a typical force magnitude pattern having a double bump that can be observed in Figure 13, characterized by a dominant *z* direction component. The forces reported are in agreement with those presented in the literature (Winter, 2009).
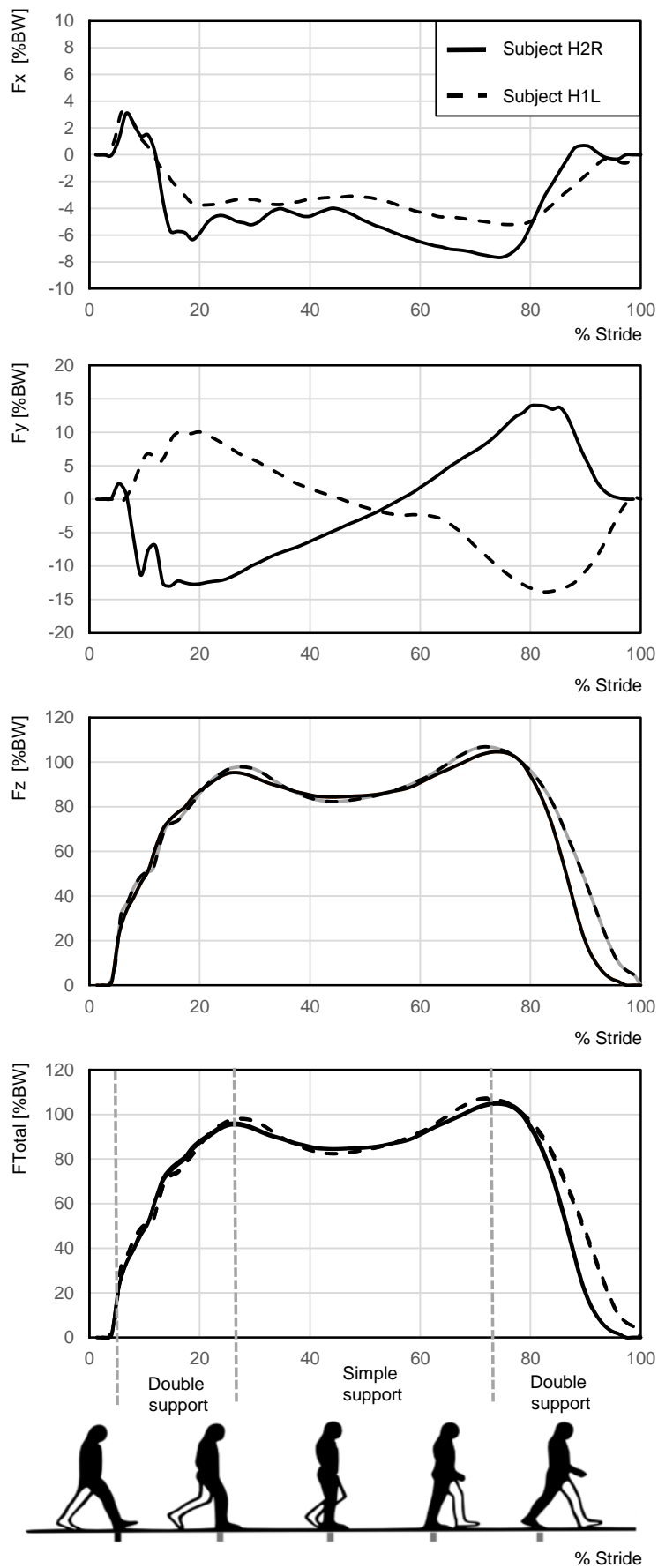
Figure 13: Representation of the three components (x,y,z) and total magnitude of the GRF for the subjects H2R and H1L during the stance phase.

The COP can be obtained from the moments-of-forces reported, considering that:

$$COP_x = -\frac{M_y}{F_z} \quad ; \quad COP_y = \frac{M_x}{F_z} \qquad (19)$$

The COP calculated is used to determine the GRF point of application. The position calculated is obtained in the force-plate reference frame, being a transformation of coordinates to the global reference frame performed to check if the COP is consistent with the position of the metatarsals. The force may be applied on the foot or on the toes. The identification of the body in which the force is applied is important for the assemblage of the global forces vector **g** (Sheffler and Chae, 2015).

Being the HCJ one of the results of the inverse dynamic analysis, the major advantage of the *OrthoLoad* data is to allow the comparison of these findings with the measured contact joint forces, provided for the captured and reconstructed motion of the subject. This comparison can determine if the predicted HCF are within the range of those found *in vivo* and help validating the lower limb model. In addition, they also serve as a reference to identify improvements in inverse dynamics optimization, when assessing the related parameters. The HCF measured by *OrthoLoad* are represented in Figure 14, being the *x* direction correspondent to lateral direction, *y* the anterior-posterior and *z* the inferior-superior, based on the femur based coordinate system proposed by the ISB (Wu et. al. 2002).
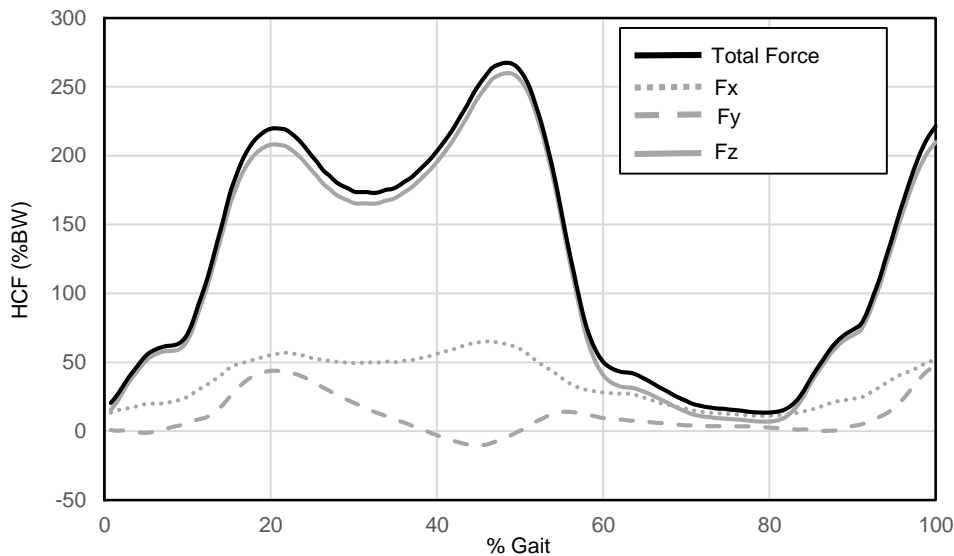
Figure 14: Hip contact force reported by *OrthoLoad* (Bergmann, 2008) in the three components of the force-plate reference frame *(x,y,z)* and total magnitude.

5. Inverse Dynamic Analysis of Indeterminate Biomechanical Systems

The dynamics of a multibody system is simulated by solving either a forward or an inverse dynamic analysis. The former is performed when the aim is to predict the system motion when the applied forces and torques are known. However, when studying biomechanical systems where the developed internal forces and torques are difficult to measure directly and are usually the object of study, an inverse dynamic analysis can be a more suitable approach (Quental et al., 2016).The analysis consists in obtaining the joint reaction and driving forces that the biomechanical model must produce to be mechanically consistent with a pre-defined dynamics response, i.e. a given motion under the action of externally applied forces.

In the first section of this Chapter, an overview of an inverse dynamic analysis procedure is presented. Next a description of the muscle actuators, which are included in the biomechanical model to mechanically represent the muscle apparatus, is presented. In the third section, the dynamic properties of the muscle tissue are discussed. The following section describes the muscle force sharing problem, and finally, in the last section, the cost function, whose study constitutes one of the objectives of this work, is described.

5.1. Inverse Dynamic Analysis

An inverse dynamic analysis requires consistent kinematic data as input, as described in Chapters 3 and 4. For this analysis, the equations of motion, expressed in Equation (17), are solved using the consistent kinematic data, the global biomechanical system mass matrix, and the vector of externally applied forces measured using force plates (see Section 4.4).

When considering only the kinematic joint constraints, the equations of motion include n equations for m unknowns, i.e. m-n degrees of freedom, so a solution cannot be obtained. One approach to solve the system equations is to consider joint actuators, using the rotational driver described in Section 3.2.5, and introducing in the system m-n equations so that the problem becomes determinate. Consequently, the equations of motion can be computationally solved. The solution obtained, i.e. the Lagrange multipliers, is not related to the actual muscular forces but to joint torques needed to perform the studied motion. This formulation is known as a determinate inverse dynamic analysis.

An alternative approach, representative of the musculoskeletal system, is to consider the muscles as one or several two-point actuators. The contribution of each muscle is added to the system as a constraint equation. Because the number of muscles is much larger than the number of DOF, the problem becomes indeterminate since there are more unknowns m than equations n. This formulation, known as indeterminate inverse dynamic analysis, is explained in detail in the following sections.

In the present work, the muscles of the leg under study, that is, the leg comprising the instrumented prosthesis, are considered as two-point actuators in order to estimate correct hip joint reaction forces.

In the contralateral leg, joint rotational drivers are considered for the sake of computational simplicity. The upper limb musculoskeletal structure is disregarded (Arnold et al., 2010; Heller et al., 2001; Modenese et al., 2011; Moissenet et al., 2014).

5.2. Muscle Actuators

In order to estimate muscle forces, muscles are included in the biomechanical system as two-point kinematic driver actuators, with a constraint equation associated to each muscle. The driver constraint equation is expressed as a straight line, with an origin P_i of a rigid Body i, and an insertion P_j of a rigid Body j, as depicted in Figure 15, being its length allowed to change in time (Nikravesh, 1988; Silva and Ambrósio, 2003). Mathematically, this muscle constraint is expressed as:

$$\boldsymbol{\phi}^{(ma,1)} = (\mathbf{d}^T\mathbf{d})^{\frac{1}{2}} - L^m(t) \tag{20}$$

where $L^m(t)$ is the muscle length variation over time that is obtained experimentally by analysing the system's kinematics and $\mathbf{d}$ is the global vector between the muscle origin P_i and insertion P_j, expressed as:

$$\mathbf{d} = \mathbf{r}_j + \mathbf{A}_j \mathbf{s}_j'^P - \mathbf{r}_i - \mathbf{A}_i \mathbf{s}_i'^P \tag{21}$$

where $\mathbf{r}_i$ and $\mathbf{r}_j$ are the global position of bodies i and j, respectively, and $\mathbf{s}'^{P_i}$ and $\mathbf{s}'^{P_j}$ are the local coordinates of the origin and insertion on the respective bodies, multiplied by the rotation matrices $\mathbf{A}_j$ and $\mathbf{A}_i$.
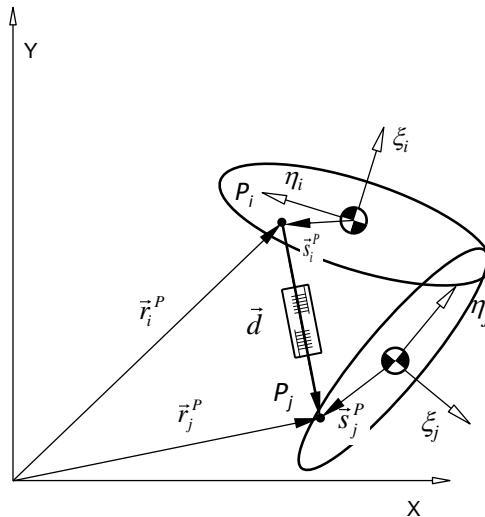
Figure 15: Muscle actuator with vector $\mathbf{d}$ from the origin P_i to the insertion P_j.

The *Jacobian* matrix*, right-hand side* of the velocity and acceleration kinematic equations can be obtained by deriving the constraint Equation (20). The interested reader is referred to the reference (Quental, 2013) for a more detailed description of the process.

Muscles with a complex path require more than a single actuator for an accurate representation. They are modelled as a sum of two-point actuators connecting intermediate points of the muscles, called *via points*, that represent the muscle's wrapping around the bones and contacting muscle (Garner and Pandy, 2000).

Each muscle actuator is associated with a Lagrange multiplier, linked with a muscle force. The constraint equation in added to the system of motion equations, expressed by Equation (17), resulting in a higher number of elements that transmit forces than equilibrium equations. Consequently, the problem becomes indeterminate, i.e. it has more unknowns than equations, thus having an infinite number of solutions.

5.3. Dynamics of the muscle tissue

The muscular force is produced when muscle contraction is stimulated by electrical impulses, emitted by the central nervous system, leading to calcium ions pumping from the sarcoplasmic reticulum. These calcium ions interact with the troponin and tropomyosin proteins that change the shape of the myofibril bundles, and allow myosin to bind with actin, forming a cross-bridge. The myosin heads then tilts, pulling the actin, causing the muscle to contract (Hall, John E. ; Guyton, 2016). Cross-bridges are established sequentially to generate force. The process briefly explained here corresponds to the *sliding filament theory,* the most widely acceptable theory on how muscles contract (Cooke, 2004).
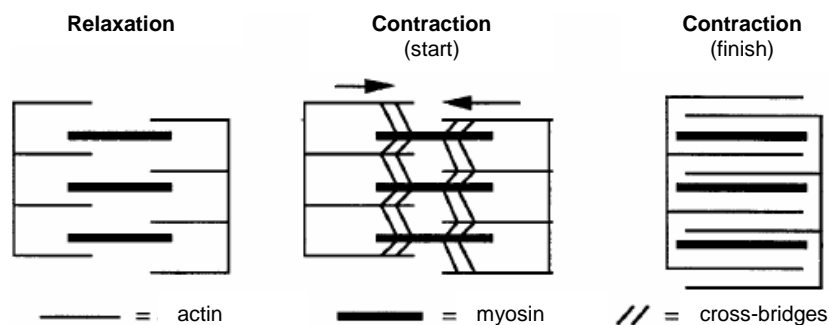
Figure 16: *Sliding filament theory* of muscle contraction. The actin filaments slide over myosin filaments. and form cross-bridges. Figure adapted from (Dicarlo et al., 1999).

The total force produced by a muscle includes two components: the passive tension and the active tension. The first component is related with the muscle tissue elasticity and is produced when the muscle length is greater than its resting length, l_m^0, being proportional to the fibre length. The active force is the actual force generated by the muscle's contractile mechanism following the establishment of cross-bridges. The active force that a muscle produces is related not only with its length but also with its velocity of contraction. This force is maximal at muscle lengths proximal to the optimal muscle fibre length, since the maximum overlapping of actin and myosin filaments originating cross-bridges is

achieved in this position. With large deviations from this position, shortening or extending the muscle, the number of cross-bridges falls, decreasing the magnitude of the active-force (Quental, 2013). When the contracting muscle reaches half of its resting length l_m^0 it is not physiologically capable of further contracting and therefore cannot generate active force (Arnold et al., 2013). The same behaviour is observed when the muscle is extending and reaches a length superior to one and a half of its resting length, l_m^0. The muscle property described, known as force-length relationship, is illustrated in Figure 17.
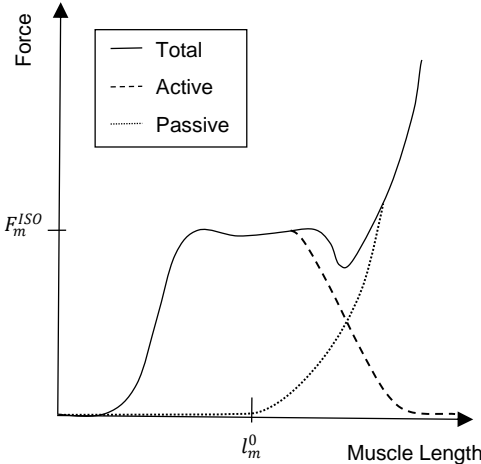
Figure 17: Force-length property.

When the muscle is not changing length, i.e. in an isometric contraction, the maximum force developed is the so-called maximum isometric force F_m^{ISO}. In the case where muscle is shortening, i.e. in a concentric contraction, as velocity increases the force that the muscle can produce decreases due to the protein reduced capacity to establish cross-bridges (Quental, 2013). When the muscle is extending, in an eccentric contraction, the force produced is increasing with velocity until it reaches a new maximum, that can be higher than the maximum isometric force. Figure 18 illustrates this muscle property known as force-velocity relationship.
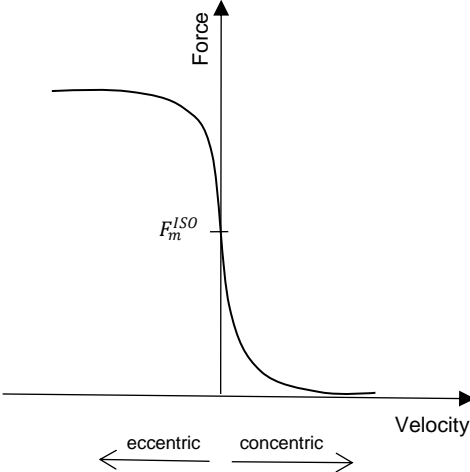
Figure 18: Force-velocity property.

To model the muscle tissue, two different types of dynamics can be considered: activation dynamics and contraction dynamics. The activation dynamics describes the delay between the emission of the neural excitation signal by the central nervous system and the corresponding muscle activation. The contraction dynamics describes the transformation of the activation state into mechanical force development, a biological process that is described in the beginning of this section. A schematic representation of these processes is illustrated in Figure 19.
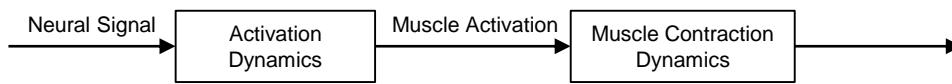
Figure 19: Dynamics of the muscle tissue, based on (Silva and Ambrósio, 2003).

To simulate the muscular contraction dynamics several mathematical models have been developed to represent the muscle-tendon mechanical behaviour and relate the muscular force to the movement of the musculoskeletal model system. In this study, the muscle is modelled using the Hill-type model presented in Silva and Ambrósio (2003) that proposes an arrangement of three active and passive mechanical elements, as shown in Figure 20 .
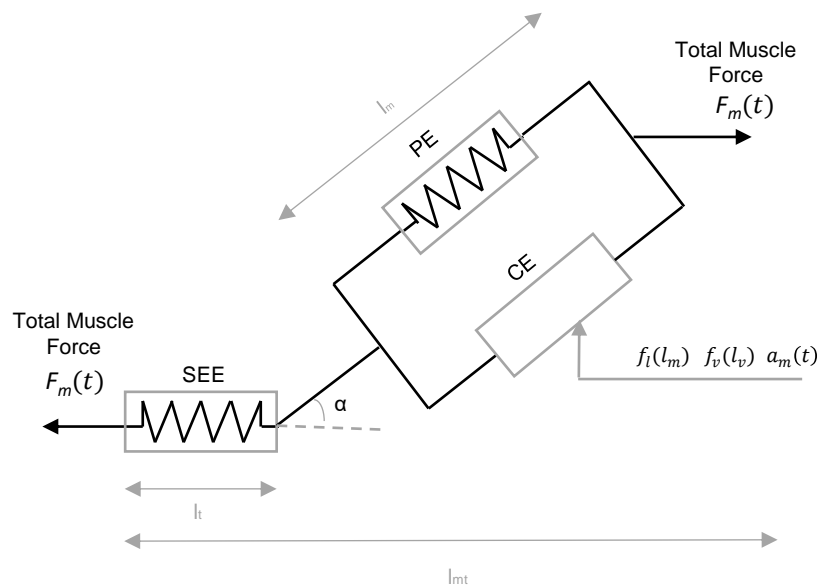
Figure 20: Muscle Model used to simulate the contraction dynamics (Hill-type)

The model consists in a contractile element (CE) that generates active force, in parallel with a passive element (PE) that represents the muscle fibres elasticity, and a non-linear elastic element (SEE) which represent the tendon. The pennation angle α is the angle between a fascicle's orientation and the tendon axis.

The Hill-type muscle model requires four parameters to determine the curves for active and passive force generation: optimal fibre length l_m^0, maximum isometric force F_m^{ISO}, pennation angle α and tendon-slack length l_t. These parameters are shown in the dataset used for modelling the biomechanical model (presented in Chapter 2).

The SEE element is associated with the non-linear stiffness of the tendon. Tendon elasticity is mainly critical for muscles with large tendons, like some of the muscles of the lower limbs. However, the complexity introduced in the system makes the computational procedure associated to the inverse dynamic analyses significantly less efficient. While studying the influence of the muscle model complexity on the muscle force sharing problem of the shoulder, Quental et al. (2018) reported that the simulation of tendon elasticity increased the computational time by more than 2000%. In force of the motion scenarios considered in this work, the elasticity of the tendons of the lower limb are neglected. Note that most studies also neglect tendon elasticity, supporting the suitability of this assumption. If the tendon does not vary its length, the muscle length can be directly calculated from the kinematic data, knowing the tendon slack length and considering that the tendon shortening velocity is null. Attending to Figure 20, the muscle length l_m is given by:

$$l_m(t) = \frac{l_{mt}(t) - l_t}{\cos\alpha} \tag{22}$$

where L^{mt} corresponds to the total length of the musculo-tendon complex.

The production of force with the CE is related with the overlapping of the contractile proteins actin and myosin. The force generated in the CE is a function of the maximal isometric force F_m^{ISO}, force-length relationship $f_l(l_m)$, force-velocity relationship $f_v(l_v)$ and activation $a_m(t)$, expressed as:

$$F_m^{CE} = \frac{f_l(l_m) \cdot f_v(l_v)}{F_m^{ISO}} a_m(t) \tag{23}$$

The force-length $f_l(l_m)$ and force-velocity $f_v(l_v)$ dependencies proposed by Kaplan (2000), based on experimental results, are considered here.

The PE element only produces force when the muscle length is greater than a given resting length l_m^0, i.e. the muscle is stretched, and therefore does not depend on muscle activation. This means that its force can the calculated directly by analysing the biomechanical model motion, using (Kaplan, 2000):

$$F_m^{PE}(l_m(t)) = \begin{cases} 0, & l_m^0 > l_m(t) \\ 8F_m^{ISO}\left(\frac{l_m}{l_m^0} - 1\right)^3, & 1.63l_m^0 \geq l_m(t) \geq l_m^0 \\ 2F_m^{ISO}, & l_m(t) > 1.63l_m^0 \end{cases} \tag{24}$$

The total muscle force F_m is computed by adding the contributions of the PE and CE element.

5.3.1. Muscles length during the gait cycle

The force-length and force-velocity relationships of a muscle are of extreme importance when evaluating muscle dynamics, since the force generated by the muscles is highly dependent on these quantities. When considering the tendon rigid, the muscle velocity and length can be directly measured by analysing the biomechanical system kinematics: the tendon slack length is considered constant and so the muscle fibre length only depends on the origin and insertion locations. Therefore, these properties are also evaluated and compared with literature (Arnold et al., 2013; Arnold and Delp, 2011). Figure 22 Figure 23 presents the normalized fibre length for both patient's gait cycles for the 20 muscles considered to take part in gait motion.

The majority of results are in accordance with the literature (Arnold et al., 2013; Arnold and Delp, 2011). The *tibialis anterior*, *extensor digitorum longus* and *biceps femoris LH* present a slight offset from the literature data. Nonetheless, the observed deviation should not be linked with an incorrect force prediction since the feasible operating region is located close to the plateau region of the force-length curve, as described in Figure 17, where the muscle is able to develop its maximum force. The *soleus*, *semimembranosus* and *semitendinosus* muscles present less consistent results since these muscles seem to operate in different regions of the force-length curve. In these cases, the muscle loses the capability to produce force when it is supposed to be important for an accurate gait motion. However, it is important to mention that the biomechanical model used in the literature does have differences with the model used in this work.
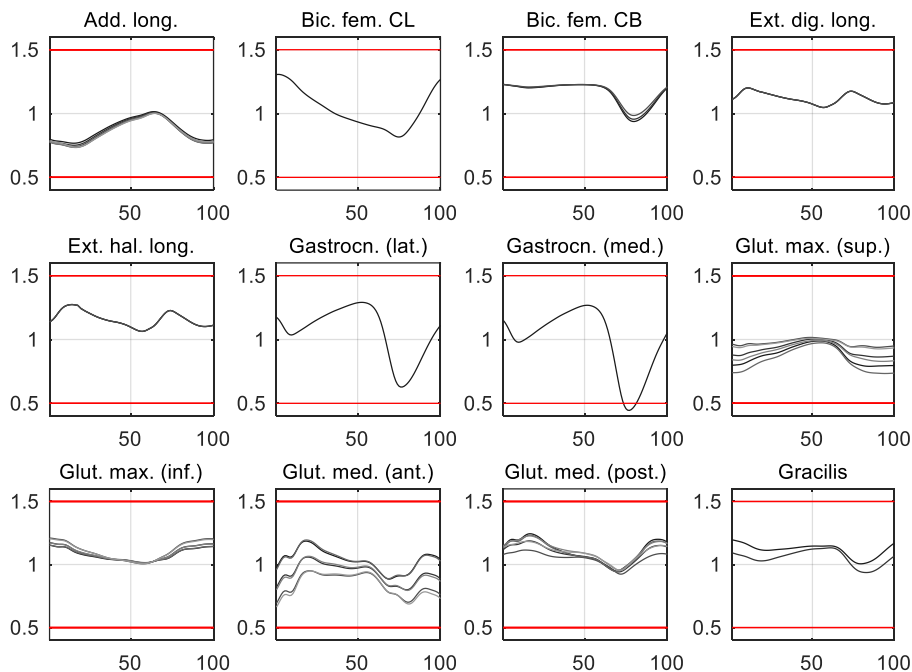
Figure 21: Normalized fibre length for the H2R patient gait cycle. For some muscles, several lines are plotted because they represent the behaviour of the different muscle bundles into which the muscle is discretized.

Iliacus (mid.)   Peroneus long.   Rectus fem.   Sartorius (prox.)

Soleus (med.)   Tibialis ant.   Tibialis post. (med.)   Vastus lat. (inf.)

Figure 22: (cont.)

LAdd. long.   LBic. fem. CL   LBic. fem. CB   LExt. dig. long.

LExt. hal. long.   LGastrocn. (lat.)   LGastrocn. (med.)   LGlut. max. (sup.)

LGlut. max. (inf.)   LGlut. med. (ant.)   LGlut. med. (post.)   LGracilis

LIliacus (mid.)   LPeroneus long.   LRectus fem.   LSartorius (prox.)

LSoleus (med.)   LTibialis ant.   LTibialis post. (med.)   LVastus lat. (inf.)
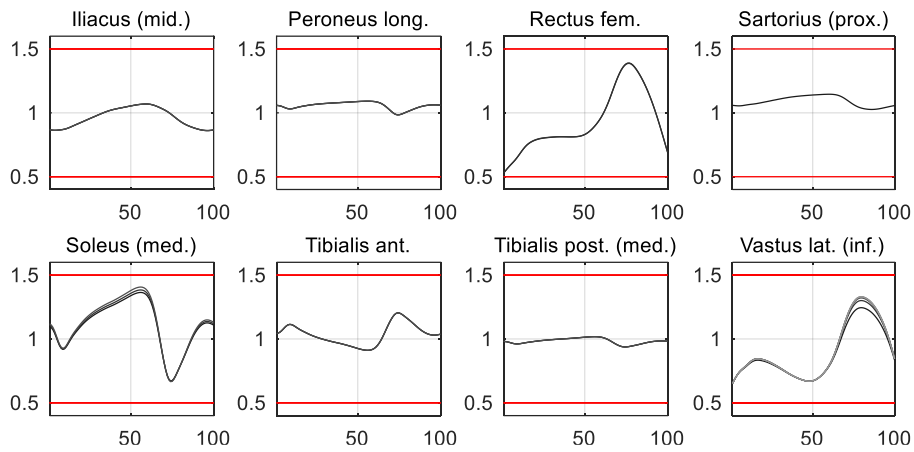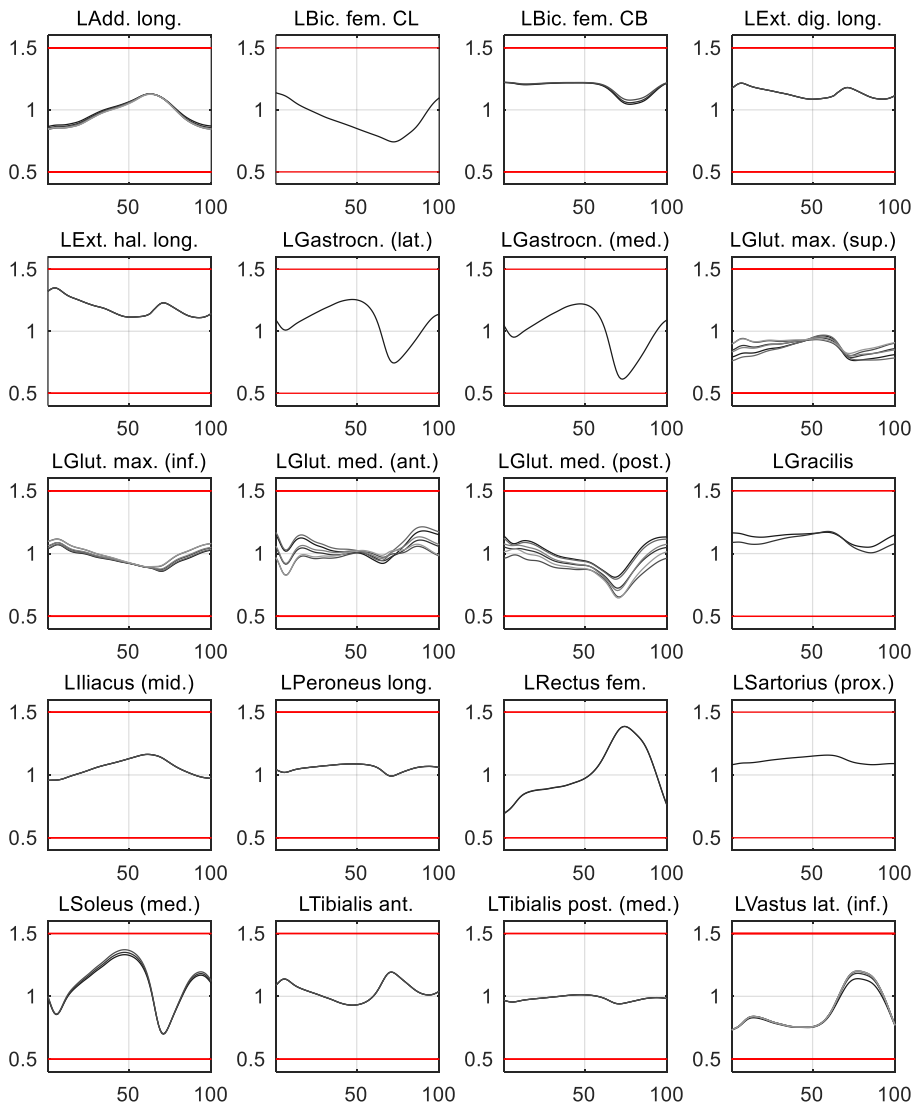
Figure 23: Normalized fibre length for the H1L patient gait cycle. For some muscles, several lines are plotted because they represent the behaviour of the different muscle bundles into which the muscle is discretized.

5.4. Redundant Muscle Force Sharing Problem

From a biological point of view, the indeterminacy of the musculoskeletal system means that any given movement can be achieved by recruiting different combinations of muscles, sets of muscles, or by applying different activation levels. In this respect the human locomotion system is redundant, i.e. different activation patterns can result in the same force moments acting on the biological joints. The muscle recruitment criteria is controlled by the central nervous system which, depending on the motion or posture to be achieved, selects the appropriate activation patterns.

The indeterminate problem described, usually referred in literature as ''the redundant muscle force-sharing problem'' (Yamaguchi et al., 1995), is generally solved using optimization procedures, which select the optimal solution from the infinite set of solutions. This solution minimizes a given cost function while satisfying the equations of motion and other physiological constraints.

The objective function is a mathematical expression that attempts to simulate the muscle recruitment criteria adopted by the central nervous system. However, presently, it is still uncertain how the exact control mechanism occurs *in vivo*. Therefore, the cost functions adopted in the literature are based on several assumptions. Different physiological criteria have been studied and presented in literature. Unfortunately, the majority of studies present purely mechanical cost functions that ignore the physiological capability and do not calculate the energy consumption (Tsirakos et al., 2017). On the contrary, it is now assumed that the main criterion of the central nervous system is to minimize the energy consumption (Alexander, 1997), and cost functions that take energy into account are expected to provide more realistic activation patterns.

The optimization problem described can be formulated as (Quental et al., 2015).

$$\text{minimize } J_E$$

$$\text{subject to } f_{mt} = \left(\mathbf{M\ddot{q}} + \ \boldsymbol{\Phi}_{\mathrm{q}}^{\mathrm{T}}\boldsymbol{\lambda} - \mathbf{g} \right)_t = 0 \tag{25}$$

$$0 \leq a \leq 1$$

where J_E denotes the objective function to be minimized, discussed further in Section 5.5, f_{mt} denotes the equations of motion that must always be fulfilled, and a the vector of the muscles activations. The inequality constraints ensure that the physiological properties of the muscles are also satisfied, in particular the activation range.

5.5. Cost Function

In the present work the muscle recruitment criterion adopted is an energy-related cost function based on physiological parameters proposed by Praagman (2008). This function, expressed in Equation (26), considers two biological processes that are assumed to be the major energy consuming mechanisms in the muscles: (1) the cross bridges detachment and (2) the calcium re-uptake..

$$J_E = \sum_{i=1}^{n} \dot{E}_{mi} = \sum_{i=1}^{n} (\dot{E}_{fi} + \dot{E}_{ai}) \tag{26}$$

The first process is related to the contraction dynamics, i.e. the activation state transformation into mechanic muscle force. This process is related to the distribution of attached cross-bridges in relation to the cross-bridge length and can be expressed as a product of the muscle force and muscle fibre length. This process is linearly related with muscle force generation. Longer muscle fibres have more sarcomeres in series and a higher number of cross-bridges can be established. Therefore, longer muscle fibres are associated with higher forces. The energy needed for the detachment of cross-bridges is assumed to be linearly dependent of muscle force. The quantity $\dot{E}_f$ is expressed as:

$$\dot{E}_f \sim l_m F_m = V_m \frac{F_m}{PCSA_m} \tag{27}$$

where V^m is the muscular volume and $PSCA^m$ the physiological cross-sectional area.

The second energy consuming process is related to the activation dynamics, defined as the phenomenon that occurs between the neural signal being developed in the central nervous system and the activation state of the muscle. The active state is associated with the absorption/reabsorption of calcium ions in the sarcoplasmic reticulum by a calcium pump and is proportional to the product of the total muscle volume and the active state. This quantity is related with the ratio of the muscle force to the maximal isometric force at the optimal fibre length, multiplied by the normalised force-length and force-velocity relationships, that is:

$$\dot{E}_a \sim V_m a_m(t) \sim V_m \frac{F_m}{F_m^{ISO} f_l(l_m) f_v(l_v)} \tag{28}$$

The energy required for the calcium re-uptake is not exactly known. However, it is assumed to be a non-linear relationship with muscle force. This assumption is made based on *in vitro* studies where it is found that this energy is linearly related with the stimulation frequency. On the other hand, muscle force is not linearly related with stimulation frequency (Blinks et al., 1978). The higher the muscle frequency, the greater is the difficulty of calcium ions to bind with actin and therefore the higher is the energy consumed. Hereupon, using a polynomial approximation of second order, the quantity $\dot{E}_a$ can be rewritten as:

$$\dot{E}_a = a_0 + a_1 V_m \frac{F_m}{F_m^{ISO} f_l(l_m) f_v(l_v)} + a_2 V_m \left(\frac{F_m}{F_m^{ISO} f_l(l_m) f_v(l_v)} \right)^2 \tag{29}$$

The energy-related cost function proposed by Praagman (2008) is the sum of the two processes, and can be written as follows:

$$\dot{E}_m = \dot{E}_f + \dot{E}_a = c_1 V_m \frac{F_m}{PCSA_m} + c_2 V_m \frac{F_m}{F_m^{ISO} f_l(l_m) f_v(l_v)} + c_3 V_m \left(\frac{F_m}{F_m^{ISO} f_l(l_m) f_v(l_v)} \right)^2 \tag{30}$$

where the values of the constants c_1, c_2 and c_3 are weight values that determine the contribution of each term in the process. The proposed cost function comprises two linear terms and one quadratic term. According to the literature (Crowninshield and Brand, 1981; Praagman, 2008), non-linear cost functions lead to muscle synergy, i.e. co-activation of muscles.

Although the energy consuming processes are thoroughly described in Equation (30), the rational for selecting the weights of each one of them, c_1, c_2 and c_3, are not reported. One of the goals of this work is to find a rational for their selection, being this discussed in Chapter 6 of this thesis.

6. Solution of the muscle force sharing problem

The discussion on the muscle load sharing problem, and the detailed description of an energy-related cost function used to solve the indeterminacy, has been done in Chapter 5. The present chapter focuses on an evaluation of the contribution of the weight values that quantify the relative contribution of the processes incorporated in Praagman (2008) cost function. The aim is to estimate the contribution of the weight factors for solving the muscle force sharing problem that can lead to improved HCF predictions, i.e. closer to those measured *in vivo*.

In the first section, the muscle force sharing problem implementation details are discussed, as well the details concerning the procedures adopted for the identification of the improved weight factors. In the second section the solution of the indeterminate problem solved using the cost function with the weight factors defined according to Praagman (2008) recommendations, herein called standard parameters, is discussed. The individual contribution of each cost function term is discussed. Next, the sharing force problem is solved for different combinations of the weight factors by performing a grid search where the parameters are varied within a selected range. Considering a two-level optimization approach, further detailed later, new weight factors are sought by minimizing the error between the computational and experimental HCF. Next, the weight factors optimization results are discussed. In the last section of the present Chapter, the muscle force and activation patterns obtained are also presented and discussed.

6.1. Muscle Force Sharing Problem Simulations Details

Knowing that the muscle force redundant problem can be solved by minimizing the energy-related cost function proposed by Praagman (2008), which is parametrized with three weight factors, Equation (30) is re-written in such way that the relative contribution of the terms is determined only by two weight factors (Nikooyan et al., 2013). The cost function can be normalized by one of the weight factors and the physical solution obtained, i.e. minimum muscular energy consumption, remains unchanged:

$$\dot{E}_m = \frac{c_1}{c_1} l_m F_m + \frac{c_2}{c_1} V_m a(t) + \frac{c_3}{c_1} V_m (a(t))^2 \Leftrightarrow \tag{31}$$

$$\dot{E}_m = l_m F_m + wf_1 V_m a(t) + wf_2 V_m (a(t))^2 \tag{32}$$

Because the first term of the objective function is much larger than the remaining terms, a scaling factor of 10^6 is considered to allow all terms to present similar orders of magnitude. Thus, in the following sections, for simplicity, the contributions of ω_1 and ω_2 are discussed, instead of the non-scaled weight factors wf_1 and wf_2, where:

$$wf_{1,2} = \omega_{1,2} \cdot 10^6$$

The indeterminate muscle force sharing problem is solved for subjects *H2R* and *H1L* using the optimization formulation presented in Equation (25) while minimizing the objective function described in Equation (32).

A static optimization procedure is selected to solve the problem, meaning that the muscle load sharing problem is solved for each frame individually. When solving the problem using the standard parameters the problem is solved for every instants of time, i.e. for a time period of 0.01 s. However, in Sections 6.3.2 and 6.3.3, the muscle force sharing problem is solved multiple times. Thus, for lower computational time, when carrying the grid search and the two level optimization only one in each 4 time frames are evaluated, meaning a time period of 0.04 s.

When modelling the muscle tissue, the tendon is considered rigid, as discussed in Chapter 5, and the activation dynamics is neglected, for the sake of computational efficiency. In fact, when considering static optimization, is it not possible to simulate activation dynamics since this is a time dependent physiological process. To account for activation dynamics, the problem must be solved using dynamic-like optimization methods, incurring more computational cost. Nevertheless, for normal gait, the dynamic optimization approach is expected to have little influence on the results (Anderson and Pandy, 2001). In contrast, the force-length and force-velocity properties are included in the modelling, to provide a better representation of the muscle tissue, given that they do not require a large computational cost.

The numerical HCFs are normalized by the LLEM total body weight while the HCF measurements are normalized by the subject's weight. To quantify the similarities between the numerical HCF curve shape and that measured *in vivo*, three indicators are used: (1) root mean square error (RMSE), (2) relative deviation between force peaks (RDP), equivalent to the difference between the numerical and measured HCF at maximum peaks, and (3) the *Fréchet* distance (FD), which is another measure of similarity between two curves[1].

The RMSE is calculated between the model-estimated HCF and the *in vivo* measurements. The RDP is defined as the difference between calculated and measured force, normalized to measured force. These two indicators are used in other studies (Heller et al., 2001; Modenese et al., 2011; Nikooyan et al., 2013). The FD indicator is not found in previous studies concerning HCF comparison, but being a measure of similarity between curves its an interesting goodness-of-fit measurement between numerical and measured HCF.

---

[1] The *Fréchet* distance between two curves is the maximum distance that a point on the first curve must travel as this curve is being continuously deformed into the second curve. The interest reader can consult the mathematical formulation and other aspects in (Alt and Godau, 1995)

6.2. Standard Problem Solution

In this section, the weight values used, ω_1 and ω_2, are obtained following the recommendations proposed by Praagman (2008), which states that weights factors should lead to an equal distribution of the linear and non-linear terms, at 50% of activation. This recommendation results in the following weight factors:

$$\omega_1 = 0.33 \quad ; \quad \omega_2 = 0.66$$

The HCF obtained in the model are compared to those measured *in vivo,* as depicted in Figure 24.
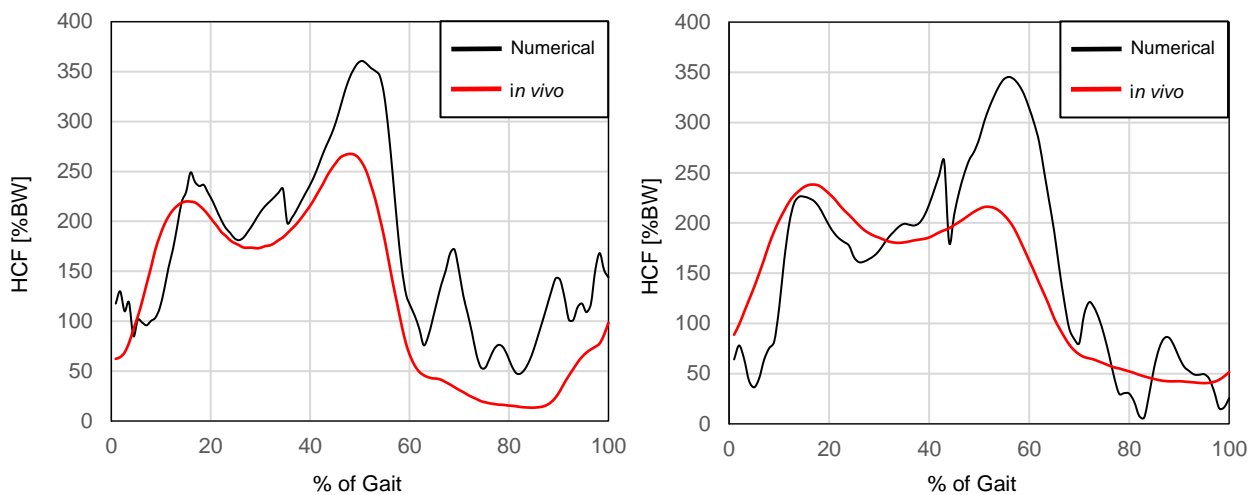
Figure 24: HCF obtained when using the standard parameters in dark line for the model of the (a) H2R patient and (b) H1L patient during a gait cycle and *in vivo* measurement in grey line.

The comparison revealed good agreement both in pattern and magnitude for the obtained and measured HCF. The deviations in shape between the forces in the model and those obtained *in vivo* are consistent with those presented in the literature (Heller et al., 2001; Modenese et al., 2011; Stansfield et al., 2003). In particular, the second force peak, presented at 55% of the gait cycle, is over-estimated for both patients studied. Table 6 presents the three goodness-of-fit indicators obtained considering the standard weight factors.

Table 6: RMSE, RDP and FD for H2R and H1L patients forces predictions for cost function using the standard parameters.

Subject	RMSE [%BW]	RDP [%Exp. peak]	FD [%BW]
H2R	63,3	25,9	94,7
H1L	68,8	30,5	112.8

6.2.1. Sensitivity of HCF to modelling assumptions

The numerical HCFs present some irregularities and peaks that do not occur *in vivo*, as depicts in Figure 24. The same is also found in other computational studies in the literature (Fraysse et al., 2009; Heller et al., 2001; Modenese et al., 2011; Moissenet et al., 2014; Rane et al., 2019; Stansfield et al., 2003). This behaviour is also observed in the muscle activation patterns and forces. In order to study the impact of the modelling assumptions on the HCF predictions, different modelling conditions, regarding the optimization method and the muscle properties, were compared. Considering the data of the subject H2R, the following modelling conditions were evaluated:

(1) RT, SO and disregard of force-length and force-velocity property and ignoring activation dynamics

(2) Similar conditions as in (1), but the force-length property is considered.

(3) The tendon element remains rigid but both force-length and force-velocity relationships are considered. Static optimization is used to solve the force load sharing problem. This corresponds to the modelling conditions used in last and following sections.

(4) Similar conditions as in (3), but the Window Moving Inverse Dynamics Optimization (WMIDO) method is used to solve the force load sharing problem (Quental et al., 2016). The WMIDO solves the indeterminate muscle force sharing problem simultaneously for *n* instants of time considering a window of *n* frames that moves forward iteratively. This method allows the use of time-dependent physiological criteria and constraints.

(5) Similar conditions as in (4), but the activation dynamics is simulated.

The HCFs predicted considering all these modelling conditions are presented in Figure 25.
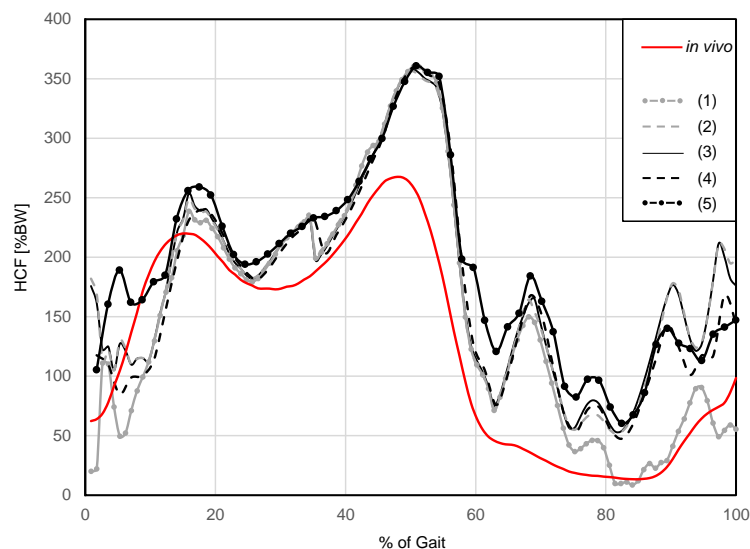
Figure 25: HCF prediction for the different modelling conditions described. The numbering corresponds to the same used for listing the different conditions. The *in vivo* forces are illustrated using a red line.

The rapid changes in magnitude are observed for all the simulations, as observed Figure 25, even when considering the most complex model, i.e. dynamic simulation and considering activation dynamics. The modelling aspects don't have an impact on the numerical HCF irregularities. Therefore, no clear conclusions are drawn for the origin of the peaks.

A parameter that shows evidence to have a considerable impact on HCF predictions is the location of the HJC. Previous studies have shown that changes in hip joint geometry and location have an influence on the kinematics and kinetics of the biomechanical system (Lenaerts et al., 2008). For example, a 3 cm misallocation of the HCF has been shown to lead to a 50% difference in mean flexion-extension hip moment, producing a significant difference in the predicted HCF (Stagni et al., 2000). Figure 26 compares the HCF obtained for the same subject when using two different HJC prediction methods. Harrington et al. (2007) proposed a set of regression equations relating the pelvic depth and pelvic width with HJC. Nevertheless, since these equations are based of magnetic resonance imaging evaluation, their claimed accuracy may not translate to the clinical reflective markers setting because of the soft tissues thickness between the anterior superior iliac spine (ASI) and posterior superior iliac spine (PSI) bony landmarks. Hara et al. (2016) propose another set of regression equations using the leg length as a single predictor. Hara et al. (2016) rational is that this measurement is much less affected by the soft tissues thickness, as supported by their study in which different regression equations were evaluated.

The method by Hara et al. (2016) predicted that the coordinates of the right HCJ of the H2R subject are [-0.0432, -0.0796, 0.0820], expressed in the pelvis reference frame. Considering the standard weight factors, this prediction of the HCJ leads to a HCF with an RMSE of 64,10% with respect to the *in vivo* data. The equations proposed by Harrington et al. (2007) predicted the coordinates of the HJC to be [0.00612, -0.0963, 0.1013], giving origin to contact forces with a RMSE of 112,18%. The application of the predictive method of Harrington et al. (2007) results in a 75,02% increase in RMSE. Considering that the method proposed by Hara et al., (2016) generates a system kinematics and measured driving angles with better agreement with the literature (Arnold and Delp, 2011; Kadaba et al., 1990), that can be observed in Figure 27, which also seems to allow a better estimation of the HCF, this method seems to be superior to that of Harrington et al. (2007). Considering these results, the predictive equations of Hara et al. (2016) are adopted. When the regression equations of Harrington et al. (2007) are applied in this work, the HJC prediction lead to inconsistent motion. When the angles measured are directly prescribed the trajectory of the model feet interfere with each other, leading to an unrealistic overlap of the anatomical segments. Despite not being addressed, note that muscle forces are also sensitive to the modelling decision concerning the location of the HJC, being further investigations on this issue required. Additionally, it is important to notice that the hip arthroplasty affects the HJC placement in the implanted patients, affecting not only the moments developed but also the muscular behaviour (Delp et al., 1996). However, the prediction equations considered are based on non-implanted patients, which can lead to a HCF misallocation, and thus affect the hip contact force predictions.
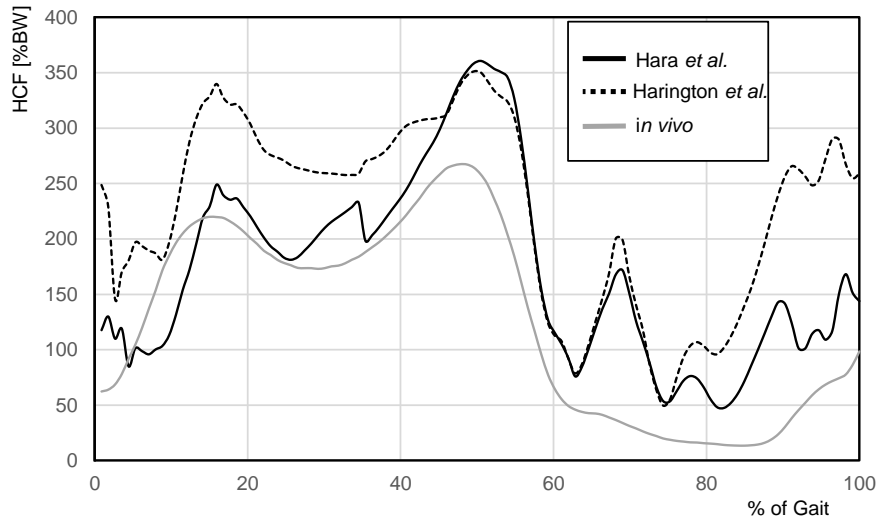
Figure 26: HCF prediction when using two different methods for estimate the HJC.
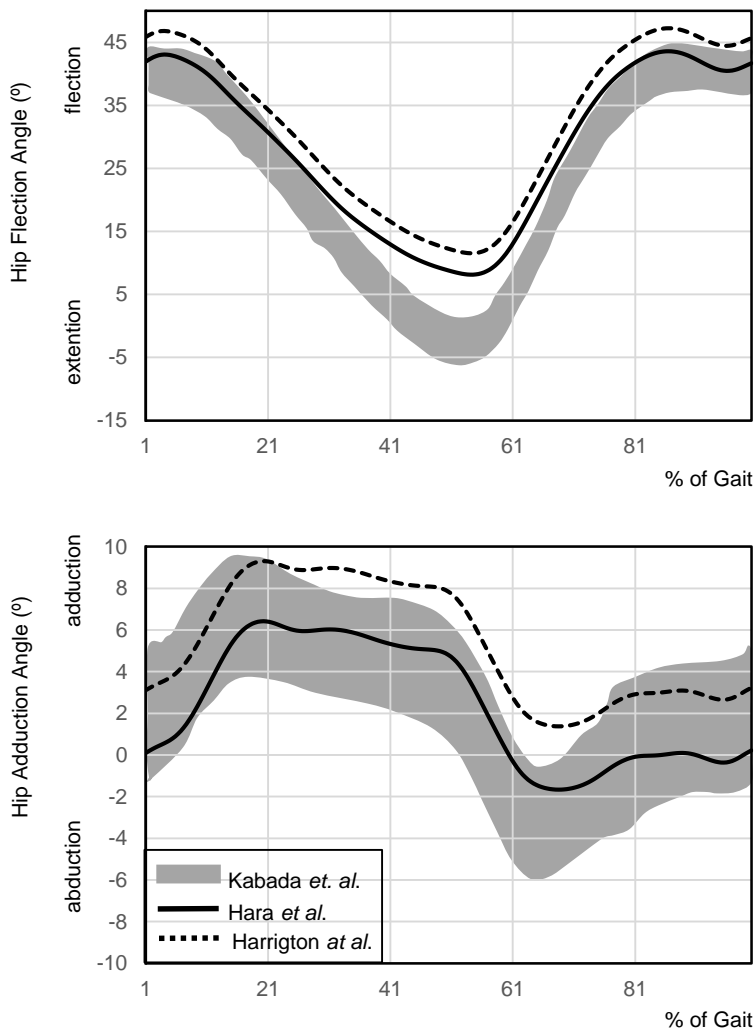
Figure 27: Hip joint angles obtained when using the two distinct HJC prediction methods. The shaded area corresponds to the joint angle ranges reported by Kadaba et al. (1990), for comparison.

6.3. Identification of the metabolic energy model

In the work of Praagman (2008), the weight factors are selected arbitrarily. This opens the possibility to the fact that a more informed choice of the weight factors may result in more accurate muscle and joint forces predictions. To explore this hypothesis, the influence of each cost function term is analysed by comparing the hip joint forces predicted by the model and those measured *in vivo* using instrumented prostheses. In other words, the aim is to quantify the relative contribution of the energy terms, one related with the detachment of cross-bridges and the other two connected to calcium-pumping, as proposed by Praagman (2008), to the prediction of the hip joint forces. The first approach to the problem is done by analysing the individual contribution of each term, by running simulations where the cost function used is composed by only one of the three cost function terms at a time. Next, a grid search is performed for multiple combinations of the weight factors, varied within a selected range. The last approach consists on a two-level optimization where the *inner optimization* consists on the muscle force-sharing problem formulation, described in Chapter 5, and the *outer optimization* consists in the identification of weight factors that lead to a closer match between the model and the *in vivo* HCF. A schematic visualization of the problem formulated is presented in Figure 28.
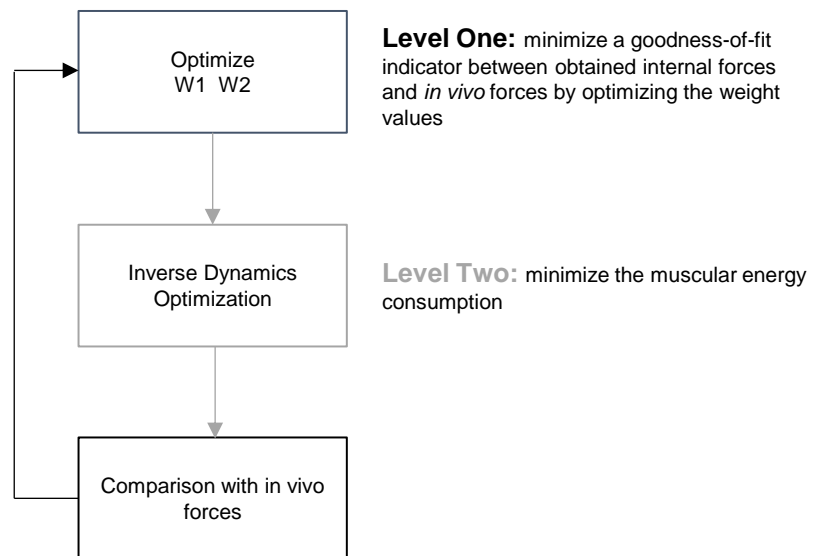
Figure 28: Cost function weight factors identification as a two-level optimization problem.

6.3.1. Weight factor's individual contribution

In order to draw some conclusions on the weight factors contribution, it is interesting to study the individual contribution of each term. Three simulations for each subject are carried by simulating each term of the objective function at a time, while the others have null contribution. The hip contact forces estimated by these simulations are presented in Figure 29. The results show that when considering only one of the linear terms, i.e. either the first or the second term of Equation (32), the force predictions are similar, presenting only minor deviations. The individual contribution of these terms seems therefore to

represent similar muscle recruitment criteria. The non-linear term leads to more unrealistic force predictions, which is especially highlighted by the over-estimation of the second peak of the HCF. Non-linear cost functions are believed to lead to muscle synergy, i.e. muscle load sharing (Praagman, 2008). Therefore, the increase in the numerical contact forces is related to a higher number of active muscles, producing a higher hip contact force. The three indicators considered for comparing the similarity in HCF between the numerical predictions and *in vivo* data for the performed simulations are detailed in Table 7.
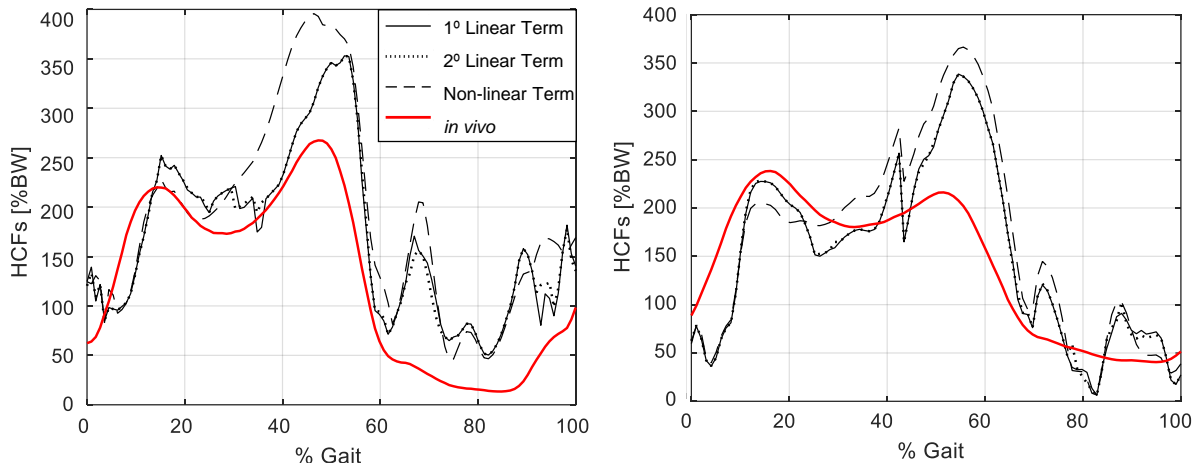
Figure 29: HCF considering individually each term of the energy-based cost function for (a) H2R patient and (b) H2R patient. The solid, dotted, and dashed lines represent the data obtained considering the first linear term, the second linear term and the non-linear term, respectively.

Table 7: Goodness-of-fit indicators for the HCF obtained for standard and individual contribution of each cost function term.

Subject	Term	RMSE [%BW]	RDP [%Exp.Peak]	FD [%BW]
H2R	First Linear Term	62,7	24,2	85,6
	Second Linear Term	63,4	24,3	86.0
	Non-linear Term	83,9	32,4	128,4
H1L	First Linear Term	58,1	29,6	107,4
	Second Linear Term	58,0	29,6	107.3
	Non-linear Term	73,5	35,0	134,3

6.3.2. Grid Search Identification

The initial approach to assess the relative contribution of the cost function terms is to perform a grid search, where simulations are run for different combinations of weight factors ω_1 and ω_2, varying within given ranges. The search range for each weight factor is selected so that the final contribution of the associated terms in the final objective function may differ up to four orders of magnitude. The objective is that the three energy terms are considered in the muscle recruitment criteria, even it with a lower contribution. The weight factors ω_1 and ω_2 are varied between 0.01 and 100, considering a logarithmically spaced vector of 50 values, resulting in a *50x50* grid, i.e. 2500 weight factors combinations. For each subject, the grid search results, i.e. the goodness-of-fit indicators chosen for evaluation (RMSE, RDEP and FD) for each weight factor combination are presented visually in Figure 30 using a colour-map where the dark blue means best fit. The best weight factors for each indicator, i.e. the combination of weight factors that presents the minimum value for each goodness-of-fit indicator is presented in Table 8.
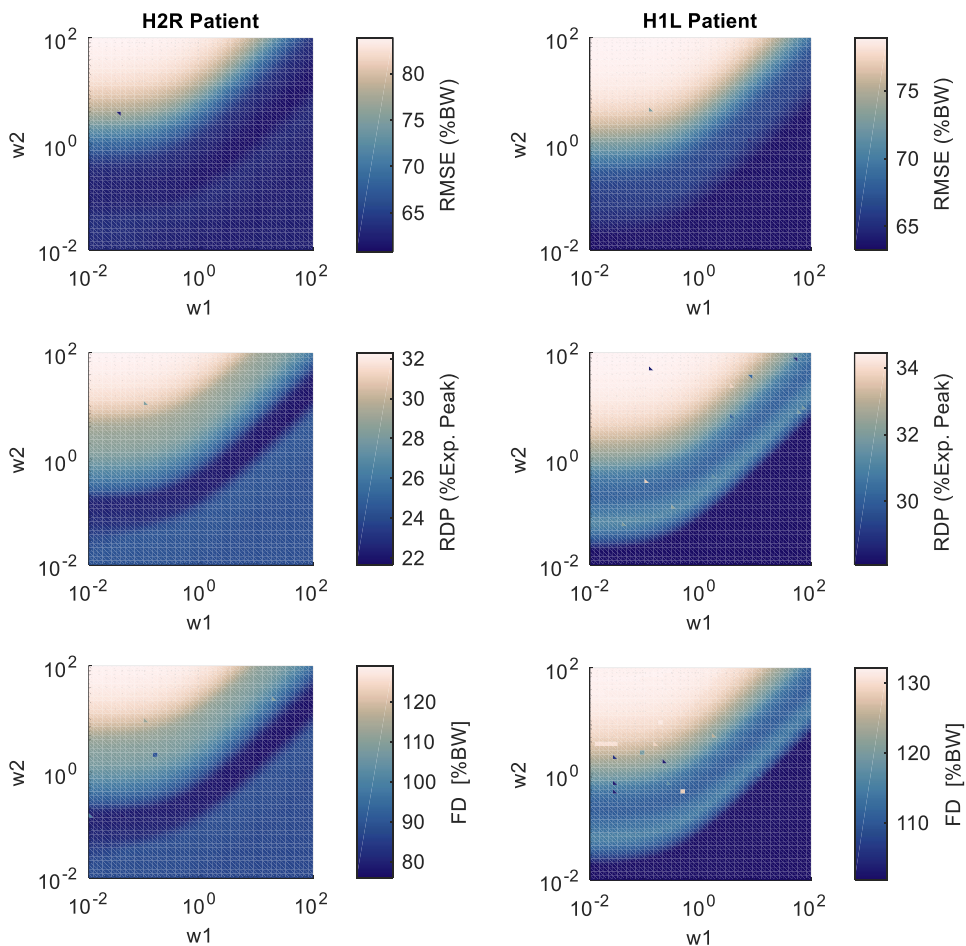
Figure 30: Grid search results for the three indicators of similarity between *in vivo* and numerical forces. The results for (a) patient H2R and (b) H1L. The colour map depicts the value of the indicator (RMSE, RDP and FD) in the respective weight factors combination, where dark blue means best fit.

Table 8: Grid search best results for both patients. The range of values for the three indicators of similarity for all grid search points is presented, as well as the combination of weight factors that lead to the best result, i.e. lower value, for the respective indicator.

Subject	RMSE range [%BW]	Min. RMSE		RDP range [%Exp.Peak]	Min. RDP		FD range [%BW]	Min. FD	
		w_1	w_2		w_1	w_2		w_1	w_2
H2R	61-84	100	12.65	22-32	100	12.65	75,9-129,0	100	15.26
HIL	63,3 - 78,9	39.07	0.03	28,1 - 34,4	100	0.07	101.8-132.1	100	1.93

The combinations of the weight factors associated with the best goodness-of-fit measurements differ from those originally recommended in the literature, resulting in improvements of the hip joint force predictions. However, no unique combination exists, i.e., different goodness-of-fit indicators may point towards different combinations, as observed for patient H1L. Moreover, note that for a given range of weight factors, differences between solutions are negligible, suggesting that many different weight factor combinations may lead to similar HCF predictions. Note that, in Figure 30, the dark blue area embraces multiple combinations of weight factors, for both patients. In fact, the HCF predictions obtained for the various weight factors combinations contained in the dark blue area, where similar.

To obtain a single solution considering all three indicators, the weight factors minimizing a combination of these three indicators may be sought. Table 9 presents the weight factors that minimize the sum of all three indicators normalized by their corresponding maximum. For comparison purposes, the standard solution is also presented.

Table 9: Goodness-of-fit indicators for the weight factors presenting the lowest sum of all three indicators, normalized by their maximum value, and the standard weight factors.

Subject		w_1	w_2	RMSE [%BW]	RDP [%Exp.Peak]	FD [%BW]
H2R	Lowest Sum	100	12.64	60,8	21,7	76,3
	Standard	0.33	0.66	63,3	25,9	94,7
	Relative Difference			3.9%	16.2%	19,4%
H1L	Lowest Sum	39,07	0.03	63,3	28,1	101,9
	Standard	0.33	0.66	68,8	30,5	112.8
	Relative Difference			8.0%	7.9%	9.7%

The results for both subjects seem to point towards the same direction. Overall, a small weight factor ω_2, lower than 20, and always smaller than ω_1, leads to more realistic force predictions. For the H2R patient, weight factors ω_2 smaller than 10 are not satisfactory as well. The worst results, e.g. maximum RMSE, have a lower contribution of ω_1 in relation to ω_2. Still, it is important to evaluate the results in relation to the ratio between the linear and non-linear terms of the cost function. The best force predictions have a lower relative contribution of the non-linear term of the cost function, i.e. <13% of the total energy contribution. The HCF prediction curves, illustrated in Figure 31, are under-estimated during initial stance and over-estimated during the late stance and swing phases for both patients. A high peak, much greater than *in vivo*, is observed at 50% of the gait cycle, i.e. at the end of the stance phase. Despite impacting the solution of the load sharing problem, the variation of the weight factors did not vary much the prediction of HCF, as highlighted in Figure 31. Note that the grey shadowed region represents the variation in HCF resulting from the application of the different weight factors considered. In any case, the optimization of the weight factors still leads to better force predictions.
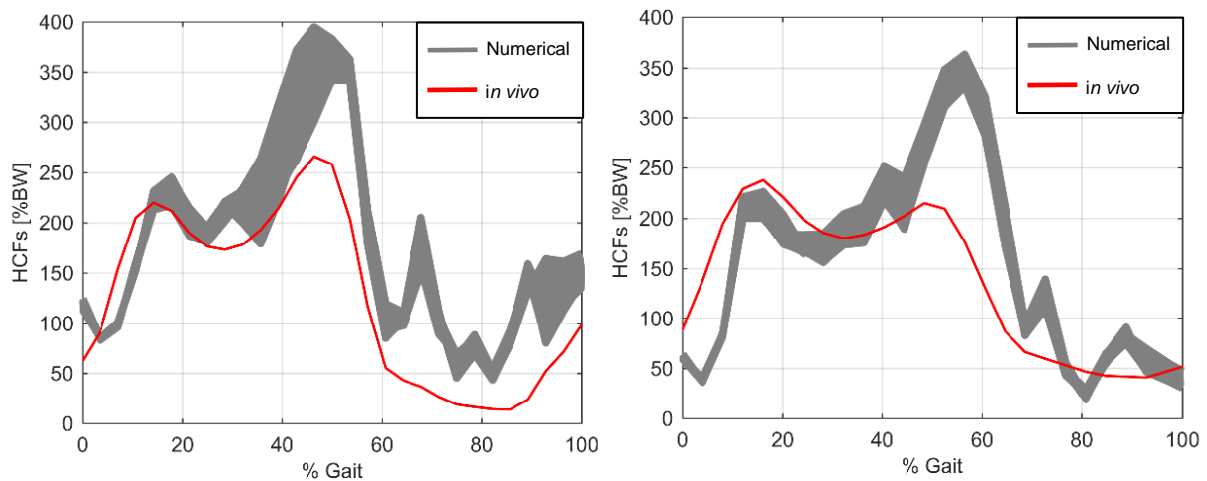
Figure 31: HCF for the (a) patient H2R and (b) patient H1L. The shaded grey area represents the range of the HCF predictions for all grid search simulations.

6.3.3. Two Level Optimization

When performing a grid search analysis, the parameters are evaluated only on discrete intervals and not on their entire domain. Therefore, a third approach is performed for a more detailed identification of the weight factors. The optimization of the weight factors is done using the *patternsearch* algorithm available in *MATLAB*. The algorithm consists on a numerical optimization method that does not use gradients for finding local minima. The objective of the optimization is only the minimization of the RMSE. The search was performed in the range of [0.01 100], as in Section 6.3.2, by creating upper and lower bound constraints. Due to possible existence of local minima, the pattern search is run 10 times, starting from different initial conditions, i.e. different initial weight values, chosen arbitrarily.

For the H2R patient, the 10 simulations converge to close combinations of the weights factors, presenting only slight variations, but the RMSE value is identical, within the given tolerance. The

simulations carried for the H2R converged to different local minima, presenting slight different values of RMSE for the HCF predicted. Table 10 presents the minimum found for the 10 simulations. The values obtained for each *patternsearch* iteration can be found on Appendix B.

Table 10:Optimal weight factors and respective RMSE. The results for the standard weight factors are also presented for comparison.

Subject		W_1	W_2	RMSE [%BW]
H2R	Standard	0,33	0,66	63,3
	Optimal Weight Factors	87,40	11,09	60,8
	Relative Deviation			*3,9%*
H1L	Standard	0,33	0,66	68,8
	Optimal Weight Factors	47,7	0,04	63,3
	Relative Deviation			*8,0%*

6.3.4. Discussion of the Results

The identification of the optimal objective weights is not straightforward. The goodness-of-fit indicators point towards different solutions, even though all of them resulted in improvements in relation to the standard weight factors. For some different combinations of weight factors, differences between HCF predictions are negligible. The cost function weights considerer in the muscle load force sharing problem have a low influence on HCF.

Nonetheless, a clear conclusion can be drawn: for both subjects, the error associated with the HCF predicted increased when increasing the non-linear term (ω_2). Similar results were obtained by Nikooyan et al. (2013), even though the authors study the influence of the weight factors on the *glenohumeral* joint contact forces. Still, it is interesting to notice that the predicted contact forces for the upper limb are underestimated, while, in the present work, the lower limb contact forces were overestimated. Pragmaan (2008) reports that introducing a non-linear term in the cost function should lead to more physiologically realistic results since only-linear cost functions predict sequential muscle recruitment instead of force sharing. In other words, the non-linear term leads to synergy (Crowninshield and Brand, 1981). In the present work, the non-linear term does lead to muscle synergy: for higher contributions of ω_2, the number of active muscles for each stride phase increased, discussed further in Section 6.4. When analysing the individual contribution of each term, as presented in Table 7 and Figure 29, the application of only the non-linear term led to an increased overestimation of the HCF. The force peak increased, on average, 8% under this condition. The reason behind this phenomenon is that the muscle-imposed synergy is causing more muscles to be active, increasing the total muscle force. Although muscle load

sharing is physiologically relevant and is recommended to be included in the muscle recruitment criteria, its contribution for the estimation of HCF was therefore not positive in this study.

When evaluating the relative contribution of the linear terms, it is challenging to draw clear conclusions. When the individual influence of the linear terms is evaluated, as presented in Section 6.3.1, the solutions, i.e. HCF, obtained for the first and second terms are similar, which suggests that the two terms might be solving the muscle force-sharing problem in an analogous way. *In vitro* studies report that 25% to 40% of the total energy consumption is related with the reabsorption of calcium (de Haan et al., 1986; Lou et al., 1997). Accordingly, for a more realistic function, future studies may consider this percentage in the definition of ω_1. However, one of the linear terms may possibly be disregarded without compromising the HCF predictions.

6.4. Evaluation of the muscles behavior

The individual muscle activations and total muscular are also an interesting object of study. Being the muscle activation patterns typical for gait motion, several studies have been dedicated to studying the typical muscle activity (Bonnefoy-Mazure and Armand, 2015; Ivanenko et al., 2004). The gait motion is achieved by the combined action of several muscles, each one with a specific role. Table 11 summarizes the overall muscle role and period of activity for the lower limb muscles most relevant for gait motion.

The muscle activations and total force are presented in Figure 32 for the H1L patient for the standard weight factors and also for the weight factors identified in Section 6.3.3. The muscle activations are also compared with literature.

When considering the new identified weight factors, i.e. ω_1=47.7 and ω_2=0.04, some muscle activations are in agreement with the literature, e.g. *Rectus Femoris*, *Soleus*, *Tibialis Anterior*, i.e., the activation period corresponds to the time during which these muscles are expected to be activated. However, some peak irregularities on the activations were encountered. Other muscles present an active state in periods where their physiological contribution is not expected, e.g. *Gluteus maximus*. In some other cases, the muscles are not activated during a period in which they have individual importance, e.g. *Tibialis Posterior*. The same is observed for the standard parameters.

The activations obtained for the standard parameters are comparable to those obtained by literature (Modenese et al., 2011; Modenese and Phillips, 2012) when using biomechanical models based on Horsman (2007) dataset and non-linear cost functions. However, the activations obtained for the new identified parameters, having low contributions of the non-linear term, are not comparable with literature once they present continuous maximum activation for a range of muscle.

Table 11: Principal muscles for gait motion, including their respective action and period of activity (Silva and Ambrósio, 2003; Sheffer and Chao, 2015)

Muscle Name	Muscle Action	Period of activity
Adductor longus	Adducts and flexes the thigh; helps to laterally rotate the hip joint.	Mid and terminal stance.
Bicepts Femoris LH	Flexes the knee and also rotates the tibia laterally, also extends the hip joint.	Heel stride and terminal swing.
Bicepts Femoris SH	Flexes the knee and also rotates the tibia laterally.	Heel stride and terminal swing.
Extensor Digitroum Longus	Extend toes 2–5 and dorsiflexes ankle.	Heel stride, pre-swing and swing.
Flexor Hallucis Longus	Flexes great toe, helps to supinate ankle, and is a very weak plantar flexor of ankle.	Mid and terminal stance
Gastrocnemius (lateral and medial head)	Powerful plantar flexor of ankle.	Mid and terminal stance.
Gluteus maximus	Major extensor of hip joint, helps to laterally rotate hip; superior fibres help to abduct hip, inferior fibres help to tighten iliotibial band.	Heel stride.
Gluteus medius	Major abductor of thigh, anterior fibres help to rotate hip medially, posterior fibres help to rotate hip laterally.	Heel stride and mid-stance.
Gracilis	Flexes the knee, adducts the thigh, and helps to medially rotate the tibia on the femur.	Initial swing.
Iliacus	Flex the torso and thigh with respect to each other.	Initial swing.
Peroneus longus	Everts foot and plantar flexes ankle, also helps to support the transverse arch of the foot.	Mid and terminal stance.
Rectus femoris	Extends the knee.	Heel stride, pre-swing and initial swing.
Sartorius	Flexes and laterally rotates the hip joint and flexes the knee.	Initial swing.
Soleus	Powerful plantar flexor of ankle.	Mid and terminal stance.
Tibialis anterior	Dorsiflexor of ankle and invertor of foot.	Heel stride and swing.
Tibialis posterior	Principal invertor of foot; also adducts foot, plantar flexes ankle, and helps to supinate the foot.	Mid and terminal stance.
Vaslus (intermedius, lateralis, medialis)	Extends the knee.	Heel stride and mid-stance.
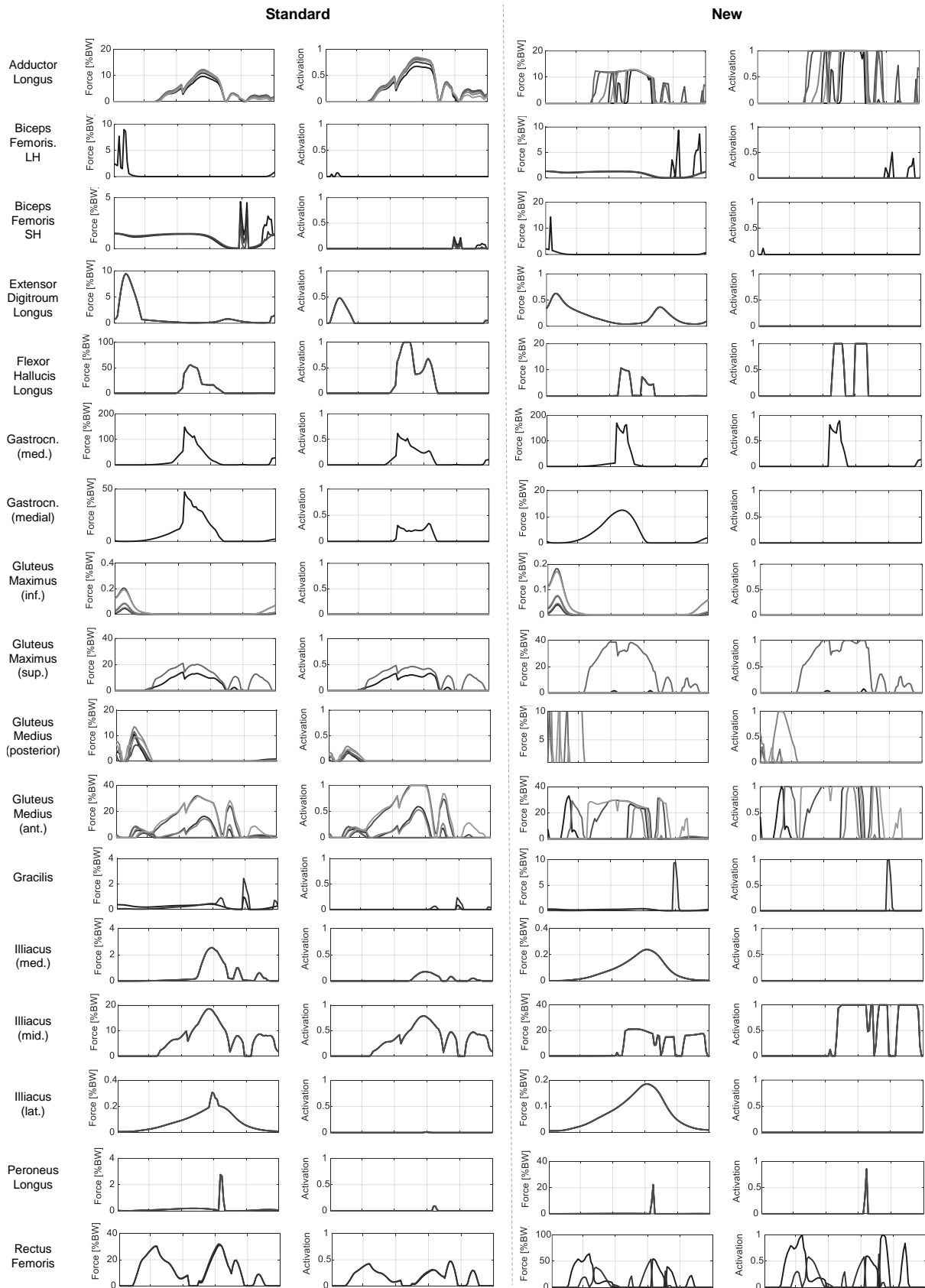
Figure 32: Activation patterns and total muscle forces for the muscles considered relevant during gait. The data were estimated for the H1L patient considering the (a) the standard parameters and (b) the new identified parameters. For some muscles, several lines are plotted because they represent the behaviour of the different muscle bundles into which the muscle is discretized.
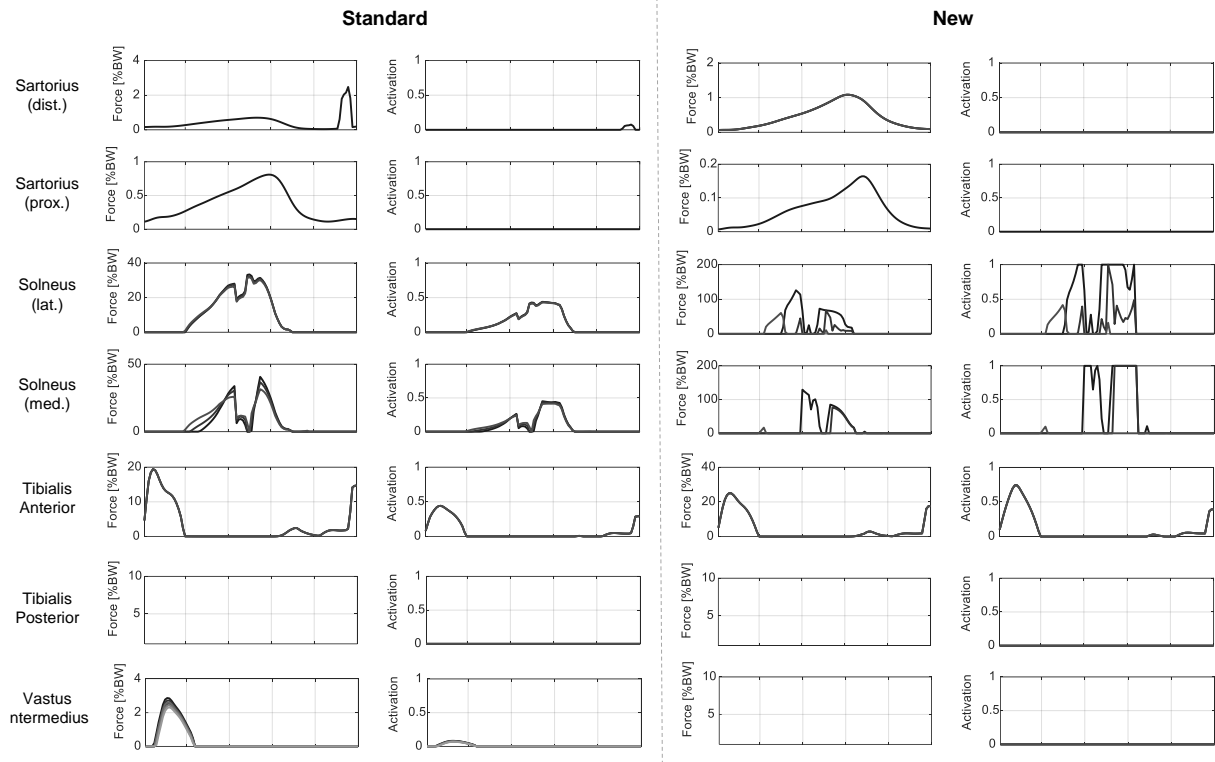
Figure 30: (cont.)

For the parameters identified in the two-level optimization, the muscles *Adductor Longus*, *Flexor hallucis longus*, *Flexor digitorum longus*, *Gluteus medius* (anterior), *Gluteus maximus* (superior), and *illiacus* (mid.) present continuous maximum activation that is not expected for typical gait motion (Simpson et al., 2015). Gait is a natural human movement that does not imply great physical effort. However, for the standard parameters, i.e. higher contribution on the non-linear term, only the muscle *Gluteus medius* presents maximum activation. In fact, the third term of the energy consumption function introduces muscle synergy, promoting load sharing between muscles, as well as antagonistic load. The lower contributions of the non-linear term cause sequential recruitment: the muscle with minimum cost tends to be activated, and the other muscles are only activated when the first reaches his maximum force. This causes the continuously maximum activations patterns observed in Figure 30 for example in *Adductor Longus* for the new identified parameters.

The parameters identified in last section, i.e. the parameters that minimize the error between numerical and experimental forces, lead to low muscle synergy. The muscle synergy is not advantageous for the proposes of this work and result in worst predictions of the HCF. Nevertheless, muscle synergism is important for a correct simulation of the muscle recruitment criteria and should be included. The human motion is achieved via co-activation of muscles, instead of activating each muscle independently (Zajac et al., 2002). The optimization result, i.e. optimal parameters having low contributions of the non-linear term, suggests that there are other aspects limiting the contribution of this term to the result. One

example is the incorrect modelling of some muscles, such as the *gluteus* muscles, that are introducing errors in the HCF prediction.

The *Gluteus* group force results are critical since they are maximally activated during mid and terminal stance, producing forces about *500N* in a stride period in which these muscles are reported not contribute to any specify gait task *in vivo* (Sheffler and Chae, 2015; Silva and Ambrósio, 2003). The same issue is reported in the literature (Modenese et al., 2011; Modenese and Phillips, 2012) when using biomechanical models based on Horsman (2007) dataset. Note that the *Gluteus* are muscles with large attachment areas, that are being included in the LLEM as several independent straight-line units with different origin and insertion points. Modelling these muscles as straight lines may lead to an underestimation of the muscle moment arms with respect to the HCJ, so that a higher force is needed to equilibrate the intersegmental moments, causing high activation levels. This aspect is further aggravated because these muscles are introducing unrealistic moments in the biomechanical systems that need to be compensated by other muscles, further contributing to over-estimated forces. The modelling of these muscles should be reviewed, and the inclusion of wrapping surfaces might be considered for a more accurate representation. In fact, Carbone et al. (2015) proposes a new comprehensive dataset for biomechanical modelling where wrapping surfaces were added to model the *Gluteus maximus* to ensure more realistic level arms. For the same musculoskeletal model, De Pieri et al. (2018) even proposes a different wrapping surface for each *Gluteus maximus* segment.

A series of studies used different criteria for solving the muscle load sharing problem: Crowninshield and Brand (1981) minimized the sum of muscle stress cubed, Heller et al. (2001) minimized the sum of muscle forces with upper bound constraints, Modenese et al. (2011) minimized a polynomial function of the muscle forces, where multiple powers were studied. The use of different criteria resulted in different activation patterns, especially when comparing linear to non-linear criteria (Pedersen et al., 1987). Nevertheless, all these methods, including the one presented in this work, could predict contact forces comparable with those measured *in vivo*. This observation is in agreement with the study of Stansfield et al. (2003), who stated that the criterion used for solving the muscle redundancy has an effect on muscle loading but a less obvious influence on joint contact forces.

7. Conclusions

The first objective of the present work is to validate the LLEM, a musculoskeletal model based on the comprehensive dataset published by Horsman (2007). The redundant muscle force sharing problem is solved using inverse dynamics. The muscle recruitment criteria is simulated by an energy related cost function proposed by Praagman et al. (2006). The main objective of the present work is to evaluate the relative contribution of the muscular energy consuming processes included in muscle load sharing cost function. The aim is to estimate the relative contribution of the processes included in the cost function, i.e. ion pumping and cross-bridges cycling, that can lead to a closer match between hip forces predicted by the model obtained forces and the experimental measurements. For that, the inverse dynamic simulation is repeated for a variety of different combinations of weight factors and the model-simulated HCF are compared to those measured *in vivo.* Also, new parameters are identified using a two-level optimization approach, where the objective is to find the combination of weight factors that lead to a lower RMSE. Also, the muscle activations patterns and the forces developed are evaluated to assess the accuracy of the biomechanical model and to identify upgrades that can be implemented to obtain more accurate predictions of hip contact forces.

A three-dimensional biomechanical model based on the comprehensive dataset published by Horsman (2007) is presented with the objective of studying the internal musculoskeletal loading for a gait cycle. The kinematic and kinetic data provided by *OrthoLoad* (Bergmann, 2008) for two patients is properly treated and used as input for inverse dynamic analyses. A kinematic analysis is successfully performed, and kinematic consistency was ensured. The driving angles prescribed for the simulation are comparable with those published in the literature (Arnold and Delp, 2011; Kadaba et al., 1990).

The energy related cost function proposed by Praagman (2008) is used to solve the redundant muscle force sharing problem for the lower limb. The authors validated the performance of the cost function under isometric conditions for an upper limb model. Nonetheless, the proposed cost function has also been shown to provide good estimations of the muscle energy rate for lower limb models (Ravera et al., 2019). The relative contribution of the energy-related terms included in the energy-based criterion proposed by Praagman (2008) are evaluated by comparing the obtained HCF with *in vivo* measurements. The musculoskeletal model of the lower extremity presented in this work is shown to allow the prediction of hip contact forces that compare well, both magnitude and pattern, to those measured *in vivo*, for different weight parameters.

The individual contribution of the two linear terms of the cost function, one related with the detachment of cross bridges and another with calcium pumping, lead to similar HCF predictions. This suggests that the solution for minimum energy consumption might the similar for the two energy terms, and one of the linear terms may possibly be disregarded without compromising the HCF predictions.

The model overestimates the HCF for late stance and swing phase, especially for the second peak of the HCF. For higher contributions of the non-linear term of the cost function, the synergism between muscles increases, and so does the magnitude of the calculated hip contact forces. This phenomenon

can be explained by the activation of a larger number of muscle actuators. Therefore, for the context of this work (i.e. predict the joint contact forces as close as possible to *in vivo*), the non-linear term high contribution is not advantageous since the forces are more over-estimated, increasing the error. Nevertheless, the muscle synergism is important for a correct simulation of the muscle recruitment criteria and should be included.

A set of new weight factors is identified for each subject, based on a two-level optimization approach. This newly identified parameters result in improvements in the model numerical HCF, but the new weight factors differ for the two subjects. Considering that local minima exist in the problem formulated, further investigation is necessary to find if a common set of parameters is possible to be defined for different subjects.

The force over-estimation may be related with the inappropriate description of some muscles. More precisely, the *gluteus* muscle group presents activation patterns that do not compare well with literature. These muscles, and others, present unrealistic activations, generating unrealistic moments on the biomechanical model that must be counteracted by other muscles, which further worsens the overestimation of the force. The modelling of these muscle should be reviewed, and the use of additional wrapping surfaces might have to be considered. Note that the present model only presents wrapping surfaces for two muscles: *gastrocnemius* and *iliopsoas*. Recently, Carbone et al. (2015) proposed a lower limb model including wrapping surfaces for eight muscles (including the *gluteus maximums*), and, based on this model, De Pieri et al. (2018) proposed more wrapping surfaces for another three muscles.

A series of studies used different criteria for solving the muscle load sharing problem. The use of different criteria resulted in different activation patterns, especially when comparing linear to non-linear criteria (Pedersen et al., 1987). Nonetheless, differences in predicted contact forces are limited, which is in agreement with the study of Stansfield et al. (2003), who stated that the criterion considered in the muscle load sharing problem has an effect on muscle loading but a less obvious influence on joint contact forces. This suggest that optimize/identify the relative contribution of the energy terms based on the reproduction of joint contact forces may not be the best approach. The optimization should also include muscle information.

7.1. Future work

Even if the lower limb model, together with the optimization techniques proposed, provide new opportunities for musculoskeletal estimations, this study still presents several limitations. For example, future work should include a larger number of subjects to allow a generalization the results.

When simulating the motion of the biomechanical model, the measured driving angles for the subjects performing a gait cycle was directly prescribed. However, a scaling procedure to adapt the model to the individual patient anatomy should be considered. A number of linear and non-linear scaling procedures have been proposed in the literature (Correa and Pandy, 2011; Lund et al., 2015; Nolte et al., 2016) to enable subject-specific simulations and increase the accuracy of the biomechanical model.

The present work showed that the HJC prediction has a considerable impact on HCF prediction. Two studied predictive methods positioned the HJC in dissimilar distances, which lead to considerable differences in the numerical HCF. Previous studies have also shown that changes in hip joint geometry and location have a high influence on the HCF predictions of the biomechanical system (Lenaerts et al., 2008). Therefore, further investigation on how to accurately track the HJC is fundamental.

The predicted contact forces present some peak irregularities that do not occur *in vivo*, but that are also found in other computational studies in the literature (Fraysse et al., 2009; Heller et al., 2001; Modenese et al., 2011; Moissenet et al., 2014; Rane et al., 2019; Stansfield et al., 2003). Although different simulations were performed to gain insight into the possible origin of these irregularities, no clear conclusions could be drawn. Consequently, further analyses are required.

In the present work, the two-level optimization approach was done using a pattern search algorithm. This procedure was chosen because optimization methods using gradients involve a high computational time if the gradients are not provided. However, future work should focus on using different optimization methods, such as genetic algorithms, for a more general search of the global optima.

Even though the non-linear term leads to synergy, the accuracy of the muscular agonist/antagonistic activity is not guaranteed. The *in vivo* coordination of the agonist and antagonist muscles is still an ongoing field on research (Lundberg et al., 2016; Yoo et al., 2016). Hurwitz et al. (2003) showed that the level of agonistic/antagonistic muscle activity affects the HCF prediction on biomechanical models. The muscle synergy predicted by the model did not lead to a correct HCF prediction since the numerical contact forces are mostly over-estimated. A possible limitation to correct synergy performance may be linked to incorrect representation of some of the muscles. Future studies should focus on including an accurate representation of the muscle synergy. For example, a constraint could be added in the muscle load sharing problem to ensure that the agonist/antagonism pairs must be active at the same time.

An analysis of the muscle moment arms developed in the biomechanical model should be performed to identify the critical muscles that are introducing inconsistent forces in the system (responsible for the over-estimation of the HCF). The geometry and modelling of the identified muscles should be modified to a better representation of the muscle apparatus, e.g. introduce wrapping surfaces.

Another important aspect is that there are other muscular energy-consuming processes that have not been accounted for in the cost function proposed by Praagman (2008). Some studies have shown that a percentage of the muscular energy consumption is related with sodium and potassium pumping (Barclay et al., 2007; Clausen, 2003). Therefore, a more accurate physiologically criterion should consider this process in the cost function (Nikooyan et al., 2013).

8. References

Alexander, R.M., 1997. A minimum energy cost hypothesis for human arm trajectories. Biol. Cybern. 76, 97–105.

Alt, H., Godau, M., 1995. Computing the Fréchet distance between two polygonal curves. Int. J. Comput. Geom. Appl. 5, 75–91.

Anderson, Frank C, Pandy, M.G., 2001. Dynamic Optimization of Human Walking . J. Biomech. Eng. 123, 381–390.

Anderson, Frank C., Pandy, M.G., 2001. Static and dynamic optimization solutions for gait are practically equivalent. J. Biomech. 34, 153–161.

Arnold, E.M., Delp, S.L., 2011. Fibre operating lengths of human lower limb muscles during walking. Philos. Trans. R. Soc. B Biol. Sci. 366, 1530–1539.

Arnold, E.M., Hamner, S.R., Seth, A., Millard, M., Delp, S.L., 2013. How muscle fiber lengths and velocities affect muscle force generation as humans walk and run at different speeds. J. Exp. Biol. 216, 2150–2160.

Arnold, E.M., Ward, S.R., Lieber, R.L., Delp, S.L., 2010. A model of the lower limb for analysis of human movement. Ann. Biomed. Eng. 38, 269–279.

Barclay, C.J., Woledge, R.C., Curtin, N.A., 2007. Energy turnover for Ca2+ cycling in skeletal muscle. J. Muscle Res. Cell Motil. 28, 259–274.

Bergmann, G., 2008. OrthoLoad [WWW Document]. Charité Univ. Berlin. URL orthoload.com (accessed 4.20.19).

Bergmann, G., Bender, A., Dymke, J., Duda, G., Damm, P., 2016. Standardized Loads Acting in Hip Implants. PLoS One 11.

Blinks, J.R., Rüdel, R., Taylor, S.R., 1978. Calcium transients in isolated amphibian skeletal muscle fibres: detection with aequorin. J. Physiol. 277, 291–323.

Bonnefoy-Mazure, A., Armand, S., 2015. Normal gait, in: Orthopedic Management of Children with Cerebral Palsy. Nova Science Publishers, Inc., pp. 199–214.

Byrne, D., Mulhall, K., Baker, J., 2010. Anatomy & Biomechanics of the Hip. Open Sport. Med. J. 4.

Carbone, V., 2016. Subject specific lower extremity modeling personalization of MS models using medical imaging and functional measurements, Journal of Chemical Information and Modeling.

Carbone, V., Fluit, R., Pellikaan, P., van der Krogt, M.M., Janssen, D., Damsgaard, M., Vigneron, L., Feilkas, T., Koopman, H.F.J.M., Verdonschot, N., 2015. TLEM 2.0 - A comprehensive

musculoskeletal geometry dataset for subject-specific modeling of lower extremity. J. Biomech. 48, 734–741.

Chambers, H., Sutherland, D., 2002. A Practical Guide to Gait Analysis. J. Am. Acad. Orthop. Surg. 10, 222–231.

Chandler, R., Clauser, C., McConville, J., Reynolds, H., Young, J., 1975. Investigation of Inertial Properties of the Human Body. PN.

Clausen, T., 2003. Na and K Pump Regulation and Skeletal Muscle Contractility. Physiol. Rev. 1269–1324.

Collins, J.J., 1995. The redundant nature of locomotor optimization laws. J. Biomech. 28 3, 251–267.

Cooke, R., 2004. The sliding filament model: 1972-2004. J. Gen. Physiol. 123, 643–656.

Correa, T.A., Pandy, M.G., 2011. A mass–length scaling law for modeling muscle strength in the lower limb. J. Biomech. 44, 2782–2789.

Crowninshield, R.D., Brand, R.A., 1981. A physiologically based criterion of muscle force prediction in locomotion. J. Biomech. 14, 793–801.

de Haan, A., de Jong, J., van Doorn, J.E., Huijing, P.A., Woittiez, R.D., Westra, H.G., 1986. Muscle economy of isometric contractions as a function of stimulation time and relative muscle length. Pflügers Arch. 407, 445–450.

De Pieri, E., Lund, M.E., Gopalakrishnan, A., Rasmussen, K.P., Lunn, D.E., Ferguson, S.J., 2018. Refining muscle geometry and wrapping in the TLEM 2 model for improved hip contact force prediction. PLoS One 13, 1–19.

Delp, S., Loan, J.P., Gross, M., Zajac, F., Topp, E., Rosen, J., 1990. An interactive graphics-based model of the lower extremity to study orthopaedic surgical procedures. IEEE Trans. Biomed. Eng. 37, 757–767.

Delp, S.L., Wixson, R.L., Komattu, A. V, Kocmond, J.H., 1996. How superior placement of the joint center in hip arthroplasty affects the abductor muscles. Clin. Orthop. Relat. Res. 328, 137–146.

Dicarlo, S., Sipe, E., Layshock, J., Varyani, S., 1999. Experiment demonstrating skeletal muscle biomechanics. Am. J. Physiol. 275, S59-71.

Dumas, R., Chèze, L., Verriest, J.P., 2007. Adjustments to McConville et al. and Young et al. body segment inertial parameters. J. Biomech. 40, 543–553.

Fraysse, F., Dumas, R., Cheze, L., Wang, X., 2009. Comparison of global and joint-to-joint methods for estimating the hip joint load and the muscle forces during walking. J. Biomech. 42, 2357–2362.

Fregly, B.J., Besier, T.F., Lloyd, D.G., Delp, S.L., Banks, S.A., Pandy, M.G., D'Lima, D.D., 2012. Grand challenge competition to predict in vivo knee loads. J. Orthop. Res. 30, 503–513.

Gage, J.R., 1993. Gait analysis. An essential tool in the treatment of cerebral palsy. Clin. Orthop. Relat. Res. 288, 126–34.

Garner, B., Pandy, M., 2000. The Obstacle-Set Method for Representing Muscle Paths in Musculoskeletal Models. Comput. Methods Biomech. Biomed. Engin. 3, 1–30.

Hall, John E. ; Guyton, A.C., 2016. Guyton and Hall Textbook of Medical Physiology, 13th ed. Elsevier.

Hara, R., McGinley, J., Briggs, C., Baker, R., Sangeux, M., 2016. Predicting the location of the hip joint centres, impact of age group and sex. Sci. Rep. 6, 1–9.

Harrington, M.E., Zavatsky, A.B., Lawson, S.E.M., Yuan, Z., Theologis, T.N., 2007. Prediction of the hip joint centre in adults, children, and patients with cerebral palsy based on magnetic resonance imaging. J. Biomech. 40, 595–602.

Haug, E.J., Yen, J., 1992. Implicit Numerical Integration of Constrained Equations of Motion Via Generalized Coordinate Partitioning. J. Mech. Des. 114, 296–304.

Heller, M.O., Bergmann, G., Deuretzbacher, G., Dürselen, L., Pohl, M., Claes, L., Haas, N.P., Duda, G.N., 2001. Musculo-skeletal loading conditions at the hip during walking and stair climbing. J. Biomech. 34, 883–893.

Horsman, M.D.K., 2007. The Twente Lower Extremity Model Human Locomotor Apparatus. University of Twente, PhD Thesis.

Hurwitz, D.E., Foucher, K.C., Andriacchi, T.P., 2003. A new parametric approach for modeling hip forces during gait. J. Biomech. 36, 113–119.

Ivanenko, Y.P., Poppele, R.E., Lacquaniti, F., 2004. Five basic muscle activation patterns account for muscle activity during human locomotion. J. Physiol. 556, 267–282.

Kadaba, M.P., Ramakrishnan, H.K., Wootten, M.E., 1990. Measurement of lower extremity kinematics during level walking. J. Orthop. Res. 8, 383–392.

Kaplan, M.L., 2000. Efficient Optimal Control of Large-Scale Biomechanical Systems. Standford Univertisy, PhD Thesis.

Lenaerts, G., De Groote, F., Demeulenaere, B., Mulier, M., Van der Perre, G., Spaepen, A., Jonkers, I., 2008. Subject-specific hip geometry affects predicted hip joint contact forces during gait. J. Biomech. 41, 1243–1252.

Lou, F., Curtin, N., Woledge, R., 1997. The energetic cost of activation of white muscle fibres from the dogfish Scyliorhinus canicula. J. Exp. Biol. 200, 495–501.

Lund, M.E., Andersen, M.S., de Zee, M., Rasmussen, J., 2015. Scaling of musculoskeletal models from static and dynamic trials. Int. Biomech. 2, 1–11.

Lundberg, H.J., Rojas, I.L., Foucher, K.C., Wimmer, M.A., 2016. Comparison of Antagonist Muscle

Activity During Walking Between Total Knee Replacement and Control Subjects Using Unnormalized Electromyography. J. Arthroplasty 31, 1331–1339.

Mansfield, P.J., Neumann, D.A., 2019. Structure and Function of the Ankle and Foot. Essentials Kinesiol. Phys. Ther. Assist. 311–350.

Modenese, L., Phillips, A.T.M., 2012. Prediction of hip contact forces and muscle activations during walking at different speeds. Multibody Syst. Dyn. 28, 157–168.

Modenese, L., Phillips, A.T.M., Bull, A.M.J., 2011. An open source lower limb model: Hip joint validation. J. Biomech. 44 12, 2185–2193.

Moissenet, F., Chèze, L., Dumas, R., 2014. A 3D lower limb musculoskeletal model for simultaneous estimation of musculo-tendon, joint contact, ligament and bone forces during gait. J. Biomech. 47, 50–58.

Nikooyan, A.A., 2011. Forces in the Shoulder Joint. On validation of musculoskeletal shoulder muscles. Delft University of Technology, PhD Thesis.

Nikooyan, A.A., Veeger, H., Westerhoff, P., Bergmann, G., Van Der Helm, F.C.T., 2013. Relative contribution of different muscle energy consumption processes in an energy-based muscle load sharing cost function. J. Mech. Med. Biol. 13, 1–18.

Nikravesh, P.E., 1988. Computer-aided Analysis of Mechanical Systems. Prentice-Hall, Inc., Upper Saddle River, NJ, USA.

Nolte, D., Tsang, C.K., Zhang, K.Y., Ding, Z., Kedgley, A.E., Bull, A.M.J., 2016. Non-linear scaling of a musculoskeletal model of the lower limb using statistical shape models. J. Biomech. 49, 3576–3581.

Pedersen, D R, Brand, R.A., Cheng, C., Arora, J.S., 1987. Direct Comparison of Muscle Force Predictions Using Linear and Nonlinear Programming. J. Biomech. Eng. 109, 192–199.

Pedersen, D. R., Brand, R.A., Cheng, C., Arora, J.S., 1987. Direct comparison of muscle force predictions using linear and nonlinear programming. J. Biomech. Eng. 109, 192–199.

Perry, J., Burnfield, J.M. (Eds.), 2010. Gait Analysis: Normal and Pathological Function. J. Sports Sci. Med. 9, 353.

Pfister, A., West, A.M., Bronner, S., Noah, J.A., 2014. Comparative abilities of Microsoft Kinect and Vicon 3D motion capture for gait analysis. J. Med. Eng. Technol. 38, 274–280.

Piazza, S., Okita, N., Cavanagh, P., 2001. Accuracy of the functional method of hip joint center location: Effects of limited motion and varied implementation. J. Biomech. 34, 967–973.

Praagman, M., 2008. Muscle load sharing. An energy-based approach. Vrije Universiteit, PhD Thesis.

Quental, C., 2013. Biomechanical Tools for the Analysis of the Native and Prosthetic Shoulders. PhD

Thesis, Instituto Superior Técnico, Universidade de Lisboa.

Quental, C., Azevedo, M., Ambrósio, J., S.B., G., Folgado, J., 2018. Influence of the Musculotendon Dynamics on the Muscle Force-Sharing Problem of the Shoulder-A Fully Inverse Dynamics Approach. J. Biomech. Eng. 140.

Quental, C., Folgado, J., Ambrósio, J., Monteiro, J., 2015. Critical analysis of musculoskeletal modelling complexity in multibody biomechanical models of the upper limb. Comput. Methods Biomech. Biomed. Engin. 18, 749–759.

Quental, C., Folgado, J.O.M.G., Ambrósio, J., 2016. A window moving inverse dynamics optimization for biomechanics of motion. Multibody Syst. Dyn. 38, 157–171.

Rane, L., Ding, Z., McGregor, A.H., Bull, A.M.J., 2019. Deep Learning for Musculoskeletal Force Prediction. Ann. Biomed. Eng. 47, 778–789.

Rasmussen, J., Damsgaard, M., Voigt, M., 2001. Muscle recruitment by the min/max criterion - A comparative numerical study. J. Biomech. 34, 409–415.

Ravera, E.P., Crespo, M.J., Catalfamo Formento, P.A., 2019. Assessment of the energy-related cost function over a range of walking speeds. Biomech. Model. Mechanobiol.

Sheffler, L.R., Chae, J., 2015. Hemiparetic Gait. Phys. Med. Rehabil. Clin. N. Am. 26, 611–623.

Silva, M.P.T., Ambrósio, J.A.C., 2003. Solution of Redundant Muscle Forces in Human Locomotion with Multibody Dynamics and Optimization Tools. Mech. Based Des. Struct. Mach. 31, 381–411.

Silva, M.P.T., Ambrósio, J.A.C., 2002. Kinematic data consistency in the inverse dynamic analysis of biomechanical systems. Multibody Syst. Dyn. 8, 219–239.

Simpson, C.S., Sohn, M.H., Allen, J.L., Ting, L.H., 2015. Feasible muscle activation ranges based on inverse dynamics analyses of human walking. J. Biomech. 48, 2990–2997.

Stansfield, B.W., Nicol, A.C., Paul, J.P., Kelly, I.G., Graichen, F., Bergmann, G., 2003. Direct comparison of calculated hip joint contact forces with those measured using instrumented implants. An evaluation of a three-dimensional mathematical model of the lower limb. J. Biomech. 36, 929–936.

Sutherland, D., 1997. The development of mature gait. Gait Posture 6, 163–170.

Tsirakos, D., Baltzopoulos, V., Bartlett, R., 2017. Review of Inverse Optimization for Functional and Physiological Considerations Related to the Force-Sharing Problem. Crit. Rev. Biomed. Eng. 45, 511–547.

van der Helm, F., Veeger, D., Pronk, G.M., Woude, L., Rozendal, R.H., 1992. Geometry parameters for musculoskeletal modelling of the shoulder system. J. Biomech. 25, 129–144.

Winter, D.A., 2009. Biomechanics and Motor Control of Human Movement: Fourth Edition, Biomechanics and Motor Control of Human Movement: Fourth Edition.

Wren, T.A.L., Gorton, G.E., Õunpuu, S., Tucker, C.A., 2011. Efficacy of clinical gait analysis: A systematic review. Gait Posture 34, 149–153.

Wu, G., Siegler, S., Allard, P., Kirtley, C., Leardini, A., Rosenbaum, D., Whittle, M., D'Lima, D., Cristofolini, L., Witte, H., Schmid, O.A., Stokes, I., 2002. ISB recommendation on definitions of joint coordinate system of various joints for the reporting of human joint motion--part I: ankle, hip, and spine. International Society of Biomechanics. J. Biomech. 35, 543–548.

Yamaguchi, G.T., 2001. Dynamic Modeling of Musculoskeletal Motion. Springer Science & Business Media.

Yamaguchi, G.T., Moran, D.W., Si, J., 1995. A computationally efficient method for solving the redundant problem in biomechanics. J. Biomech. 28, 999–1005.

Yoo, H.-J., Sim, T., Choi, A., Park, H.-J., Yang, H., Heo, H.M., Park, K.S., Mun, J.H., 2016. Quantifying coordination between agonist and antagonist muscles during a gait. J. Mech. Sci. Technol. 30, 5321–5328.

Zajac, F.E., 1989. Muscle and tendon: properties, models, scaling, and application to biomechanics and motor control. Crit. Rev. Biomed. Eng. 17, 359—411.

Zajac, F.E., Neptune, R.R., Kautz, S.A., 2002. Biomechanics and muscle coordination of human walking: Part I: Introduction to concepts, power transfer, dynamics and simulations. Gait Posture 16, 215–232.

Appendix A: **Muscle Apparatus**

The following Tables A1 to A38 present the Lower Extremity Muscle Apparatus included in the LLEM. The physiological parameters presented are: the physiological cross-section area *PSCA*, defined as the muscle volume divided by the optimal fibre length, the optimal muscle length L_0, the tendon length L_s and the pennation angle *α*, defined as the angle between a fascicle's orientation and the tendon axis. The geometric parameters comprise the origin and insertion of the muscle in the respective rigid bodies local reference frame *(ξ,η,ζ)*. The parameters presented are needed for modelling the muscle as a mechanical element. The representative images of each muscle are from the University of Washington "Musculoskeletal Atlas: A Musculoskeletal Atlas of the Human Body" by Carol Teitz, M.D. and Dan Graney, Ph.D. The images are reproduced with the permission of the authors.

Table A1: Adductor Brevis physiological parameters.
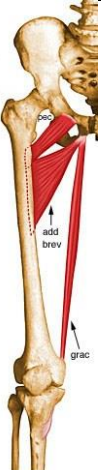
Adductor Brevis	Bundle	PCSA (cm^2)	L_0 (m)	L_S (m)	α (rad)	Origin Insertion	ξ (m)	η (m)	ζ (m)
	Prox.1	1.900	0.0950	0.0340	0.0000	Pelvis	0.0967	-0.0617	0.0213
						Femur	-0.0025	0.0936	0.0140
	Prox.2	1.900	0.0950	0.0418	0.0000	Pelvis	0.1012	-0.0619	0.0193
						Femur	0.0011	0.0811	0.0131
	Mid.1	1.750	0.1040	0.0369	0.0000	Pelvis	0.0962	-0.0669	0.0144
						Femur	0.0030	0.0685	0.0125
	Mid.2	1.750	0.1040	0.0467	0.0000	Pelvis	0.0998	-0.0671	0.0127
						Femur	0.0039	0.0555	0.0119
	Dist.1	1.600	0.1120	0.0409	0.0000	Pelvis	0.0891	-0.0744	0.0071
						Femur	0.0046	0.0426	0.0107
	Dist.2	1.600	0.1120	0.0493	0.0000	Pelvis	0.0914	-0.0745	0.0060
						Femur	0.0061	0.0298	0.0084

Table A2: Adductor Longus physiological parameters.

Adductor Longus	Bundle	PCSA (cm^2)	L_0 (m)	L_S (m)	α (rad)	Origin Insertion	ξ (m)	η (m)	ζ (m)
	1	2.517	0.1060	0.0768	0.0000	Pelvis	0.1030	-0.0579	0.0241
						Femur	0.0148	-0.0011	0.0009
	2	2.517	0.1060	0.0860	0.0000	Pelvis	0.1049	-0.0603	0.0216
						Femur	0.0152	-0.0133	-0.0015
	3	2.517	0.1060	0.0959	0.0000	Pelvis	0.1062	-0.0624	0.0186
						Femur	0.0161	-0.0258	-0.0032
	4	2.517	0.1060	0.1060	0.0000	Pelvis	0.1068	-0.0643	0.0154
						Femur	0.0171	-0.0384	-0.0047
	5	2.517	0.1060	0.1162	0.0000	Pelvis	0.1066	-0.0660	0.0120
						Femur	0.0178	-0.0509	-0.0065
	6	2.517	0.1060	0.1262	0.0000	Pelvis	0.1055	-0.0675	0.0085
						Femur	0.0177	-0.0632	-0.0090

Table A3: Adductor Magnus physiological parameters.

Adductor Magnus	Bundle	PCSA (cm²)	L_0 (m)	L_S (m)	α (rad)	Origin Insertion	ξ (m)	η (m)	ζ (m)
	Dist.1	8.833	0.1080	0.2103	0.0000	Pelvis	0.0295	-0.1197	0.0420
						Femur	0.0074	-0.1923	-0.0486
	Dist.2	8.833	0.1080	0.2148	0.0000	Pelvis	0.0354	-0.1158	0.0348
						Femur	0.0074	-0.1923	-0.0486
	Dist.3	8.833	0.1080	0.2261	0.0000	Pelvis	0.0526	-0.1065	0.0202
						Femur	0.0074	-0.1923	-0.0486
	Mid. 1	3.683	0.1040	0.0649	0.0000	Pelvis	0.0226	-0.1177	0.0411
						Femur	0.0129	-0.0259	-0.0017
	Mid. 2	3.683	0.1040	0.0646	0.0000	Pelvis	0.0255	-0.1155	0.0452
						Femur	0.0129	-0.0259	-0.0017
	Mid. 3	3.683	0.1040	0.0957	0.0000	Pelvis	0.0293	-0.1147	0.0352
						Femur	0.0142	-0.0575	-0.0083
	Mid. 4	3.683	0.1040	0.0958	0.0000	Pelvis	0.0318	-0.1129	0.0387
						Femur	0.0142	-0.0575	-0.0083
	Mid. 5	3.683	0.1040	0.1303	0.0000	Pelvis	0.0380	-0.1108	0.0281
						Femur	0.0164	-0.0893	-0.0114
	Mid. 6	3.683	0.1040	0.1306	0.0000	Pelvis	0.0399	-0.1094	0.0307
						Femur	0.0164	-0.0893	-0.0114
	Prox. 1	1.250	0.1070	0.0320	0.0000	Pelvis	0.0691	-0.0937	0.0131
						Femur	0.0097	0.0673	0.0040
	Prox. 2	1.250	0.1070	0.0281	0.0000	Pelvis	0.0544	-0.1020	0.0229
						Femur	0.0115	0.0466	0.0022
	Prox. 3	1.250	0.1070	0.0486	0.0000	Pelvis	0.0618	-0.0979	0.0180
						Femur	0.0134	0.0258	0.0004
	Prox. 4	1.250	0.1070	0.0706	0.0000	Pelvis	0.0691	-0.0937	0.0131
						Femur	0.0151	0.0051	-0.0013

Table A4: Biceps Femoris Long Head physiological parameters.

Biceps Femoris CL	Bundle	PCSA (cm²)	L_0 (m)	L_S (m)	α (rad)	Origin Insertion	ξ (m)	η (m)	ζ (m)
	1	27.200	0.0850	0.3362	0.5219	Pelvis	0.0127	-0.1096	0.0734
						Tibia	0.0305	0.1169	0.0485

Table A5: Biceps Femoris Short Head physiological parameters.

Bices Femoris CB	Bundle	PCSA (cm²)	L_0 (m)	L_S (m)	α (rad)	Origin Insertion	ξ (m)	η (m)	ζ (m)
	1	3.933	0.0910	0.1482	0.0000	Femur	0.0043	-0.0187	0.0067
						Tibia	0.0305	0.1169	0.0485
	2	3.933	0.0910	0.1042	0.0000	Femur	0.0073	-0.0646	-0.0011
						Tibia	0.0305	0.1169	0.0485
	3	3.933	0.0910	0.0565	0.0000	Femur	0.0098	-0.1136	-0.0010
						Tibia	0.0305	0.1169	0.0485

Table A6: Extensor Digitorum Longus physiological parameters.

Ext. dig.long	Bundle	PCSA (cm²)	L_0 (m)	L_S (m)	α (rad)	Origin Insertion	ξ (m)	η (m)	ζ (m)
	1	1.800	0.0600	0.4139	0.1449	Tibia	0.0225	0.0546	0.0391
						Toes	0.0274	-0.0067	0.0173
	2	1.800	0.0600	0.4522	0.1449	Tibia	0.0336	0.0940	0.0374
						Toes	0.0274	-0.0067	0.0173
	3	1.800	0.0600	0.4767	0.1449	Tibia	0.0435	0.1189	0.0351
						Toes	0.0274	-0.0067	0.0173

Table A7: Extensor Hallucis Longus physiological parameters.

Ext. hal.long.	Bundle	PCSA (cm²)	L_0 (m)	L_S (m)	α (rad)	Origin Insertion	ξ (m)	η (m)	ζ (m)
	1	2.033	0.0600	0.2549	0.2513	Tibia	0.0178	-0.0963	0.0286
						Toes	0.0183	0.0003	-0.0365
	2	2.033	0.0600	0.3068	0.2513	Tibia	0.0164	-0.0418	0.0318
						Toes	0.0183	0.0003	-0.0365
	3	2.033	0.0600	0.3602	0.2513	Tibia	0.0193	0.0132	0.0358
						Toes	0.0183	0.0003	-0.0365

Table A8: Flexor Digitorum Longus physiological parameters.

Flex. dig.long.	Bundle	PCSA (cm²)	L_0 (m)	L_S (m)	α (rad)	Origin Insertion	ξ (m)	η (m)	ζ (m)
	1	2.200	0.0380	0.4437	0.4974	Tibia	0.0114	0.0184	-0.0078
						Toes	0.0233	-0.0150	0.0137
	2	2.200	0.0380	0.3907	0.4974	Tibia	0.0125	-0.0348	-0.0122
						Toes	0.0233	-0.0150	0.0137
	3	2.200	0.0380	0.3498	0.4974	Tibia	0.0119	-0.0757	-0.0106
						Toes	0.0233	-0.0150	0.0137

Table A9: Flexor Hallucis Longus physiological parameters.

Flex. hal.long.	Bundle	PCSA (cm²)	L₀ (m)	Lₛ (m)	α (rad)	Origin Insertion	ξ (m)	η (m)	ζ (m)
	1	10.367	0.0260	0.4382	0.5253	Tibia	0.0085	-0.0167	0.0399
						Toes	0.0244	-0.0134	-0.0366
	2	10.367	0.0260	0.3847	0.5253	Tibia	0.0084	-0.0705	0.0347
						Toes	0.0244	-0.0134	-0.0366
	3	10.367	0.0260	0.3304	0.5253	Tibia	0.0085	-0.1256	0.0295
						Toes	0.0244	-0.0134	-0.0366

Table A10: Gastrocnemius physiological parameters.

Gastrocn	Bundle	PCSA (cm²)	L₀ (m)	Lₛ (m)	α (rad)	Origin Insertion	ξ (m)	η (m)	ζ (m)
	Lat.	24.000	0.0570	0.4438	0.4433	Femur	0.0072	-0.2049	0.0043
						Foot	-0.0935	-0.0304	0.0229
	Med	43.800	0.0600	0.4552	0.1885	Femur	0.0061	-0.1958	-0.0362
						Foot	-0.0938	-0.0388	0.0201

Table A11: Gemellus physiological parameters.
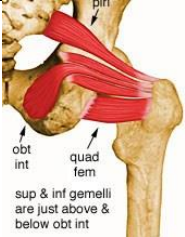
Gemellus	Bundle	PCSA (cm²)	L₀ (m)	Lₛ (m)	α (rad)	Origin Insertion	ξ (m)	η (m)	ζ (m)
	Inf.	4.100	0.0340	0.0774	0.0000	Pelvis	-0.0145	-0.0892	0.0619
						Femur	0.0082	0.1837	0.0391
	Sup.	4.100	0.0340	0.0734	0.0000	Pelvis	-0.0051	-0.0401	0.0403
						Femur	0.0146	0.1748	0.0293

Table A12: Gluteus Maximus physiological parameters.

Glut. Max.	Bundle	PCSA (cm^2)	L_0 (m)	L_S (m)	α (rad)	Origin Insertion	ξ (m)	η (m)	ζ (m)
	Sup.1	8.283	0.1200	0.0135	0.0000	Pelvis	-0.0285	0.0290	0.0748
						Femur	0.0221	0.2340	0.0694
	Sup. 2	8.283	0.1200	0.0370	0.0000	Pelvis	-0.0392	0.0064	0.0559
						Femur	0.0169	0.2039	0.0741
	Sup. 3	8.283	0.1200	0.0550	0.0000	Pelvis	-0.0459	-0.0214	0.0404
						Femur	0.0103	0.1740	0.0793
	Sup. 4	8.283	0.1200	0.0397	0.0000	Pelvis	-0.0407	0.0404	0.0637
						Femur	0.0375	0.2293	0.0645
	Sup. 5	8.283	0.1200	0.0644	0.0000	Pelvis	-0.0527	0.0190	0.0436
						Femur	0.0330	0.1989	0.0690
	Sup. 6	8.283	0.1200	0.0799	0.0000	Pelvis	-0.0588	-0.0093	0.0286
						Femur	0.0257	0.1692	0.0745
	Inf. 1	3.750	0.1510	0.0201	0.0000	Pelvis	-0.0569	-0.0570	0.0153
						Femur	-0.0240	0.1096	0.0507
	Inf. 2	3.750	0.1510	0.0145	0.0000	Pelvis	-0.0482	-0.0636	0.0174
						Femur	-0.0224	0.0960	0.0459
	Inf. 3	3.750	0.1510	0.0142	0.0000	Pelvis	-0.0400	-0.0743	0.0170
						Femur	-0.0146	0.0714	0.0371
	Inf. 4	3.750	0.1510	0.0150	0.0000	Pelvis	-0.0520	-0.0503	0.0219
						Femur	-0.0240	0.1096	0.0507
	Inf. 5	3.750	0.1510	0.0099	0.0000	Pelvis	-0.0433	-0.0569	0.0240
						Femur	-0.0224	0.0960	0.0459
	Inf. 6	3.750	0.1510	0.0111	0.0000	Pelvis	-0.0360	-0.0687	0.0225
						Femur	-0.0146	0.0714	0.0371

Table A13: Gluteus Minimus physiological parameters.

Glut. Min.	Bundle	PCSA (cm^2)	L_0 (m)	L_S (m)	α (rad)	Origin Insertion	ξ (m)	η (m)	ζ (m)
	Ant.	10.000	0.0380	0.0661	0.0000	Pelvis	0.0498	0.0302	0.1236
						Femur	0.0282	0.1520	0.0491
	Mid.	8.100	0.0340	0.0773	0.0000	Pelvis	0.0280	0.0268	0.1078
						Femur	0.0282	0.1520	0.0491
	Post.	7.400	0.0370	0.0807	0.0000	Pelvis	0.0103	0.0164	0.0912
						Femur	0.0282	0.1520	0.0491

Table A14: Gluteus Medius physiological parameters.

Glut. med.	Bundle	PCSA (cm^2)	L_0 (m)	L_S (m)	α (rad)	Origin Insertion	ξ (m)	η (m)	ζ (m)
	Ant. 1	6.317	0.0380	0.0614	0.0000	Pelvis	0.0546	0.0461	0.1351
						Femur	0.0162	0.1741	0.0530
	Ant. 2	6.317	0.0380	0.0597	0.0000	Pelvis	0.0649	0.0416	0.1361
						Femur	0.0241	0.1711	0.0521
	Ant. 3	6.317	0.0380	0.0543	0.0000	Pelvis	0.0755	0.0332	0.1331
						Femur	0.0314	0.1691	0.0510
	Ant. 4	6.317	0.0380	0.0737	0.0000	Pelvis	0.0599	0.0508	0.1427
						Femur	0.0135	0.1662	0.0574
	Ant. 5	6.317	0.0380	0.0734	0.0000	Pelvis	0.0686	0.0449	0.1414
						Femur	0.0206	0.1611	0.0577
	Ant. 6	6.317	0.0380	0.0677	0.0000	Pelvis	0.0787	0.0360	0.1377
						Femur	0.0278	0.1591	0.0566
	Post. 1	10.133	0.0450	0.0739	0.2775	Pelvis	0.0118	0.0700	0.1156
						Femur	0.0041	0.1868	0.0438
	Post. 2	10.133	0.0450	0.0746	0.2775	Pelvis	-0.0096	0.0528	0.0864
						Femur	0.0003	0.1870	0.0398
	Post. 3	10.133	0.0450	0.0675	0.2775	Pelvis	-0.0176	0.0234	0.0674
						Femur	-0.0035	0.1864	0.0377
	Post. 4	10.133	0.0450	0.0922	0.2775	Pelvis	0.0025	0.0859	0.1112
						Femur	0.0041	0.1868	0.0438
	Post. 5	10.133	0.0450	0.1070	0.2775	Pelvis	-0.0228	0.0754	0.0802
						Femur	-0.0017	0.1828	0.0483
	Post. 6	10.133	0.0450	0.1034	0.2775	Pelvis	-0.0335	0.0506	0.0599
						Femur	-0.0055	0.1819	0.0467

Table A15: Gracilis physiological parameters.

Gracilis	Bundle	PCSA (cm^2)	L_0 (m)	L_S (m)	α (rad)	Origin Insertion	ξ (m)	η (m)	ζ (m)
	1	2.450	0.1810	0.2544	0.0000	Pelvis	0.0670	-0.0975	0.0166
						Tibia	0.0167	0.0850	-0.0242
	2	2.450	0.1810	0.2715	0.0000	Pelvis	0.0872	-0.0833	0.0107
						Tibia	0.0167	0.0850	-0.0242

Table A16: Iliacus physiological parameters.

Iliacus	Bundle	PCSA (cm²)	L_0 (m)	L_S (m)	α (rad)	Origin / Insertion	ξ (m)	η (m)	ζ (m)
	Lat. 1	2.200	0.1030	0.1167	0.4625	Pelvis	0.0211	0.0836	0.1180
						Femur	-0.0091	0.1265	0.0023
	Lat. 2	2.200	0.1030	0.0953	0.4625	Pelvis	0.0393	0.0661	0.1197
						Femur	-0.0091	0.1265	0.0023
	Lat. 3	2.200	0.1030	0.0797	0.4625	Pelvis	0.0472	0.0514	0.1183
						Femur	-0.0091	0.1265	0.0023
	Mid. 1	4.333	0.0520	0.1753	0.0000	Pelvis	-0.0052	0.0867	0.0908
						Femur	-0.0091	0.1265	0.0023
	Mid. 2	4.333	0.0520	0.1477	0.0000	Pelvis	0.0074	0.0616	0.0884
						Femur	-0.0091	0.1265	0.0023
	Mid. 3	4.333	0.0520	0.1214	0.0000	Pelvis	0.0198	0.0374	0.0867
						Femur	-0.0091	0.1265	0.0023
	Med. 1	2.533	0.0890	0.1286	0.0000	Pelvis	-0.0021	0.0788	0.0515
						Femur	-0.0091	0.1265	0.0023
	Med. 2	2.533	0.0890	0.1092	0.0000	Pelvis	0.0039	0.0590	0.0554
						Femur	-0.0091	0.1265	0.0023
	Med. 3	2.533	0.0890	0.0850	0.0000	Pelvis	0.0138	0.0326	0.0544
						Femur	-0.0091	0.1265	0.0023

Table A17: Obturator Externus physiological parameters.

Obt. Ext.	Bundle	PCSA (cm²)	L_0 (m)	L_S (m)	α (rad)	Origin / Insertion	ξ (m)	η (m)	ζ (m)
	Inf. 1	2.750	0.0690	0.0521	0.0000	Pelvis	0.0501	-0.0970	0.0230
						Femur	-0.0179	0.1246	0.0335
	Inf. 2	2.750	0.0690	0.0704	0.0000	Pelvis	0.0694	-0.0882	0.0107
						Femur	-0.0179	0.1246	0.0335
	Inf. 1	8.200	0.0280	0.1140	0.0000	Pelvis	0.0893	-0.0664	0.0103
						Femur	-0.0007	0.1659	0.0238
	Inf. 2	8.200	0.0280	0.1030	0.0000	Pelvis	0.0716	-0.0813	0.0133
						Femur	-0.0007	0.1659	0.0238
	Inf. 3	8.200	0.0280	0.0900	0.0000	Pelvis	0.0501	-0.0920	0.0218
						Femur	-0.0007	0.1659	0.0238

Table A18: Obturator Internus physiological parameters.

Obturator int.	Bundle	PCSA (cm^2)	L$_0$ (m)	L$_S$ (m)	α (rad)	Origin Insertion	ξ (m)	η (m)	ζ (m)
	1	8.467	0.0210	0.1463	0.0000	Pelvis	0.0283	-0.0268	0.0486
						Femur	0.0114	0.1793	0.0343
	2	8.467	0.0210	0.1352	0.0000	Pelvis	0.0307	-0.0452	0.0413
						Femur	0.0114	0.1793	0.0343
	3	8.467	0.0210	0.1397	0.0000	Pelvis	0.0412	-0.0615	0.0315
						Femur	0.0114	0.1793	0.0343

Table A19: Pectineus physiological parameters.

Pectineus	Bundle	PCSA (cm^2)	L$_0$ (m)	L$_S$ (m)	α (rad)	Origin Insertion	ξ (m)	η (m)	ζ (m)
	1	1.700	0.1150	0.0141	0.0000	Pelvis	0.0852	-0.0349	0.0392
						Femur	-0.0024	0.1002	0.0116
	2	1.700	0.1150	0.0218	0.0000	Pelvis	0.0902	-0.0384	0.0357
						Femur	-0.0021	0.0914	0.0113
	3	1.700	0.1150	0.0294	0.0000	Pelvis	0.0952	-0.0420	0.0322
						Femur	-0.0018	0.0826	0.0110
	4	1.700	0.1150	0.0211	0.0000	Pelvis	0.1002	-0.0455	0.0287
						Femur	-0.0024	0.1002	0.0116

Table A20: Peroneus Brevis physiological parameters.

Peroneus brev.	Bundle	PCSA (cm^2)	L$_0$ (m)	L$_S$ (m)	α (rad)	Origin Insertion	ξ (m)	η (m)	ζ (m)
	1	6.333	0.0270	0.2811	0.4032	Tibia	0.0139	-0.0365	0.0398
						Foot	0.0047	-0.0154	0.0532
	2	6.333	0.0270	0.2342	0.4032	Tibia	0.0126	-0.0833	0.0359
						Foot	0.0047	-0.0154	0.0532
	3	6.333	0.0270	0.1888	0.4032	Tibia	0.0119	-0.1286	0.0317
						Foot	0.0047	-0.0154	0.0532

Table A21: Peroneus Longus physiological parameters.

Peroneus brev.	Bundle	PCSA (cm^2)	L$_0$ (m)	L$_S$ (m)	α (rad)	Origin Insertion	ξ (m)	η (m)	ζ (m)
	1	7.967	0.0340	0.3664	0.2758	Tibia	0.0234	0.0788	0.0470
						Foot	-0.0133	-0.0053	0.0426
	2	7.967	0.0340	0.3289	0.2758	Tibia	0.0189	0.0415	0.0447
						Foot	-0.0133	-0.0053	0.0426
	3	7.967	0.0340	0.2917	0.2758	Tibia	0.0147	0.0046	0.0422
						Foot	-0.0133	-0.0053	0.0426

Table A22: Peroneus Tertius

Peroneus tret.	Bundle	PCSA (cm^2)	L$_0$ (m)	L$_S$ (m)	α (rad)	Origin Insertion	ξ (m)	η (m)	ζ (m)
	1	2.067	0.0430	0.1967	0.3334	Tibia	0.0179	-0.1182	0.0278
						Foot	0.0512	-0.0196	0.0484
	2	2.067	0.0430	0.2473	0.3334	Tibia	0.0178	-0.0667	0.0320
						Foot	0.0512	-0.0196	0.0484
	3	2.067	0.0430	0.2984	0.3334	Tibia	0.0184	-0.0150	0.0351
						Foot	0.0512	-0.0196	0.0484

Table A23: Piriformis physiological parameters.
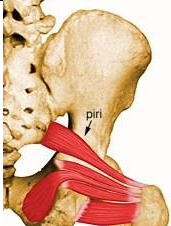
	Bundle	PCSA (cm^2)	L$_0$ (m)	L$_S$ (m)	α (rad)	Origin Insertion	ξ (m)	η (m)	ζ (m)
	1	8.100	0.0390	0.1022	0.0000	Pelvis	-0.0502	-0.0256	0.0163
						Femur	-0.0006	0.1868	0.0264

Table A24: Plantaris physiological parameters.

Plantaris	Bundle	PCSA (cm^2)	L$_0$ (m)	L$_S$ (m)	α (rad)	Origin Insertion	ξ (m)	η (m)	ζ (m)
	1	2.400	0.0480	0.4393	0.0000	Femur	0.0076	-0.2129	0.0209
						Foot	-0.0875	-0.0302	0.0063

Table A25: Popliteus physiological parameters.

Popliteus	Bundle	PCSA (cm^2)	L$_0$ (m)	L$_S$ (m)	α (rad)	Origin Insertion	ξ (m)	η (m)	ζ (m)
	1	5.350	0.0240	0.0952	0.0000	Femur	0.0070	-0.2374	0.0290
						Tibia	0.0090	0.0558	-0.0094
	2	5.350	0.0240	0.0597	0.0000	Femur	0.0070	-0.2374	0.0290
						Tibia	0.0019	0.0976	-0.0012

Table A26: Psoas physiological parameters.

Psoas	Bundle	PCSA (cm^2)	L_0 (m)	L_S (m)	α (rad)	Origin Insertion	ξ (m)	η (m)	ζ (m)
	Minor 1	1.100	0.0590	0.2145	0.0000	Pelvis	0.0000	0.2041	0.0344
						Femur	0.0247	0.1546	-0.0271
	Major 1	6.500	0.0990	0.2064	0.2339	Pelvis	-0.0068	0.1777	0.0349
						Femur	-0.0091	0.1265	0.0023
	Major 2	6.500	0.0990	0.1596	0.2339	Pelvis	0.0215	0.1357	0.0309
						Femur	-0.0091	0.1265	0.0023
	Major 3	6.500	0.0990	0.1218	0.2339	Pelvis	0.0225	0.0933	0.0317
						Femur	-0.0091	0.1265	0.0023

Table A27: Quadratis Femoris physiological parameters.
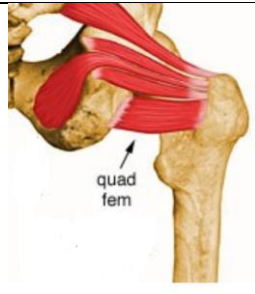
Quadratis	Bundle	PCSA (cm^2)	L_0 (m)	L_S (m)	α (rad)	Origin Insertion	ξ (m)	η (m)	ζ (m)
	1	3.650	0.0340	0.0834	0.0000	Pelvis	0.0415	-0.0985	0.0275
						Femur	-0.0149	0.1556	0.0335
	2	3.650	0.0340	0.0742	0.0000	Pelvis	0.0351	-0.1011	0.0355
						Femur	-0.0153	0.1477	0.0341
	3	3.650	0.0340	0.0652	0.0000	Pelvis	0.0288	-0.1037	0.0436
						Femur	-0.0155	0.1397	0.0346
	4	3.650	0.0340	0.0566	0.0000	Pelvis	0.0225	-0.1063	0.0516
						Femur	-0.0158	0.1318	0.0351

Table A28: Rectus Femoris physiological parameters.

Rectus fem.-	Bundle	PCSA (cm^2)	L_0 (m)	L_S (m)	α (rad)	Origin Insertion	ξ (m)	η (m)	ζ (m)
	1	14.450	0.0780	0.3403	0.3840	Pelvis	0.0808	-0.0060	0.1108
						Patella	-0.0010	0.0229	0.0006
	2	14.450	0.0780	0.3390	0.3840	Pelvis	0.0808	-0.0060	0.1108
						Patella	-0.0017	0.0237	0.0122

Table A29: Sartoris physiological parameters.
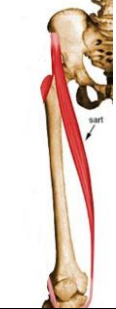
Sartorius	Bundle	PCSA (cm^2)	L$_0$ (m)	L$_S$ (m)	α (rad)	Origin / Insertion	ξ (m)	η (m)	ζ (m)
	Prox.1	5.900	0.3470	0.1851	0.0000	Pelvis	0.0826	0.0262	0.1255
						Tibia	0.0190	0.0892	-0.0260
	Dist.1	5.900	0.3470	0.1827	0.0000	Pelvis	0.0826	0.0262	0.1255
						Tibia	0.0190	0.0892	-0.0260

Table A30: Semimembranosus physiological parameters.

Semimemb	Bundle	PCSA (cm^2)	L$_0$ (m)	L$_S$ (m)	α (rad)	Origin / Insertion	ξ (m)	η (m)	ζ (m)
	1	17.100	0.0810	0.3034	0.4363	Pelvis	0.0225	-0.1148	0.0702
						Tibia	-0.0254	0.1316	-0.0082

Table A31: Semitendinosus physiological parameters.

Semitend	Bundle	PCSA (cm^2)	L$_0$ (m)	L$_S$ (m)	α (rad)	Origin / Insertion	ξ (m)	η (m)	ζ (m)
	1	14.700	0.1420	0.3011	0.0000	Pelvis	0.0102	-0.1094	0.0627
						Tibia	0.0093	0.0743	-0.0218

Table A32: Soleus physiological parameters.

Soleus	Bundle	PCSA (cm^2)	L$_0$ (m)	L$_S$ (m)	α (rad)	Origin Insertion	ξ (m)	η (m)	ζ (m)
	Med.1	31.433	0.0240	0.2731	0.4939	Tibia	0.0149	-0.0143	-0.0176
						Foot	-0.0890	-0.0352	0.0089
	Med.2	31.433	0.0240	0.3039	0.4939	Tibia	0.0129	0.0174	-0.0161
						Foot	-0.0890	-0.0352	0.0089
	Med.3	31.433	0.0240	0.3277	0.4939	Tibia	0.0086	0.0423	-0.0119
						Foot	-0.0890	-0.0352	0.0089
	Lat.1	28.633	0.0260	0.3073	0.4939	Tibia	0.0092	0.0253	0.0416
						Foot	-0.0935	-0.0304	0.0229
	Lat. 2	28.633	0.0260	0.3343	0.4939	Tibia	0.0108	0.0521	0.0437
						Foot	-0.0935	-0.0304	0.0229
	Lat. 3	28.633	0.0260	0.3737	0.4939	Tibia	0.0121	0.0914	0.0484
						Foot	-0.0935	-0.0304	0.0229

Table A33: Tensor Fascia Lata physiological parameters.

Tensor fasc.l.	Bundle	PCSA (cm^2)	L$_0$ (m)	L$_S$ (m)	α (rad)	Origin Insertion	ξ (m)	η (m)	ζ (m)
	1	4.400	0.1150	0.3296	0.0000	Pelvis	0.0789	0.0312	0.1381
						Tibia	0.0553	0.1810	0.0224
	2	4.400	0.1150	0.3396	0.0000	Pelvis	0.0743	0.0414	0.1418
						Tibia	0.0553	0.1810	0.0224

Table A34: Tibialis Anterior physiological parameters.

Tibialis ant	Bundle	PCSA (cm^2)	L$_0$ (m)	L$_S$ (m)	α (rad)	Origin Insertion	ξ (m)	η (m)	ζ (m)
	1	8.867	0.0460	0.3506	0.1676	Tibia	0.0448	0.0996	0.0103
						Foot	0.0314	-0.0143	-0.0179
	2	8.867	0.0460	0.3228	0.1676	Tibia	0.0423	0.0724	0.0044
						Foot	0.0314	-0.0143	-0.0179
	3	8.867	0.0460	0.2710	0.1676	Tibia	0.0305	0.0201	0.0019
						Foot	0.0314	-0.0143	-0.0179

Table A35: Tibialis Posterior physiological parameters.

Tibialis post.	Bundle	PCSA (cm^2)	L$_0$ (m)	L$_S$ (m)	α (rad)	Origin Insertion	ξ (m)	η (m)	ζ (m)
	Med.1	7.200	0.0240	0.3331	0.2391	Tibia	0.0211	0.0669	0.0090
						Foot	-0.0149	-0.0017	-0.0156
	Med.2	7.200	0.0240	0.2847	0.2391	Tibia	0.0184	0.0186	0.0056
						Foot	-0.0149	-0.0017	-0.0156
	Med.3	7.200	0.0240	0.2219	0.2391	Tibia	0.0176	-0.0442	0.0027
						Foot	-0.0149	-0.0017	-0.0156
	Lat.1	7.200	0.0240	0.2956	0.2391	Tibia	0.0192	0.0253	0.0347
						Foot	-0.0149	-0.0017	-0.0156
	Lat.2	7.200	0.0240	0.2229	0.2391	Tibia	0.0160	-0.0482	0.0288
						Foot	-0.0149	-0.0017	-0.0156
	Lat.3	7.200	0.0240	0.1552	0.2391	Tibia	0.0169	-0.1197	0.0240
						Foot	-0.0149	-0.0017	-0.0156

Table A36: Vastus Intermedius physiological parameters.
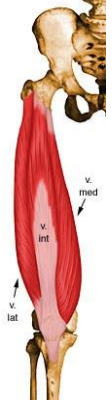
Vastus interm.	Bundle	PCSA (cm^2)	L$_0$ (m)	L$_S$ (m)	α (rad)	Origin Insertion	ξ (m)	η (m)	ζ (m)
	1	6.350	0.0770	0.0813	0.2059	Femur	0.0458	-0.0602	-0.0069
						Patella	-0.0010	0.0229	0.0006
	2	6.350	0.0770	0.1378	0.2059	Femur	0.0397	-0.0043	0.0024
						Patella	-0.0010	0.0229	0.0006
	3	6.350	0.0770	0.1991	0.2059	Femur	0.0324	0.0554	0.0168
						Patella	-0.0010	0.0229	0.0006
	4	6.350	0.0770	0.0783	0.2059	Femur	0.0439	-0.0626	0.0050
						Patella	-0.0017	0.0237	0.0122
	5	6.350	0.0770	0.1346	0.2059	Femur	0.0375	-0.0073	0.0165
						Patella	-0.0017	0.0237	0.0122
	6	6.350	0.0770	0.1960	0.2059	Femur	0.0307	0.0530	0.0277
						Patella	-0.0017	0.0237	0.0122

Table A37: Vastus Lateralis physiological parameters.
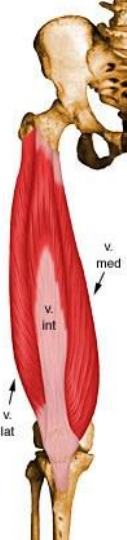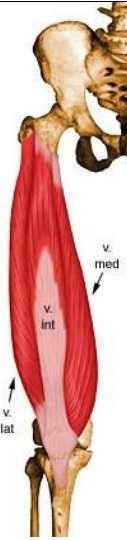
Vastus lat.	Bundle	PCSA (cm²)	L_0 (m)	L_S (m)	α (rad)	Origin Insertion	ξ (m)	η (m)	ζ (m)
	Lat. 1	1.783	0.0910	0.0249	0.0000	Femur	0.0116	-0.1199	0.0043
						Patella	-0.0017	0.0237	0.0122
	Lat. 2	1.783	0.0910	0.0629	0.0000	Femur	0.0124	-0.0741	0.0055
						Patella	-0.0017	0.0237	0.0122
	Lat. 3	1.783	0.0910	0.1051	0.0000	Femur	0.0112	-0.0287	0.0098
						Patella	-0.0017	0.0237	0.0122
	Lat. 4	1.783	0.0910	0.1491	0.0000	Femur	0.0083	0.0161	0.0174
						Patella	-0.0017	0.0237	0.0122
	Lat. 5	1.783	0.0910	0.1939	0.0000	Femur	0.0036	0.0605	0.0282
						Patella	-0.0017	0.0237	0.0122
	Lat. 6	1.783	0.0910	0.2395	0.0000	Femur	-0.0029	0.1043	0.0423
						Patella	-0.0017	0.0237	0.0122
	Sup. 1	29.500	0.0910	0.2752	0.0000	Femur	0.0163	0.1432	0.0542
						Patella	-0.0017	0.0237	0.0122
	Sup. 2	29.500	0.0910	0.2856	0.0000	Femur	0.0298	0.1580	0.0373
						Patella	-0.0017	0.0237	0.0122

Table A38: Vastus Medialis physiological parameters.

Vastus med.	Bundle	PCSA (cm²)	L_0 (m)	L_S (m)	α (rad)	Origin Insertion	ξ (m)	η (m)	ζ (m)
	Inf.1	4.900	0.0760	0.0316	0.0000	Femur	0.0181	-0.1231	-0.0150
						Patella	-0.0010	0.0229	0.0006
	Inf. 2	4.900	0.0760	0.0265	0.0000	Femur	0.0280	-0.1225	-0.0197
						Patella	-0.0010	0.0229	0.0006
	Mid. 1	11.600	0.0760	0.0686	0.0000	Femur	0.0218	-0.0778	-0.0102
						Patella	-0.0010	0.0229	0.0006
	Mid. 2	11.600	0.0760	0.0656	0.0000	Femur	0.0315	-0.0772	-0.0146
						Patella	-0.0010	0.0229	0.0006
	Sup. 1	26.900	0.0830	0.1136	0.0000	Femur	0.0214	-0.0255	-0.0023
						Patella	-0.0010	0.0229	0.0006
	Sup. 2	26.900	0.0830	0.1116	0.0000	Femur	0.0303	-0.0250	-0.0064
						Patella	-0.0010	0.0229	0.0006
	Sup. 3	26.900	0.0830	0.1660	0.0000	Femur	0.0184	0.0273	0.0068
						Patella	-0.0010	0.0229	0.0006
	Sup. 4	26.900	0.0830	0.1642	0.0000	Femur	0.0273	0.0278	0.0027
						Patella	-0.0010	0.0229	0.0006
	Sup. 5	26.900	0.0830	0.2319	0.0000	Femur	0.0188	0.0941	0.0164
						Patella	-0.0010	0.0229	0.0006
	Sup. 6	26.900	0.0830	0.2311	0.0000	Femur	0.0234	0.0944	0.0142
						Patella	-0.0010	0.0229	0.0006

Appendix B: **Pattern Search Results**

The solutions found for each iteration of the pattern search is presented in Table B1. All the solutions minimize the RMSE between numerical and *in vivo* HCF. The combinations of weight factors found for each iteration is presented, as well the associated RMSE.

Table B1: Local minimums found for each iteration of the pattern search.

Subject		It.	W_1	W_2	RMSE [%BW]
H2R	Standard		0,33	0,66	63,25
	Optimal Weight Factors	1	87,40	11,09	60,80
		2	87,46	11,10	60,80
		3	87,41	11,10	60,80
		4	87,42	11,10	60,80
		5	87,42	11,10	60,80
		6	87,47	11,10	60,80
		7	87,51	11,10	60,80
		8	87,43	11,09	60,80
		9	87,44	11,10	60,80
		10	87,13	11,06	60,80
H1L	Standard		0,33	0,66	68,82
	Optimal Weight Factors	1	47.74	0.04	63,27
		2	2.10	0.10	63,32
		3	1.98	0.09	63,32
		4	42.54	0.04	63,27
		5	1.29	0,07	63.33
		6	0.76	0.01	63,27
		7	0.77	0,01	63,27
		8	47.74	0,04	63,27
		9	2,10	0,10	63,32
		10	1,98	0,09	63,32